THESIS

Power recycling for an interferometric gravitational wave detector

Masaki Ando

Department of Physics, Faculty of Science,
University of Tokyo.

December 1998

Contents

1 Introduction **4**

2 Gravitational Waves **9**

2.1 Wave solutions of the Einstein equation 10

2.1.1 Einstein equation 10

2.1.2 Linearized theory 10

2.1.3 Gravitational wave 12

2.1.4 Effect of gravitational waves on free particles 13

2.1.5 Polarization 14

2.2 Generation of gravitational waves 15

2.2.1 Radiation of gravitational waves 15

2.2.2 Sources of gravitational waves 16

2.2.3 Evidence of the existence of a gravitational wave 20

2.3 Detection of gravitational waves 20

2.3.1 Physical and astronomical aims 20

2.3.2 Resonant-mass detectors 21

2.3.3 Interferometric detector 24

2.3.4 Other types of gravitational wave detectors 27

3 Interferometric gravitational wave detector **30**

3.1 Michelson interferometer 31

3.1.1 Phase detection with a Michelson interferometer 32

3.1.2 Detection of gravitational waves 33

3.1.3 Frequency response and baseline length 35

3.1.4 Optimization of the frequency response 36

3.2 Fabry-Perot cavity . . . 39
3.2.1 Characteristics of a Fabry-Perot cavity . . . 39
3.2.2 Coupling of a cavity . . . 41
3.2.3 FSR and finesse . . . 42
3.2.4 Phase enhancement of a Fabry-Perot cavity . . . 43
3.2.5 Response to gravitational waves . . . 45
3.2.6 Storage time . . . 46
3.2.7 Response to mirror displacement . . . 47
3.2.8 Response to frequency fluctuation . . . 48
3.3 Power recycling . . . 50
3.3.1 Principle of power recycling . . . 50
3.3.2 Recycling cavity . . . 51
3.3.3 Power recycling gain . . . 52
3.4 Noise sources for an interferometer . . . 53
3.4.1 Optical readout noise . . . 53
3.4.2 Thermal noise . . . 56
3.4.3 Seismic noise . . . 58
3.4.4 Noises of the laser source . . . 60
3.4.5 Residual gas noise . . . 62
3.4.6 Noises due to control of the interferometer . . . 63

4 Signal separation scheme **65**
4.1 Overview of control schemes . . . 66
4.1.1 Power-recycled Fabry-Perot-Michelson interferometer . . . 66
4.1.2 Frontal modulation . . . 67
4.1.3 Signal separation . . . 70
4.2 Frontal modulation . . . 71
4.2.1 Modulation and demodulation . . . 71
4.2.2 Static response of an interferometer . . . 79
4.2.3 Derivative of the response . . . 81
4.3 Sensitivities of the signals under operational conditions . . . 84
4.3.1 Operational point . . . 85
4.3.2 Conditions for the sidebands . . . 86

4.3.3 Response of the interferometer at the operational point . . 88
4.3.4 Signals extracted using frontal modulation 89
4.4 Signal-separation method 91
4.4.1 Signal mixing problem 92
4.4.2 Sideband elimination 92
4.4.3 Adjustment of the optical parameters 93
4.4.4 Calculation of the signals in a model interferometer 95
4.4.5 Requirements for signal separation 96

5 3-m Fabry-Perot-Michelson interferometer 100
5.1 Optical design 104
5.1.1 Mirrors 104
5.1.2 Beam splitter 106
5.1.3 Pick-off mirror 107
5.1.4 Fabry-Perot arm cavity 108
5.1.5 Michelson interferometer and power recycling 108
5.2 Suspension system 109
5.2.1 Double pendulum 109
5.2.2 Isolation ratio 111
5.2.3 Coil-magnet actuator 111
5.3 Laser 113
5.3.1 Laser source 115
5.3.2 Mode matching 117
5.3.3 Optical isolators 118
5.4 Signal extraction and control system 119
5.4.1 Modulation, demodulation, and control 120
5.4.2 Oscillator 121
5.4.3 Phase modulator 121
5.4.4 RF photo detector 122
5.4.5 Demodulator 123
5.5 Devices for monitor and measurement 125
5.5.1 AF photo detector 125
5.5.2 Intensity modulator 125

5.5.3 Optical spectrum analyzer . . . 126
5.6 Vacuum system . . . 126

6 Experiment **128**
6.1 Lock acquisition . . . 129
6.1.1 Correlation diagram . . . 129
6.1.2 Guide locking scheme . . . 131
6.1.3 Automatic locking scheme . . . 135
6.2 Operation with power recycling . . . 137
6.2.1 Power-recycling gain . . . 138
6.2.2 Stability of operation . . . 139
6.2.3 Control system . . . 142
6.2.4 Calibration of signals . . . 143
6.2.5 Residual RMS deviations . . . 144
6.2.6 Signal gain . . . 145
6.3 Signal separation . . . 147
6.3.1 Mixing in the V_{RI} signal . . . 148
6.3.2 Signal sensitivity matrix . . . 150
6.4 Sensitivity of the interferometer . . . 151
6.4.1 Displacement noise level . . . 151
6.4.2 Estimation of noise level . . . 152
6.4.3 Summary of noise sources . . . 159

7 Discussion and conclusion **163**
7.1 Results and discussions . . . 163
7.2 Power recycling in a real detector . . . 165
7.3 Conclusion . . . 166

References **167**

Acknowledgements **174**

Chapter 1

Introduction

Gravitational waves are ripples of space-time curvature which propagate across the universe at the speed of light. The existence of gravitational waves has been predicted as one of the consequences of the General Theory of Relativity [1, 2, 3], and confirmed as a result of the observation of the binary pulsar PSR 1913+16 [4, 5, 6]. However, gravitational waves have not been directly detected, because of the weakness of the gravitational interactions. The detection of gravitational waves will not only confirm the General Theory of Relativity, but also open a new field of 'gravitational wave astronomy'. In order to create this new astronomy which is qualitatively different from that with electro-magnetic waves, several groups in the world are struggling with development and construction of gravitational wave detectors.

Mainly, two types of gravitational wave detector have been developed: resonant-mass type detectors and free-mass type detectors. At first, gravitational waves were attempted to detect with resonant-mass detectors [7, 8], which are designed to detect the vibration of an elastic body excited by gravitational waves. Since many kinds of technology have been developed and accumulated, resonant-mass detectors have already reached the observation phase. However, a resonant-mass detector is not suitable for an observation of the waveform of gravitational waves because it is sensitive only at a narrow frequency range near the resonance of the elastic body. On the other hand, it is possible to observe the waveform of gravitational waves with a free-mass detector using a laser interferometer, which has a wider observation band [9, 10]. Laser interferometric gravitational wave

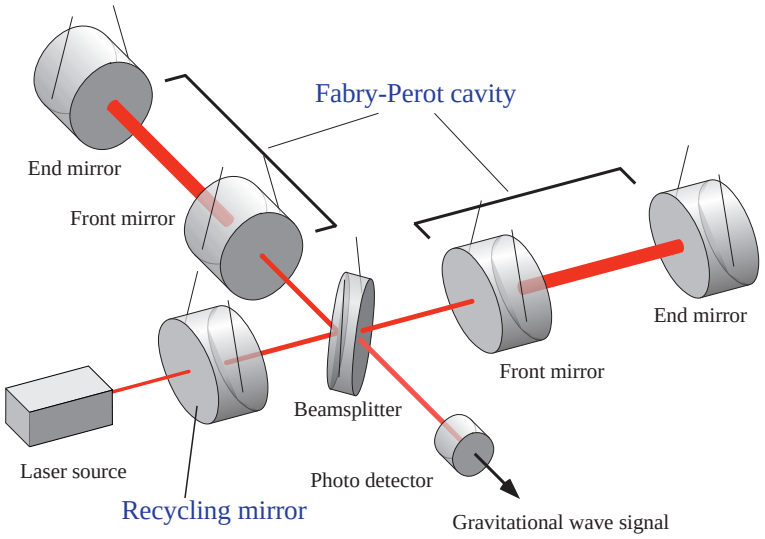

Figure 1.1: Laser interferometric gravitational wave detector. It is based on a Michelson interferometer, which detects the differential length change in two orthogonal optical paths. In practice, a few mirrors are added to the Michelson interferometer to increase the effective arm length and laser power. This figure shows a Fabry-Perot-Michelson interferometer with power recycling, which is mainly discussed in this thesis.

detectors have been energetically developed recently because of their advantages of a wide observation band and its high potential sensitivity with a larger baseline length compared with a resonant-mass detectors. At present, four projects are constructing laser interferometric gravitational wave detectors: the LIGO project in the United States of America [11], the VIRGO project by Italy and France [12], the GEO project by Germany and Britain [13], and the TAMA project in Japan [14].

Gravitational waves are detected with a laser interferometer by measuring the proper length between mirrors by means of laser light. An interferometric gravitational wave detector is basically a Michelson interferometer which detects the differential change in two orthogonal optical path lengths separated by a beamsplitter (Fig. 1.1). In practice, the interferometer has a little more complex optical configuration with a few additional mirrors to the Michelson interferometer in order to increase the effective arm length and laser power. In the LIGO,

VIRGO, and TAMA detectors, the Michelson interferometer is extended to a Fabry-Perot-Michelson interferometer with power recycling. On the other hand, a dual-recycling (signal recycling and power recycling) technique is applied to the Michelson interferometer in the GEO detector. All of the four projects adopt a power recycling technique.

Power recycling [15] is a technique to improve the shot-noise limited sensitivity of an interferometer by enhancing the effective laser power. In order to operate a Michelson interferometer at its highest sensitivity, the interference fringe must be dark at the output port of the interferometer. Under this operational condition, the laser beams reflected by the arm mirrors of the Michelson interferometer interfere constructively in the direction of the laser source at the beamsplitter; almost all of the laser power goes back toward the laser source. The recycling mirror reflects this beam back toward the beam splitter and thus enhances the laser power in the interferometer, which results in an improvement of the shot-noise level. Thus, power recycling is indispensable for advanced interferometric gravitational wave detectors because shot noise is one of the fundamental noise sources of an interferometer.

Though power recycling will be used in all of the interferometric detectors under construction, several problems must be solved in order to apply power recycling to these detectors. One of them is a problem in control of the interferometer. In order to behave as free masses, the mirrors of an interferometric gravitational wave detector are suspended as pendulums. Though the suspension system has another role to isolate the mirror from the seismic motion at the observation frequency band, the mirror is largely excited by the seismic motion at the resonant frequency of the pendulum. Thus it is necessary to control the interferometer in order to keep it at the operational point. However, since a power-recycled interferometer has a complex and coupled optical configuration, careful analysis and design are required to extract independent control signals from the interferometer. In addition, in a power-recycled interferometer, the lock acquisition is not a simple problem. Since the control signals are linear functions of the motion of the interferometer only around the operational point, it is not obvious whether the interferometer can be locked at the operational point from an uncontrolled state. Thus, the controllability and lock-acquisition of a

power-recycled interferometer must be tested experimentally.

However, before the research described in this thesis, power recycling has not been realized nor investigated with an interferometer which has the similar configuration as a real detector: a complex optical configuration with suspended mirrors. Power recycling has been realized experimentally in several table-top interferometers with rigidly supported mirrors: a simple Michelson interferometer with power recycling [16], a dual-recycled Michelson interferometer [17], and power-recycled Fabry-Perot-Michelson interferometers [18, 19, 20, 21, 22, 23]. On the other hand, in interferometers with optical components suspended as pendulums, power recycling has been realized experimentally only with simple Michelson interferometers [24, 25, 26]. Thus, it is necessary to realize power recycling with the same optical configuration as a real interferometric gravitational wave detector: a power-recycled Fabry-Perot-Michelson interferometer or a dual-recycled Michelson interferometer [27, 28, 29][1].

A prototype interferometer with an arm length of 3 m has been developed at the University of Tokyo [30, 31]. It has the same characteristics as those of a real gravitational wave detector; it is a Fabry-Perot-Michelson interferometer with suspended optical components like LIGO, VIRGO, and TAMA. With this prototype interferometer, we have developed the control system for a power-recycled interferometer. This research contains three topics. The first topic is to realize power recycling with this prototype interferometer [32]. Since power recycling was not demonstrated before this research in a suspended Fabry-Perot-Michelson interferometer, it was quite significant to investigate the lock acquisition process experimentally. The second topic of this research is to develop a signal-separation scheme for the control of a power-recycled Fabry-Perot-Michelson interferometer [33]. In order to operate a power-recycled Fabry-Perot-Michelson interferometer, four longitudinal degrees of freedom must be controlled to maintain the operational condition. One of the main problems in controlling a power-recycled interferometer is that the control signal for the length of the recycling cavity can-

[1]After power recycling was demonstrated with this research, power recycling was realized with a 40-m prototype interferometer at California Institute of Technology by the LIGO group [27] and a 20-m prototype interferometer at National Astronomical Observatory by the TAMA group [28]. Dual recycling was also realized with a 30-m prototype interferometer at Garching by the GEO group [29].

not be extracted independently with a conventional signal-extraction scheme. To solve this problem, we have invented a new scheme to separate the signals and tested it experimentally. The third topic of this research is to estimate the effect of various noise sources in this prototype interferometer. The role of the control system is to maintain the stability and, at the same time, the sensitivity of the interferometer. Thus, the control system of the 3-m prototype interferometer is designed so as not to degrade the sensitivity of the interferometer.

In this thesis, we describe the results of the power recycling experiments on a 3-m Fabry-Perot-Michelson interferometer with suspended mirrors. In particular, this thesis is concentrated on the control of the interferometer, which is one of the main problems in power recycling. In Chapter 2, the physical background of gravitational waves is described: the propagation, generation, and detection of gravitational waves. Chapter 3 describes the fundamentals of an interferometric gravitational wave detector: its principle, a Fabry-Perot cavity, the power recycling technique, and the main noise sources of the detector. In Chapter 4, we explain the signal-extraction and control scheme for a power-recycled Fabry-Perot-Michelson interferometer: the conventional scheme, its signal-mixing problem, and our new signal-separation scheme. The experimental setup of a 3-m prototype interferometer is given in Chapter 5. Chapter 6 details the experimental results with power recycling: the lock-acquisition analysis, realization of power recycling, signal-separation measurements, and noise estimations. In Chapter 7, we summarize and discuss the achievements and problems with a 3-m prototype interferometer, and give a prospect for power recycling on real gravitational wave detectors.

Chapter 2

Gravitational Waves

Gravitational waves are ripples of space-time curvature which propagate across the universe at the speed of light. The existence of gravitational waves was predicted by A. Einstein as one of the consequences of the General Theory of Relativity [1, 2, 3]. Gravitational waves are generated by accelerated masses, in analogy to electro-magnetic waves generated by accelerated charges. The existence of the gravitational waves has been confirmed indirectly as a result of the observation of the binary pulsar PSR 1913+16 discovered by R. A. Hulse and J. H. Taylor [4, 5, 6]. However, gravitational waves have not been directly detected, because of the weakness of the gravitational interactions. The detection of gravitational waves will not only confirm the General Theory of Relativity, but also create a new field of a 'gravitational wave astronomy'.

In this chapter, we review wave solutions of the Einstein equation, generation of gravitational waves, and its detection.

- **Wave solutions of the Einstein equation.** The theory of gravitational waves. Their effect on free particles, and their polarization.
- **Generation of gravitational waves.** The theory of gravitational radiation. The sources of gravitational waves.
- **Detection of gravitational waves.** The physical and astronomical aims of gravitational wave detection. Several types of gravitational wave detectors.

2.1 Wave solutions of the Einstein equation

2.1.1 Einstein equation

In the General Theory of Relativity, the four dimensional distance, ds, between two points in space time, x^μ and $x^\mu + dx^\mu$, is given by

$$ds^2 = g_{\mu\nu} dx^\mu dx^\nu, \tag{2.1}$$

where $g_{\mu\nu}$ is the metric tensor[1]. The metric tensor $g_{\mu\nu}$ is determined by the energy-momentum tensor $T_{\mu\nu}$ according to the Einstein equation

$$G_{\mu\nu} = \frac{8\pi G}{c^4} T_{\mu\nu} \tag{2.2}$$

$$G_{\mu\nu} \equiv R_{\mu\nu} - \frac{1}{2} g_{\mu\nu} R, \tag{2.3}$$

where c and G are the speed of light[2] and the gravitational constant[3], respectively. The Christoffel symbol ($\Gamma^\mu{}_{\nu\lambda}$), the Riemann tensor ($R^\mu{}_{\nu\alpha\beta}$), the Ricci tensor ($R_{\mu\nu}$), and the Ricci scalar (R) satisfy the following equations:

$$\Gamma^\mu{}_{\nu\lambda} = \frac{1}{2} g^{\mu\alpha} (g_{\alpha\nu,\lambda} + g_{\alpha\lambda,\nu} - g_{\nu\lambda,\alpha}) \tag{2.4}$$

$$R^\mu{}_{\nu\alpha\beta} = \Gamma^\mu{}_{\nu\beta,\alpha} - \Gamma^\mu{}_{\nu\alpha,\beta} + \Gamma^\mu{}_{\gamma\alpha}\Gamma^\gamma{}_{\nu\beta} - \Gamma^\mu{}_{\gamma\beta}\Gamma^\gamma{}_{\nu\alpha} \tag{2.5}$$

$$R_{\mu\nu} \equiv R^\alpha{}_{\mu\alpha\nu} \tag{2.6}$$

$$R \equiv R^\alpha{}_\alpha. \tag{2.7}$$

2.1.2 Linearized theory

Though it is difficult to solve the equation analytically, the nature of the gravitational field is investigated by linearizing the equation. In nearly flat space time, the metric can be treated as a perturbation from the Minkowski metric:

$$g_{\mu\nu} = \eta_{\mu\nu} + h_{\mu\nu}, \tag{2.8}$$

[1]Greek indices (α, β, μ, ν, and so on) denote the coordinate numbers from 0 to 3, while Roman indices (i, j, k, and so on) denote the coordinate numbers from 1 to 3. The coordinates are denoted by $x^0 = ct$, $x^1 = x$, $x^2 = y$, and $x^3 = z$. In addition, the indices follow the Einstein summation convention, i.e. any indices repeated in a product are automatically summed up.

[2]The speed of light: $c = 2.99792458 \times 10^8$ [m/s].

[3]The gravitational constant: $G = 6.67259 \times 10^{-11}$ [N $\cdot$ m^2/kg^2].

where the Minkowski metric $\eta_{\mu\nu}$ is give by

$$\eta_{\mu\nu} = \begin{pmatrix} -1 & 0 & 0 & 0 \\ 0 & 1 & 0 & 0 \\ 0 & 0 & 1 & 0 \\ 0 & 0 & 0 & 1 \end{pmatrix}. \tag{2.9}$$

Defining the trace reverse tensor $\bar{h}_{\mu\nu}$ of $h_{\mu\nu}$ by

$$\bar{h}_{\mu\nu} \equiv h_{\mu\nu} - \frac{1}{2}\eta_{\mu\nu}h \tag{2.10}$$

$$h \equiv h^{\alpha}{}_{\alpha}, \tag{2.11}$$

and considering only to the first order of $\bar{h}_{\mu\nu}$, we obtain the equations[4]

$$\Gamma^{\mu}{}_{\nu\lambda} = \frac{1}{2}(\bar{h}^{\mu}{}_{\nu,\lambda} + \bar{h}^{\mu}{}_{\lambda,\nu} - \bar{h}_{\nu\lambda}{}^{,\mu}) \tag{2.12}$$

$$G_{\mu\nu} = -\frac{1}{2}(\bar{h}_{\mu\nu,\alpha}{}^{,\alpha} + \eta_{\mu\nu}\bar{h}_{\alpha\beta}{}^{,\alpha\beta} - \bar{h}_{\mu\alpha,\nu}{}^{,\alpha} - \bar{h}_{\nu\alpha,\mu}{}^{,\alpha}). \tag{2.13}$$

Putting a Lorentz gauge condition

$$\bar{h}^{\mu\nu}{}_{,\nu} = 0 \tag{2.14}$$

to Eq. (2.13), we obtain the linearized Einstein equation[5]

$$\Box\bar{h}_{\mu\nu} = -\frac{16\pi G}{c^4}T_{\mu\nu}. \tag{2.15}$$

[4]Since $|\bar{h}_{\mu\nu}| \ll 1$, we can use the relations

$$\bar{h}^{\mu}{}_{\nu} = \eta^{\mu\alpha}\bar{h}_{\alpha\nu}$$
$$\bar{h}^{\mu\nu} = \eta^{\nu\alpha}\bar{h}^{\mu}{}_{\alpha}.$$

.

[5]From Eq. (2.13), we obtain an equation:

$$G_{\mu\nu} = -\frac{1}{2}\Box\bar{h}_{\mu\nu}$$

$$(\Box \equiv -\frac{\partial^2}{c^2\partial t^2} + \triangle).$$

2.1.3 Gravitational wave

The linearized Einstein equation, Eq. (2.15), in vacuum ($T_{\mu\nu} = 0$) is

$$\Box \bar{h}_{\mu\nu} = 0. \tag{2.16}$$

Eq. (2.16) has a plane wave solution

$$\bar{h}_{\mu\nu} = A_{\mu\nu} \exp(\mathrm{i} k_\alpha x^\alpha). \tag{2.17}$$

Under the Lorentz gauge condition, Eq. (2.14), the following equations are satisfied:

$$A_{\mu\nu} k^\nu = 0 \tag{2.18}$$

$$k_\mu k^\mu = 0. \tag{2.19}$$

Equation (2.18) and (2.19) show that the plane-wave solution Eq. (2.17) is transverse wave which propagates at the speed of light. This plane wave is called a gravitational wave.

By the gauge transformations called Transverse Traceless gauge (TT gauge)[6], the gravitational waves propergating on the z-direction is written as[7]

$$\bar{h}_{\mu\nu} = A_{\mu\nu} e^{\mathrm{i}k(ct-z)} \tag{2.20}$$

$$A_{\mu\nu} = \begin{pmatrix} 0 & 0 & 0 & 0 \\ 0 & h_+ & h_\times & 0 \\ 0 & h_\times & -h_+ & 0 \\ 0 & 0 & 0 & 0 \end{pmatrix}, \tag{2.21}$$

where $k = k_0$, $h_+ = A_{xx}$, and $h_\times = A_{xy}$. This equation means that there are two independent constants h_+ and $h_\times$. The angular frequency of the gravitational waves is written as $\omega = ck$.

[6] TT gauge condition is described by

$$A^\alpha{}_\alpha = 0$$
$$A_{\mu\nu} U^\nu = 0,$$

where U^ν is any constant timelike unit vector.

[7] U^ν is selected to be $U^\nu = \delta^\nu{}_0$.

2.1.4 Effect of gravitational waves on free particles

Here we describe the effect of gravitational waves on a free particle. A free particle obeys the geodesic equation

$$\frac{d}{d\tau}U^\mu + \Gamma^\mu{}_{\alpha\beta}U^\alpha U^\beta = 0, \tag{2.22}$$

where U^μ is the four velocity of the particle, and τ is the proper time. We consider the motion of this particle in a background Minkowski space time where the particle is initially at rest, under the TT gauge condition. The initial condition for U^μ is

$$(U^\mu)_0 = (1, 0, 0, 0) \tag{2.23}$$

Substituting Eqs. (2.12) and (2.23) to Eq. (2.22), and considering that $\bar{h}_{\alpha 0} = 0$ (here we consider the gravitational waves described by Eqs. (2.20) and (2.21)), the initial four accelerations of the particle is

$$\begin{aligned}\left(\frac{dU^\mu}{d\tau}\right)_0 &= -\Gamma^\mu{}_{00} = -\frac{1}{2}\eta^{\mu\alpha}(\bar{h}_{\alpha 0,0} + \bar{h}_{0\alpha,0} - \bar{h}_{00,\alpha}) \\ &= 0.\end{aligned} \tag{2.24}$$

This equation shows that the particle initially at rest does not change its position in the TT gauge. In order to see the effect of gravitational waves, consider the proper length between nearby particles (P_1 and P_2) which have the position $(0, 0, 0)$ and $(\epsilon, 0, 0)$ ($|\epsilon| \ll 1$) in the TT gauge, respectively. When gravitational waves described by Eqs. (2.20) and (2.21) incident on these particles, the proper distance between P_1 and P_2 changes as

$$\begin{aligned}\int_{\mathrm{P}_1}^{\mathrm{P}_2} |g_{\mu\nu}dx^\mu dx^\nu|^{\frac{1}{2}} &= \int_0^\epsilon |g_{xx}|^{\frac{1}{2}}\, dx \simeq |g_{xx}(\mathrm{P}_1)|^{\frac{1}{2}}\,\epsilon \\ &\simeq \left[1 + \frac{1}{2}\bar{h}_{xx}(\mathrm{P}_1)\right]\epsilon.\end{aligned} \tag{2.25}$$

This equation show that the gravitational wave changes the proper distance between two free particles. Thus, gravitational waves can be detected by monitoring the distance between free particles.

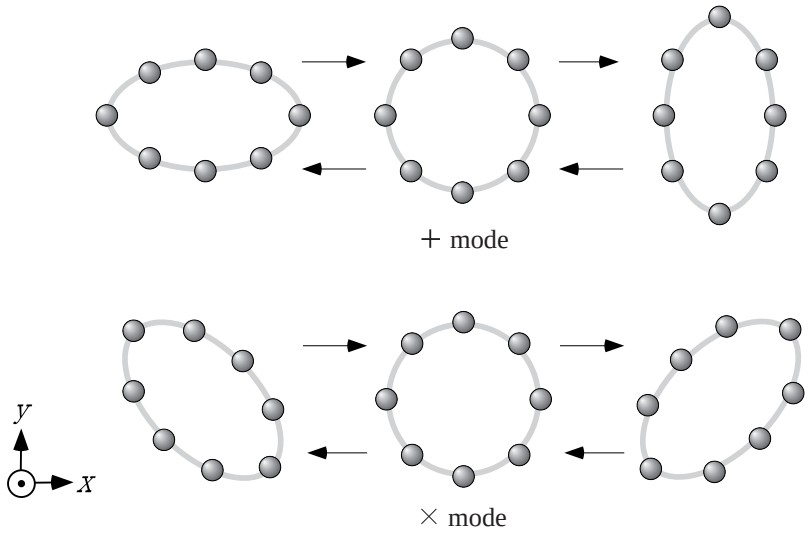

Figure 2.1: Distortions of a circle of free particles caused by gravitational waves incident from the perpendicular direction of this paper. The upper and lower figures show the distortions by +mode waves and ×mode waves, respectively.

2.1.5 Polarization

In order to investigate the effect of gravitational waves on free particles, we consider the case that the particles P_1 and P_2 are separated by an infinitesimal vector ξ^i.

From Eq. (2.22), the equation of geodesic deviation is described

$$\frac{d^2}{d\tau^2}\xi^i = R^i{}_{\alpha\beta j}U^\alpha U^\beta \xi^j \tag{2.26}$$

Taking to the first order of $\bar{h}_{\mu\nu}$ under consideration[8], Eq. (2.26) is written as

$$\frac{1}{c^2}\frac{\partial^2}{\partial t^2}\xi^i = -R^i{}_{0j0}\xi^j. \tag{2.27}$$

[8]In this approximation,

$$U^\alpha \simeq (1,0,0,0)$$
$$\tau \simeq ct.$$

In addition, since

$$R^{i}{}_{0j0} = -\frac{1}{2c^2}\frac{\partial^2 \bar{h}^{i}{}_{j}}{\partial t^2}$$

is satisfied under the TT gauge condition, Eq. (2.27) is written as

$$\frac{\partial^2}{\partial t^2}\xi^i = \frac{1}{2}\frac{\partial^2 \bar{h}^{i}{}_{j}}{\partial t^2}\xi^j. \tag{2.28}$$

Solving this equation so as not to get infinity in $t \to \infty$, we obtain

$$\delta\xi^i = \frac{1}{2}\bar{h}^{i}{}_{j}\xi^j, \tag{2.29}$$

where $\delta\xi^i$ is the deviation of ξ^i.

When gravitational waves propagating in the z-direction incident on these particles, $\bar{h}_{\mu\nu}$ is represented by Eqs. (2.20) and (2.21). Thus, we obtain

$$\begin{pmatrix} \delta\xi^x \\ \delta\xi^y \end{pmatrix} = \frac{1}{2}h_+ \begin{pmatrix} \xi^x \\ -\xi^y \end{pmatrix} e^{\mathrm{i}k(ct-z)} + \frac{1}{2}h_\times \begin{pmatrix} \xi^y \\ \xi^x \end{pmatrix} e^{\mathrm{i}k(ct-z)}. \tag{2.30}$$

In Eq. (2.30), the first and second terms represents the two polarizations of gravitational waves (+ mode and $\times$ mode, respectively). The names of the polarizations correspond to the shape of the deviations of the particles initially arranged in circle in x-y plane (Fig. 2.1).

2.2 Generation of gravitational waves

2.2.1 Radiation of gravitational waves

The radiation of gravitational waves is explained in an analogy of the radiation of electro-magnetic waves. Gravitational waves are radiated from accelerated masses as electro-magnetic waves are radiated from accelerated charges. While the dominant contribution to the electro-magnetic-wave radiation comes from the time variation of the electric dipole moment, the gravitational dipole radiation are forbidden by the conservation laws of momentum and angular momentum.

In a typical case that the motion within the source is slow enough compared with the speed of light (a slow-motion approximation), the gravitational wave radiation is contributed by the time variation of the gravitational quadrupole

moment. To describe the gravitational wave, we use a reduced quadrupole moment defined by

$$I(t) = \int \rho(t, \mathbf{x}) \left(x_i x_j - \frac{1}{3} \delta_{ij} x^i x^j \right) d^3x, \tag{2.31}$$

where $\rho(t, \mathbf{x})$ is a mass density. The radiated gravitational wave is written using the second derivative of $I_{ij}(t)$ with respect to the time:

$$\bar{h}_{ij}(t) = \frac{2G}{c^4 r} \ddot{I}_{(t-\frac{r}{c})}, \tag{2.32}$$

where r is the distance from the observation point to the source. From the above equation, the gravitational wave propagating along the z-direction is written as

$$h_+(t) = \frac{2G}{c^4 r} \frac{\ddot{I}_{11}(t-\frac{r}{c}) - \ddot{I}_{22}(t-\frac{r}{c})}{2}$$
$$h_\times(t) = -\frac{2G}{c^4 r} \ddot{I}_{12}(t-\frac{r}{c}),$$

The luminosity of the gravitational waves (the averaged energy flux) is written as

$$\mathcal{L}_{\mathrm{GW}} = \frac{G}{5c^5} \left\langle \sum_{ij} \dddot{I}_{ij}^2 \right\rangle. \tag{2.33}$$

2.2.2 Sources of gravitational waves

If gravitational waves could be generated artificially, it would be possible to test their existence and to study their nature. However, it is quite difficult to generate gravitational waves strong enough for laboratory experiments[9]. Thus, the experimental studies of gravitational waves is directed toward the natural sources, in particular toward the astronomical sources.

Here we estimate roughly the amplitude of gravitational waves from astronomical sources. Writing $\ddot{I}_{ij}$ by a corresponding mass energy[10], $\ddot{I}_{ij} = M_{\mathrm{q}} c^2$, the

[9] As an example, we consider gravitational waves from a rotating dumbbell (two massive balls connected with a bar). The radiated energy is $\mathcal{L}_{\mathrm{GW}} \sim 10^{-27}$ erg/s (10^{-34} W), when the weight of the masses is 100 kg, length of the bar is 2 m, and the rotation frequency is 100 Hz. The amplitude of the gravitational wave from this dumbbell is $\bar{h}_{ij} \lesssim 10^{-43}$ [34].

[10] The second derivative of a quadrupole momentum $\ddot{I}_{ij}$ has a dimension of energy:

$$\ddot{I}_{ij} \sim \frac{(\text{mass in motion}) \times (\text{system size})^2}{(\text{system transit time})^2} \sim (\text{quadrapole kinetic energy}).$$

amplitude of the radiated gravitational wave is described from Eq. (2.32) as

$$\bar{h}_{ij} \sim 5 \times 10^{-21} \left(\frac{M_{\rm q}}{M_\odot} \right) \left(\frac{20 \text{ Mpc}}{r} \right), \tag{2.34}$$

where $M_\odot$ is the mass of the sun. The value $r \sim 20$ Mpc is the distance to the Virgo cluster. A few bursts of gravitational waves at high frequency (less than a few kilohertz) are expected in a year among the galaxies included within a 20 Mpc sphere, which could be detected with ground-based detectors.

Expected main gravitational wave sources [3, 34, 35, 36] are described below. Here the sources are classified by the waveform: burst waves, periodic waves, and stochastic waves.

Burst sources

Bursts of gravitational waves are generated by supernova explosions, coalescence of compact binaries, stars falling into super massive black holes, and so on.

One type of supernova explosions is triggered by the collapse of a stellar core to a neutron star, when the star has exhausted its supply of nuclear fuel. Gravitational waves are expected to be generated in the explosion and in the instability after the explosion. Supernova events are estimated to occur a few times per century in our galaxy ($h \sim 10^{-18}$), and a few times per year within 20 Mpc distance ($h \sim 10^{-21}$). The frequency of the radiated gravitational waves is expected to be below a few kilohertz. Burst gravitational waves are also radiated in star collapses to black holes. The event rate is not well known; the upper limit for the collapse-formation of super massive black holes is a few per year in 3 Gpc.

The other reliable gravitational wave sources are coalescing compact binaries composed of compact stars as neutron stars (NSs) and black holes (BHs). A binary system loses its orbital energy, radiating periodic gravitational waves. Then, at last, the compact objects collide and coalesce, radiating a strong quasi-periodic gravitational waves in a few minutes. The gravitational waves from a coalescence binary have the waveform of 'chirp'; both frequency and amplitude increase with time. The event rate of coalescence of neutron star binaries is estimated to be about a few times per year within 200 Mpc. In the last 15 minutes, the waves from coalescing NS-NS binaries will have frequencies from about 10 Hz up to a few kHz, and will radiate gravitational waves with an amplitude of $h \sim 10^{-21}$.

Strong gravitational waves will be also radiated from coalescence of massive black hole (MBH) binaries. Their event rate is estimated to be once per year within a distance of 3 Gpc. Gravitational waves from a MBH-MBH binary at this distance will have a chirp waveform sweeping upward from $h \sim 10^{-20}$ at 10^{-4} Hz to $h \sim 10^{-18}$ at 10^{-2} Hz in the final year of coalescence for MBHs with a mass of $10^5 M_\odot$.

Burst waves are also radiated from stars spiraling into MBHs thought to inhabit galactic nuclei. The frequency of the radiated waves is around 10^{-3} Hz for a MBH of $10^7 M_\odot$; the waveform is strongly influenced by the spin of the MBH. The amplitude would be $h \sim 10^{-22}$ for a $1 M_\odot$ star spiraling into MBH at a distance of 20 Mpc. Though the event rate is not well known, it will be reasonable in a 20 Mpc range, which contains ∼100 galaxies.

Periodic sources

Periodic gravitational waves are radiated from binary stars and from rotating neutron stars (pulsars).

Binary star systems are certain sources of continuous gravitational waves; the waveform is computed with confidence from the measured mass and orbital parameters. In addition, gravitational waves from a neutron star binary have been observed indirectly (described in the following Section). In order to radiate strong periodic gravitational waves, the binary systems must be comprised of compact stars: white dwarfs (WD), neutron stars, or black holes. WD-WD binaries are thought to be so numerous in our galaxy that they will not resolvable. They are considered to form a stochastic background with an amplitude of $h \sim 10^{-21}$ around 10^{-3} Hz. However, there thought to be a large number of resolvable sources with higher frequency or larger amplitude than the background. Considering a NS-NS binary in our galaxy ($\sim$ 10 kpc), gravitational waves with $h \simeq 4 \times 10^{-22}$ will be radiated at a frequency of 5×10^{-3} Hz. The effective amplitude of these waves is 2×10^{-19} with one year of integration time.

When a single rotating neutron star deviates from axisymmetry about its principle axis, it will radiate gravitational waves at twice its rotation frequency, and at the beat frequency of the rotation and precessional frequencies. The amplitude is estimated to be $h \sim 10^{-25}$ for a pulsar at 1 kpc distance with a rotation

frequency of 200 Hz and an ellipticity of 10^{-6} in the equatorial plane. Though the amplitude is rather small, the signal can be enhanced with a long integration time because the rotation frequency is precisely known by the electromagnetic observation of the pulsar. The effective signal is enhanced by the square root of the number of cycles, by a factor of 10^4 in a one week observation period for 200 Hz waves.

Stochastic sources

Besides the background caused by the dense galactic binary systems, a stochastic background of gravitational waves is expected to be produced in the big bang, in phase transitions in the early universe, and from cosmic strings.

One of the predicted origins of the stochastic background of gravitational waves is the big bang itself; these background waves are called primordial gravitational waves. It is estimated that that the gravitational waves have not interacted with matter since the Planck era, when space and time came into being, and that primordial gravitational waves should not have been thermalized by interactions with matter. On the other hand, the gravitational waves emerged from the big bang are considered to have interacted with the subsequent, early-time expansion of the universe to produce a stochastic background today.

The cosmological gravitational wave background is often discussed in terms of $\Omega_{\rm g}(f)$, the energy density per logarithmic frequency interval relative to the closure density (the critical energy density necessary to close the universe). The RMS amplitude of the fluctuating gravitational waves in a bandwidth of f at a frequency of f is expressed by $\Omega_{\rm g}$ in the relation $h \sim 1 \times 10^{-18}\sqrt{\Omega_{\rm g}}\,(1\ {\rm Hz}/f)$, assuming a Hubble constant of 75 $\mathrm{km \cdot s^{-1} \cdot Mpc^{-1}}$. The observation of the cosmic microwave radiation sets a limit of $\Omega_{\rm g} \leq 10^{-9}$ at 10^{-18} Hz.

A stochastic background could also have been produced by phase transitions associated with QCD interactions and with electroweak interactions during the early expansion of the universe. If the collision of vacuum bubbles have occurred in the electroweak phase transition, the gravitational wave background might have a density of $\Omega_{\rm g} \sim 3 \times 10^{-7}$ around 0.1 mHz.

It is suggested that cosmic strings have been created in a phase transition associated with the grand-unified interactions long before the QCD and electroweak

phase transitions. The vibrations of the cosmic strings would produce gravitational waves with almost a flat spectrum of Ω_g independent of the frequency. The suggested waves have a strength of $\Omega_g \sim 10^{-7}$, which is already constrained by pulsar timing observations.

2.2.3 Evidence of the existence of a gravitational wave

The existence of a gravitational wave has been confirmed by the observation of a binary pulsar. In 1974 the binary pulsar PSR 1913+16 was found by R. A. Hulse and J. H. Taylor [4]. From the observed parameters of this system, including orbital precession, gravitational red shift, and radiation time delay, nearly all of the relevant properties of this binary system are determined. In particular, the masses of the pulsar and the companion star have been determined in a very good precision[11].

PSR 1913+16 shows the self-consistency of the General Theory of Relativity in a very good precision. One of the most important results from the observation of this binary system is the change in the orbital period due to the radiation of gravitational waves [5, 6]. The binary system radiates gravitational waves in the radiation rate described in Eq. (2.33). Since the orbital energy is carried away by the gravitational wave radiation, the orbital period of the binary system decreases. The observed change in the orbital period agrees with that predicted by the General Theory of Relativity within the experimental accuracy, better than one per cent.

2.3 Detection of gravitational waves

2.3.1 Physical and astronomical aims

The existence of gravitational waves has been predicted theoretically, and confirmed by the observation of a neutron-star binary. However, gravitational waves have not been detected directly, because of the weakness of gravitational interactions. The detection of gravitational waves is one of the most important tasks

[11]The 1993 Nobel Prize in Physics was awarded to R. A. Hulse and J. H. Taylor for their discovery of the binary pulsar and indirect observation of a gravitational wave.

left for us in order to verify the General Theory of Relativity. In addition, the detection of gravitational waves has a possibility to open a new observation window to the universe. The information obtained from the waveform of gravitational waves is different in quality from that of electro-magnetic waves: since gravitational waves transmits almost everything, they inform us about the dynamic motion of astronomical objects. It is expected that the waveform of gravitational waves might give us information such as: the Hubble constant, the state equation of a neutron star, the mechanism of supernova explosions, understandings of the strong gravitational field, and information about the early universe.

The attempt to detect gravitational waves is pioneered by J. Weber [7, 8]. He used resonant-type detectors, which detect the vibration of massive metal bars excited by gravitational waves at their resonant frequency. Currently, laser interferometric detectors [9] are investigated and constructed vigorously. An interferometric detector measures the distance between free-falling masses perturbed by gravitational waves. One of the advantages of an interferometric detector is its broad observation band, which enables us to observe the waveform of gravitational waves. While resonant-type detectors and interferometric detectors on the ground aim at high frequency (10 Hz $\sim$ 1 kHz) gravitational waves, lower frequency gravitational waves are tried to detect by a Doppler tracking method, a space interferometer ($10^{-4} \sim 10^{-1}$ Hz), and a pulsar timing method ($10^{-9} \sim 10^{-7}$ Hz). At extremely low frequencies ($10^{-18} \sim 10^{-15}$ Hz), the gravitational waves would be measured as quadrupolar anisotropies in the cosmic microwave background.

2.3.2 Resonant-mass detectors

Principle of a resonant-type detector

A resonant-type detector is comprised of a massive elastic body (an antenna) and a vibration detector (a transducer) [7]. A part of the energy of incident gravitational waves is converted to vibration energy of the elastic body. A transducer detects the vibration as a gravitational wave signal.

Ideally, a resonant-type detector is modeled by two point particles (mass m) connected with a mass-less spring (with natural length l_0 and the spring constant $k_{\rm s}$) (Fig. 2.2). Considering only the first order of $\bar{h}_{\mu\nu}$, the deviation of the distance

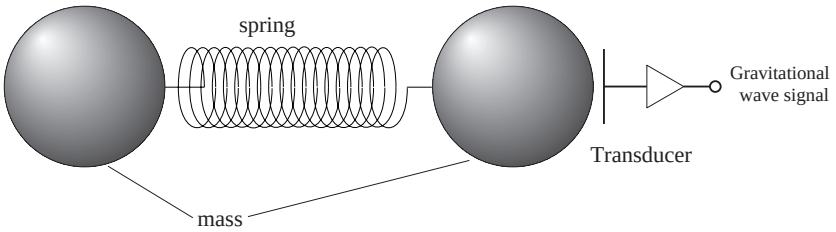

Figure 2.2: Resonant-type gravitational waves detector, modeled by two masses connected with a spring. Gravitational waves excite the oscillator, which is detected with a transducer.

of two particles $\delta\xi^\mu$ is written as

$$\frac{\partial^2\delta\xi^i}{\partial t^2} + \frac{\omega_0}{Q}\frac{\partial\delta\xi^i}{\partial t} + {\omega_0}^2\delta\xi^i = \frac{1}{2}\frac{\partial^2\bar{h}^i{}_j}{\partial t^2}\xi^j, \tag{2.35}$$

where Q is the quality factor (Q-value) of the resonance, and $\omega_0 = \sqrt{k_{\rm s}/m}$ is the resonant angular frequency of this system. Equation (2.35) represents a damped harmonic oscillator excited by a gravitational wave force[12]. When the frequency of the incident gravitational waves is near the resonant frequency of the detector, the vibration is excited efficiently.

The energy which the detector receives from the incident gravitational waves is proportional to the mass of the antenna, and to the square of the Q-value and l_0. Thus, the antenna is made of a few tons of metal with small losses (usually, aluminum or Niobium is used). The sensitivity is mainly limited by the thermal motion of the elastic body, and the readout noise of the transducer. In order to reduce the effect of the thermal noise, the detector is usually operated at cryogenic temperatures. In addition, low-noise transducers have been developed.

Development of resonant-mass detectors

Table 2.1 shows the operated and planned resonant-type detectors. The development of resonant-mass gravitational wave detectors is pioneered by J. Weber [7], and the sensitivities have been improved by a number of other research groups since then. Weber's detector consisted of two sets of bar-type resonant detectors

[12]In the limitation of $\omega_0 \to 0$ and $Q \to \infty$, the equation reduces to the deviation of free particles, Eq. (2.28).

Table 2.1: Operated and planned resonant-mass detectors.

Resonant-mass detectors					
Group	Detector name	Antenna	Transducer	Frequency	Sensitivity
Maryland	'Weber-bar'	Al bar	PZT	1660 Hz	10^{-16}
Rome	Explorer	Al bar	DC-SQUID	920 Hz	8×10^{-19}
LSU	Allegro	Al bar	DC-SQUID	910 Hz	6×10^{-19}
UWA	Niobe	Nb bar	RF cavity	710 Hz	7×10^{-19}
Frascati	Nautilus	Al bar	DC-SQUID	900 Hz	$(\sim 10^{-20})$
Legnaro	Auriga	Al bar	DC-SQUID	920 Hz	$(\sim 10^{-20})$
Stanford		Al bar	DC-SQUID	900 Hz	$(\sim 10^{-20})$
KEK	Crab IV	Al torsion	Capacitance	60 Hz	2×10^{-22}
ICRR		Al disk	FP cavity	1200 Hz	1×10^{-17}
LSU		TIGA		$1 \sim 2$ kHz	$(\sim 10^{-21})$

with PZT transducers operated at room temperature. In the second generation of the resonant-mass detectors, the antenna is cooled to the temperature of liquid helium (4.2 K) in order to reduce the thermal noise. At present, an observation network is formed with 'Explorer' at the University of Rome [37], 'Allegro' at Louisiana State University (LSU) [38], and 'Niobe' at the University of Western Australia (UWA) [39]. The third generation of resonant-mass detectors is now under construction: 'Nautilus' at the INFN Frascati Laboratories [40], 'Auriga' at the INFN Legnaro Laboratories [41], and one detector at Stanford University [42]. These detectors are cooled to less than 100 mK, resulting in a sensitivity of $h \sim 10^{-20}$.

Besides bar-type detectors, a torsion-type detector and a disk-type detector have been developed. The torsion-type detector has a lower resonant frequency, aiming at periodical gravitational waves from a particular pulsar. By 1900 hours of observation with the 'CRAB IV' detector at KEK in Japan, an upper limit of $h < 2 \times 10^{-22}$ has been set for periodic gravitational waves from the Crab pulsar [43]. A disk-type detector has been developed at ICRR in Japan [44]. A disk-type detector can be supported at the node of the resonance mode, which results in a high Q-value of the antenna.

The subsequent generation resonant-mass detectors will be 'sphere-shaped' detectors called TIGA (a truncated icosahedral gravitational wave antenna) [45, 46]. A TIGA has a larger cross section for gravitational waves. In addition, the source direction and polarization is determined with a TIGA. The discussed and planned detector is a network of antennas with different resonant frequencies ('xylophone'), cooled to 50 mK. The sensitivity of a 'xylophone' of TIGA detectors is expected to be $h \sim 10^{-21}$.

2.3.3 Interferometric detector

Principle of an interferometric detector

The principle of an interferometric gravitational wave detector is a Michelson interferometer (Fig. 3.1)[13]. As described in Section 2.1, the distance of free particles is perturbed by gravitational waves. The change in distance causes a phase change in the laser light (the phase of the laser beam is modulated by the gravitational waves), which is detected as change in the interference fringe of the Michelson interferometer.

The Michelson interferometer is comprised of a laser source, a beamsplitter, two mirrors, and a photo detector. In the interferometric detectors on the earth, the mirrors are suspended as pendulums so that they should behave as free masses in the direction along the laser beam at the observation frequency. The beam from the laser source is divided in two orthogonal directions (along x- and y-directions in Fig. 3.1) with a beamsplitter. The two beams are reflected back with mirrors and recombined on the beamsplitter, producing an interference fringe. Gravitational waves change the arm length (distance between a mirror and the beamsplitter) differentially, i.e., stretch one arm length and shrink the other[14]. This change appears as the change of the interference fringe and detected with a photo detector.

The sensitivity of an interferometric detector is limited by shot noise, thermal noise, and seismic noise. Since the effect of the shot noise is inversely proportional

[13]The details of an interferometric detector are discussed in the following Chapters.

[14]This point of view is true when the period of the gravitational waves is lower enough than the round trip time of the light in the arms.

Table 2.2: Currently operated prototype interferometers. FPM: a Fabry-Perot-Michelson interferometer.

Prototype interferometers			
Group	Baseline	Type	Displacement noise
Caltech	40 m	Locked Fabry-Perot	3×10^{-19} m/$\sqrt{\text{Hz}}$ (1994)
		Power-recycled FPM	—
MPQ	30 m	Delay-line Michelson	3×10^{-18} m/$\sqrt{\text{Hz}}$ (1988)
		Dual-recycled Michelson	—
Glasgow	10 m	Locked Fabry-Perot	6×10^{-19} m/$\sqrt{\text{Hz}}$ (1992)
NAO	20 m	Fabry-Perot Michelson	2×10^{-17} m/$\sqrt{\text{Hz}}$ (1996)
		Power-recycled FPM	—
Tokyo	3 m	Fabry-Perot Michelson	1×10^{-17} m/$\sqrt{\text{Hz}}$ (1994)
		Power-recycled FPM	2×10^{-17} m/$\sqrt{\text{Hz}}$ (1998)

to the square-root of the laser power, a power recycling technique is used together with a high-power laser source. The gravitational wave signal is proportional to the baseline length of an interferometer, while the thermal noise and seismic noise are independent of the baseline length. Thus, larger baseline length is desirable to reduce the effect of thermal noise and seismic noise.

Development of interferometric detectors

The real development of laser interferometric gravitational wave detectors was begun in the early 1970s [9, 10]. Since that time, several groups have pursued interferometric detectors, constructing tabletop interferometers and prototype interferometers with suspended optics. Table 2.2 summarizes the prototype interferometers under investigation currently. The prototype interferometers were used to investigate the principles of interferometric detectors and their noise behavior. In recent years, the configurations of these prototype interferometers have been changed to those resembling the real gravitational wave detectors: a power-recycled Fabry-Perot-Michelson interferometer or a dual-recycled Michelson interferometer.

Advanced techniques for future interferometers are under investigation now

Table 2.3: Laser interferometric gravitational wave detector projects. FP: Fabry-Perot type, DL: Delay-line type, PR: power recycling, DR: Dual recycling.

Interferometric gravitational wave detector projects				
Country	Project	Baseline length	Type	Observation
U.S.A.	LIGO	4 km × 2	FP (PR)	2001 ∼
Italy, France	VIRGO	3 km	FP (PR)	2002 ∼
Germany, U.K.	GEO	600 m	DL (DR)	2000 ∼
Japan	TAMA	300 m	FP (PR)	1999 ∼

with table-top and prototype experiments: better vibration isolation systems, mirror cooling techniques, and advanced optical configurations.

Interferometric detector projects

Table 2.3 shows the projects to construct laser interferometric gravitational wave detectors. LIGO is an American project to construct two interferometers with an baseline length of 4 km [11]. LIGO is planning coincidence detection and waveform analysis of gravitational waves with these two interferometers. VIRGO is a project by Italy and France [12]. VIRGO aims at low-frequency gravitational waves by adopting a multi-stage seismic isolation system. GEO is a project by Germany and U.K. [13]. The GEO interferometer is a delay-line-Michelson interferometer with dual recycling (power and signal recycling). The Japanese project to construct an interferometer with a baseline length of 300 m is called TAMA [14]. Though the sensitivity of TAMA will not be as good as interferometers with longer baseline lengths (like LIGO and VIRGO), TAMA will start the observation earlier than the other projects. All these four projects adopt the power recycling technique to increase the effective laser power so as to improve the shot-noise level of the interferometer.

Besides the interferometers on the earth described above, a space interferometric gravitational wave detector, called LISA [36], is planned by ESA and NASA. LISA will consist of three large interferometers with a baseline length of 5×10^6 km, formed by three spacecrafts. The spacecrafts are planned to be

launched in 2008 $\sim$ 2010.

2.3.4 Other types of gravitational wave detectors

Doppler tracking

Doppler tracking is a scheme to detect gravitational waves by the accurate measurement of the Doppler shift of microwave signals communicated between the earth and a spacecraft [47]. The output of a stable oscillator on the earth (typically with a frequency of a few MHz) is up-converted and transmitted to a spacecraft (up link). This up-linked microwave is sent back to the earth by the spacecraft (down link). The frequency of the down-linked microwave is measured by comparison with that of the master oscillator. The fundamental limitation to the sensitivity of the Doppler tracking scheme is given by the stability of the frequency reference. With the best available frequency standard (a hydrogen maser clock) the sensitivity is about $h \sim 10^{-15}$ (in 1000 sec). The observation band ($10^{-2} \sim 10^{-4}$ Hz) is restricted by the round-trip time of the radio signal to lower frequencies and by the thermal noise of the telecommunication system to higher frequencies.

In an observation about one month long using a ULYSSES spacecraft, the sensitivity was about

$$h \sim 1.3 \times 10^{-15} \left(\frac{f}{10^{-2}\ \mathrm{Hz}} \right)^{-0.26} \tag{2.36}$$

in the frequency band from 2.3×10^{-4} to 5×10^{-2} Hz [48, 49]. In this observation, the sensitivity was limited by the density fluctuations of the inter-planetary plasma. It is possible to reduce this noise by using multi-frequency or higher frequency radio links. In a planned mission (CASSINI), the plasma noise will be decreased by a factor about 250 using higher frequency radio links. With the improvements in the reference clock and telecommunication system, the sensitivity of CASSINI will be $h \sim 7 \times 10^{-16}$.

Laser interferometer in space

The observation band of a ground-based interferometric detector is limited by the seismic noise at lower frequencies, where several strong gravitational wave

sources are expected: periodic waves from binaries and pulsars, and burst waves from MBHs. A mission named LISA (Laser Interferometer Space Antenna) is planned targeting these low frequency gravitational waves ($10^{-4} \sim 1$ Hz) [36]. In LISA, a triangle interferometer with a baseline length of 5×10^6 km will be formed by three spacecraft in an earth-like heliocentric orbit, following 20 degrees behind the earth. The spacecraft will monitor the distance to one another using laser beams in a similar way as the RF transponder scheme.

LISA will have a sensitivity of $h \sim 10^{-21}$ at 10^{-3} Hz with a bandwidth of 10^{-3} Hz; the sensitivity will be improved much more than that of the Doppler tracking scheme. The sensitivity of LISA is limited by the optical-path noise (shot noise, master clock noise, residual laser phase noise, beam pointing instabilities, and so on) and the forces acting on the proof masses (thermal distortion of space craft, thermal noise due to dielectric losses, electrical force on charged proof masses, residual gas impacts on proof masses, and so on).

LISA is envisaged as a NASA/ESA collaborative project. The mission is aimed at a launch in the 2008∼2010 time frame.

Pulsar timing

Since arrival times of the radio pulses from millisecond and binary pulsars are measured with a very high accuracy, their fluctuations can be used for the detection of gravitational waves [50, 51]. The effect of gravitational waves passing by a pulsar or by the earth appears in the differences of the observed pulse arrival times and those predicted by the pulsar spindown and so on. The observation target of pulsar timing is a low-frequency ($10^{-7} \sim 10^{-9}$ Hz) stochastic gravitational wave radiation background, which may be generated in the early universe, or may exist as the superposition of many low-frequency sources.

The statistical analysis of the pulsar timing data of PSR B1855+09 yields an upper limit of 9×10^{-8} for $\Omega_{\rm g}$ in a frequency range of $4 \times 10^{-9} \sim 4 \times 10^{-8}$ Hz [52]. The observation band is determined by the total observation time (lower frequency limit) and sufficient integration time of the pulse arrival times (upper frequency limit). This value corresponds to $h \sim 3 \times 10^{-14}$ at a frequency of 10^{-8} Hz.

The sensitivity of pulsar timing is limited by the stability of the pulsar, the

long-term frequency stability of the reference clock, and the observation time. The upper limit of Ω_g is improved with the fifth power of the observation time. An observation network with stable pulsars would alleviate problems with the reference clock and the effect of the other noise source, inter-stellar scintillation [3].

Chapter 3

Interferometric gravitational wave detector

Laser interferometric gravitational wave detectors have been investigated and developed energetically in recent years. This is because an interferometric detector has a wide observation band, and its potential high sensitivity with a long baseline length of a few kilometers. In this Chapter, we describe the fundamentals of an interferometric gravitational wave detector: its characteristics and its noise sources.

An interferometric gravitational wave detector is comprised of several optical devices: a Michelson interferometer and cavities. In the LIGO, VIRGO, and TAMA detectors, the interferometer is formed with a Michelson interferometer, Fabry-Perot arm cavities, and the recycling cavity. In the first half of this Chapter, the fundamentals of each optical device are described (a Michelson interferometer, a Fabry-Perot cavity, and a power recycling technique). In the latter half, the noise sources of an interferometric gravitational wave detector are described. This Chapter contains the following Sections.

- **Michelson interferometer.** The principle of of gravitational wave detection with a Michelson interferometer. The frequency response of a Michelson interferometer and its optimization with delay lines or Fabry-Perot cavities.

- **Fabry-Perot cavity.** The fundamentals of a Fabry-Perot cavity. The

response to a gravitational wave, displacement of a mirror, and fluctuation of incident laser frequency.

- **Power recycling.** The principle of power enhancement with power recycling. The characteristics of a power recycling cavity.

- **Noise sources for an interferometer.** Noise sources which can limit the sensitivity of an interferometric gravitational wave detector.

3.1 Michelson interferometer

The principle of an interferometric gravitational wave detector is a Michelson interferometer. The arm length of a Michelson interferometer[1] is perturbed by gravitational waves, which cause phase changes in the laser beams reflected back with the end mirrors. Gravitational waves with suitable polarization will change the arm lengths differentially because of the quadrupolar nature of gravitational waves. The resulting differential phase change is detected as change in the interference fringe.

The phase changes caused by gravitational waves are proportional to the arm length of a Michelson interferometer when the period of gravitational waves is long enough comparing with the storage time of the laser beam in the Michelson arm. On the other hand, the phase change caused by shorter period gravitational waves does not increase with the baseline length because of cancellation of phase changes. Thus, there is an optimal baseline length depending on the frequency of target gravitational waves. The optimal baseline length for gravitational waves with a frequency of 1 kHz would be about 75 km. However, it is difficult to construct such a long-baseline interferometer because of practical problems. In order to optimize the frequency response of the interferometer, the effective baseline length[2] is usually extended by a delay-line or a Fabry-Perot cavity.

[1]The two orthogonal optical paths of the Michelson interferometer are called 'arms' of the Michelson interferometer. The 'arm length' represents the distance between the beamsplitter and the end mirror.

[2]The effective baseline length of a Michelson interferometer $L_{\rm eff}$ is defined by $L_{\rm eff} = \tau c$, where τ is the storage time of the laser light in the arm (the storage time of the signal sidebands).

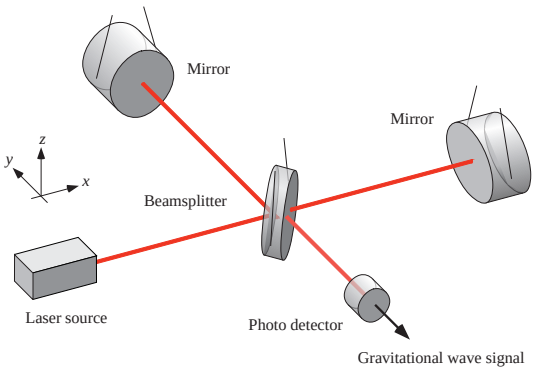

Figure 3.1: The principle of a laser interferometric gravitational wave detector is a Michelson interferometer; gravitational waves are detected as the changes in the interference fringe. The mirrors are suspended as pendulum to behave as free masses at observation frequencies.

3.1.1 Phase detection with a Michelson interferometer

Figure 3.1 shows a Michelson interferometer for detection of gravitational waves. The laser beam from the source is divided with a beamsplitter in two orthogonal directions (along x- and y-directions in Fig. 3.1). These beams are reflected with mirrors and recombined on the beamsplitter. Gravitational waves cause differential phase changes in two orthogonal optical paths of the Michelson interferometer, which are detected as the changes in the interference fringe at the photo detector.

We write the beam from the laser source as

$$E_{\rm l} = E_0 e^{{\rm i}\Omega_{\rm l} t}, \tag{3.1}$$

where E_0 and $\Omega_{\rm l}$ are the amplitude and angular frequency of the laser beam. The beams reflected from two arms are recombined on the beamsplitter after experiencing the phase changes ϕ_x and ϕ_y and the amplitude changes r_x and r_y in the arms of the Michelson interferometer[3]. The electro-magnetic field detected

[3] r_x and r_y include the amplitude changes at the beamsplitter, i.e., the reflectivity and transmissivity of the beamsplitter.

at the photo detector is written by

$$E_{\mathrm{PD}} = r_x E_0 e^{\mathrm{i}(\Omega_{\mathrm{l}} t - \phi_x)} - r_y E_0 e^{\mathrm{i}(\Omega_{\mathrm{l}} t - \phi_y)}.$$

Thus, the power detected by the photo detector is

$$P_{\mathrm{PD}} = |E_{\mathrm{PD}}|^2 = \frac{P_{\max} + P_{\min}}{2} - \frac{P_{\max} - P_{\min}}{2} \cos\phi_-, \tag{3.2}$$

where ϕ_- is the difference of the phases

$$\phi_- = \phi_x - \phi_y. \tag{3.3}$$

$P_{\max}$ and $P_{\min}$ represent the maximum and minimum power of the interference fringe, in other words, the bright fringe and dark fringe power. Equation (3.2) shows that the Michelson interferometer detects the phase difference of the beams in two arms from a power on the photo detector.

The interference efficiency is often represented by a contrast C defined by

$$C \equiv \frac{P_{\max} - P_{\min}}{P_{\max} + P_{\min}}. \tag{3.4}$$

In an ideal case ($r_x = r_y$ and the interferometer is perfectly aligned), $P_{\min}$ becomes zero, and the contrast becomes unity. When $\phi_- = 0$, the laser beams from both arms interfere destructively, and the interference fringe get completely dark. In addition, when no power is lost in the interferometer, the power on the photo detector is written in a simpler expression as

$$P_{\mathrm{PD}} = \frac{1}{2} P_{\mathrm{l}} (1 - \cos\phi_-), \tag{3.5}$$

where P_{l} is the power of the incident laser beam: $P_{\mathrm{l}} = |E_{\mathrm{l}}|^2$.

3.1.2 Detection of gravitational waves

Gravitational waves cause differential phase change in two arms of the Michelson interferometer. Here, we consider the phase change caused by a +-polarized gravitational wave propagating along the z-direction.

The proper distance of the photon traveling along the x-axis satisfies the equation

$$ds^2 = -c^2 dt^2 + \{1 + h_+(t)\} dx^2 = 0.$$

With an approximation of $h_+(t) \ll 1$, we get[4]

$$\{1 - \frac{1}{2}h_+(t)\}c\ dt = dx.$$

Integrating both sides of this equation, we get the equation for the round-trip time of a photon between the beamsplitter and the mirror Δt_x:

$$\Delta t_x = \frac{2\xi^x}{c} + \frac{1}{2}\int_{t-\frac{2\xi^x}{c}}^{t} h_+(t')dt', \tag{3.6}$$

where ξ^x is the distance between the beamsplitter and the mirror[5].

Thus, the round-trip phase change in the photon traveling along the x-direction is written as

$$\phi_x = \Omega_{\rm l}\Delta t_x = \frac{2\xi^x\Omega_{\rm l}}{c} + \frac{\Omega_{\rm l}}{2}\int_{t-\frac{2\xi^x}{c}}^{t} h_+(t')dt'. \tag{3.7}$$

The gravitational wave causes a phase change in the opposite sign for the photon traveling along the y-direction:

$$\phi_y = \Omega_{\rm l}\Delta t_y = \frac{2\xi^y\Omega_{\rm l}}{c} - \frac{\Omega_{\rm l}}{2}\int_{t-\frac{2\xi^y}{c}}^{t} h_+(t')dt'. \tag{3.8}$$

Thus, the phase difference caused by the gravitational wave is written from Eqs. (3.7) and (3.8)

$$\delta\phi_{\rm GR} = \Omega_{\rm l}\int_{t-\frac{2l}{c}}^{t} h_+(t')dt', \tag{3.9}$$

assuming that the arm lengths of the Michelson interferometer are equal: $l = \xi^x = \xi^y$. This phase difference is detected as the change in the interference fringe of the Michelson interferometer.

When the changes in the incident gravitational waves are much slower than the storage time in the arm $2l/c$, Eq. (3.9) is written as

$$\delta\phi_{\rm GR} \simeq \frac{2l\Omega_{\rm l}}{c}h_+ = \frac{4\pi l}{\lambda_{\rm l}}h_+, \tag{3.10}$$

where $\lambda_{\rm l}$ is the wavelength of the incident laser beam.

[4]We select the sign $dx/dt > 0$.

[5]Here, we again use the approximation of $h_+(t) \ll 1$.

3.1.3 Frequency response and baseline length

Though the sensitivity of a Michelson interferometer increases with a larger baseline length for low-frequency gravitational waves, it does not increase for a high frequency gravitational waves because of cancellation of the phase changes. Thus, a Michelson interferometer has an optimal baseline length corresponding to the target frequency of gravitational waves.

By a Fourier transformation of $h_+(t)$,

$$h_+(t) = \int_{-\infty}^{\infty} h_+(\omega) e^{\mathrm{i}\omega t} d\omega. \tag{3.11}$$

Substituting this equation into Eq. (3.9),

$$\delta\phi_{\mathrm{GR}} = \Omega_{\mathrm{l}} \int_{t-\frac{2l}{c}}^{t} dt' \int_{-\infty}^{\infty} d\omega h_+(\omega) e^{\mathrm{i}\omega t'} = \int_{-\infty}^{\infty} H_{\mathrm{MI}}(\omega) h_+(\omega) e^{\mathrm{i}\omega t} d\omega, \tag{3.12}$$

where $H_{\mathrm{MI}}(\omega)$ is written by

$$H_{\mathrm{MI}}(\omega) = \frac{2\Omega_{\mathrm{l}}}{\omega} \sin\left(\frac{l\omega}{c}\right) e^{-\mathrm{i}\frac{l\omega}{c}}. \tag{3.13}$$

$H_{\mathrm{MI}}(\omega)$ represents the sensitivity of the Michelson interferometer to gravitational waves with an angular frequency of ω.

In an approximation that the period of a gravitational wave ($2\pi/\omega$) is much longer than the storage time in the arm of the Michelson interferometer ($\tau = 2l/c$), the absolute value of the response is written as $|H_{\mathrm{MI}}| \sim 2\Omega_{\mathrm{l}} l/c$; the phase change caused by gravitational waves is proportional to the baseline length l. This is because the effect of gravitational waves accumulates during the storage time of the photon in the arms of the Michelson interferometer. On the other hand, the sensitivity to higher frequency gravitational waves does not increase with a larger baseline length because the effects of gravitational waves are integrated and canceled out.

From Eq. (3.13), we can see that the sensitivity of the Michelson interferometer is maximized when the baseline length l satisfies

$$\frac{l\omega_{\mathrm{obs}}}{c} = \frac{\pi}{2}, \tag{3.14}$$

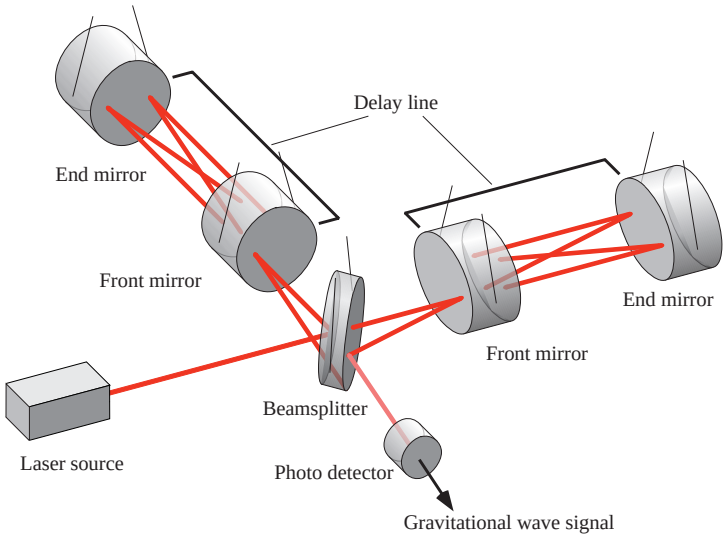

Figure 3.2: Michelson interferometer with delay-line arms. The laser beam is bounced between the mirrors; here, the bounce number (N_{DL}) is 4.

for a given angular frequency ω_{obs} of the gravitational waves. This equation shows that the optimal storage time in the arm of the Michelson interferometer is half of the period of the target gravitational waves[6].

The optimal baseline length for gravitational waves with a frequency of 1 kHz is about 75 km. This is an unrealistic value for a ground-based interferometer because of practical problems: the high cost to construct long vacuum tubes and the difficulty to find a site for the interferometer. Thus, several optical configurations have been proposed to optimize the frequency response of an interferometer with a realistic baseline length of a few kilometers by increasing the signal storage time, in other words, by extending the effective baseline length.

3.1.4 Optimization of the frequency response

In order to extend the effective arm length and to optimize the frequency response, two schemes are proposed[7]: a delay-line scheme and a Fabry-Perot scheme.

[6]In other words, this condition is written that the optical path length is optimized when it is half of the wavelength of target gravitational waves.

[7]It is also possible to optimize the frequency response by the use of a signal recycling technique. This scheme is reviewed in Section 3.3.

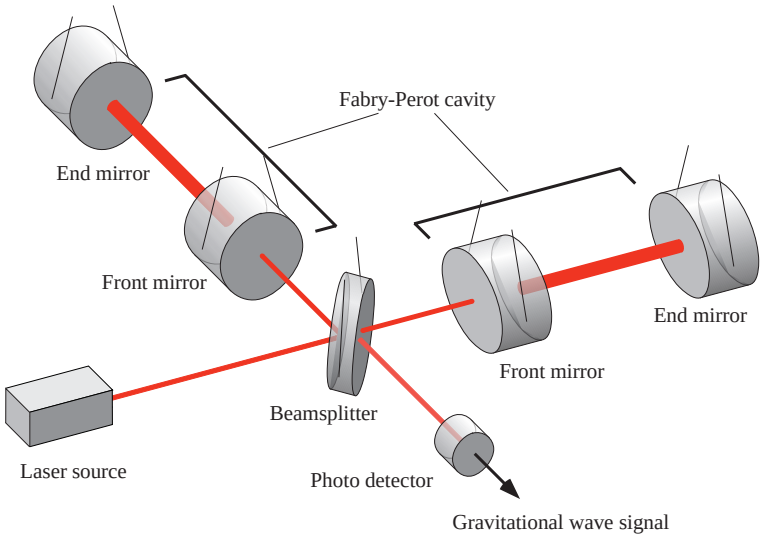

Figure 3.3: Michelson interferometer with Fabry-Perot arm cavities. The beam is stored in the cavity by multi-interference.

The effective arm length can be extended with an optical delay line, folding the optical path by multiple reflections. In a delay-line-Michelson interferometer (Fig. 3.2), the total optical path length $L_{\rm DL}$ is written as $L_{\rm DL} = N_{\rm DL} l_{\rm DL}$, where $N_{\rm DL}$ is the number of the optical path ($N_{\rm DL}-1$ reflections), and $l_{\rm DL}$ is the distance between two mirrors forming the delay lines[8].

The expressions for the frequency response of a delay-line-Michelson interferometer $H_{\rm DLMI}(\omega)$ is obtained by replacing $2l$ of $H_{\rm MI}(\omega)$ in Eq. (3.13) by $L_{\rm DL}$:

$$H_{\rm DLMI}(\omega) = \frac{2\Omega_{\rm l}}{\omega} \sin\left(\frac{L_{\rm DL}\omega}{2c}\right) e^{-{\rm i}\frac{L_{\rm DL}\omega}{2c}}. \tag{3.15}$$

The effective arm length can also be extended by the multiple interference of a Fabry-Perot cavity. In a Fabry-Perot-Michelson interferometer, the mirrors of a Michelson interferometer are replaced by Fabry-Perot cavities (Fig. 3.3). The frequency response of a Fabry-Perot-Michelson interferometer $H_{\rm FPMI}(\omega)$ is written as

$$H_{\rm FPMI}(\omega) = \frac{2a_{\rm cav}\Omega_{\rm l}}{\omega} \frac{\sin\left(\frac{L\omega}{c}\right)}{1 - r_{\rm F} r_{\rm E} e^{-2{\rm i}\frac{L\omega}{c}}} e^{-{\rm i}\frac{L\omega}{c}}, \tag{3.16}$$

[8]A simple Michelson interferometer is interpreted as a delay line with a bounce number $N_{\rm DL} = 2$.

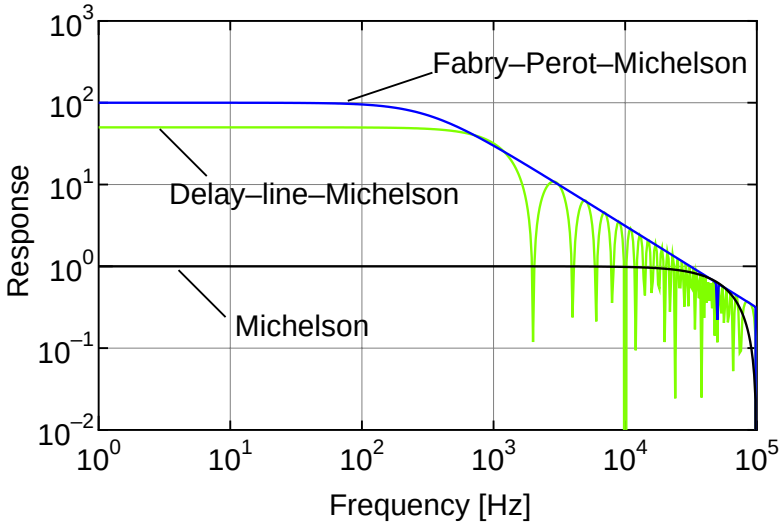

Figure 3.4: Calculated frequency responses of a delay-line Michelson interferometer and a Fabry-Perot-Michelson interferometer. The baseline length is 3 km and the response is optimized for gravitational waves with a frequency of 1 kHz. The frequency response of a simple Michelson interferometer with the same baseline length is drawn for comparison.

where

$$a_{\rm cav} = \frac{t_{\rm F}^2 r_{\rm E}}{1 - r_{\rm F} r_{\rm E}}, \tag{3.17}$$

$r_{\rm F}$ and $r_{\rm E}$ are the amplitude reflectivity of the front and end mirrors, $t_{\rm F}$ is the transmissivity of the front mirror, and L is the length of the Fabry-Perot cavity (Section 3.2).

The averaged bounce number in a Fabry-Perot cavity is written as

$$N_{\rm FP} = \frac{2\mathcal{F}}{\pi}, \tag{3.18}$$

where $\mathcal{F}$ is a finesse, which represents the sharpness of the resonance of the Fabry-Perot cavity.

Figure 3.4 shows the calculated frequency response of a delay-line-Michelson interferometer and a Fabry-Perot-Michelson interferometer. In both cases, the baseline length is 3 km and the response is optimized for a gravitational wave with a frequency of 1 kHz. For comparison, the frequency response of a Michelson

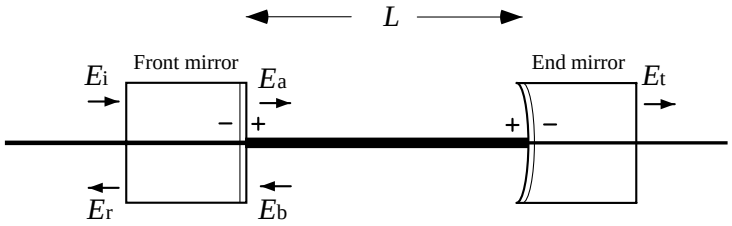

Figure 3.5: Fabry-Perot cavity. The cavity is comprised of two mirrors: a front mirror with a reflectivity of $R_{\rm F} = r_{\rm F}^2$ and an end mirror with a reflectivity of $R_{\rm E} = r_{\rm E}^2$. The sign change on reflection is defined in this figure.

interferometer with the same baseline length is drawn in Fig. 3.4. The response of the Fabry-Perot type interferometer shows a smoother response.

Though both types have advantages and disadvantages, the Fabry-Perot type is mainly researched and will be adopted in the large-scale interferometers under construction, LIGO and VIRGO. This is because a delay-line requires larger mirrors. In addition, scattered light noise is one of the main problems of a delay-line-type interferometer [53].

3.2 Fabry-Perot cavity

In the LIGO, VIRGO, and TAMA detectors, Fabry-Perot cavities are used to extend the effective baseline length. Fabry-Perot cavities are also used as a mode cleaner, a recycling cavity, and a reference cavity for frequency stabilization. In this Section, we describe the fundamentals and characteristics of a Fabry-Perot cavity.

3.2.1 Characteristics of a Fabry-Perot cavity

A Fabry-Perot cavity is comprised of two mirrors: a front mirror and an end mirror. Here, we consider the response of a Fabry-Perot cavity. Figure 3.5 shows the field amplitudes both inside and outside the Fabry-Perot cavity. These fields

satisfy the following equations.

$$
\begin{aligned}
E_{\mathrm{a}} &= t_{\mathrm{F}} E_{\mathrm{i}} + r_{\mathrm{F}} E_{\mathrm{b}} \\
E_{\mathrm{b}} &= r_{\mathrm{E}} e^{-\mathrm{i}\frac{2L\Omega_{\mathrm{l}}}{c}} E_{\mathrm{a}} \\
E_{\mathrm{r}} &= -r_{\mathrm{F}} E_{\mathrm{i}} + t_{\mathrm{F}} E_{\mathrm{b}} \\
E_{\mathrm{t}} &= t_{\mathrm{E}} e^{-\mathrm{i}\frac{L\Omega_{\mathrm{l}}}{c}} E_{\mathrm{a}},
\end{aligned}
$$

where Ω_{l} is angular frequency of the input laser beam, L is the length of the cavity. r and t represent the amplitude reflectivity and transmissivity, respectively. The indices '$_{\mathrm{F}}$' and '$_{\mathrm{E}}$' denote the front mirror and the end mirror, respectively.

From the above equations, the reflectivity and transmissivity of the Fabry-Perot cavity (r_{cav}, t_{cav}) and the amplitude gain of the cavity[9] (g_{cav}) are written as

$$
r_{\mathrm{cav}}(\Phi) = \frac{E_{\mathrm{r}}}{E_{\mathrm{i}}} = -r_{\mathrm{F}} + \frac{t_{\mathrm{F}}^2 r_{\mathrm{E}} e^{-\mathrm{i}\Phi}}{1 - r_{\mathrm{F}} r_{\mathrm{E}} e^{-\mathrm{i}\Phi}} \tag{3.19}
$$

$$
t_{\mathrm{cav}}(\Phi) = \frac{E_{\mathrm{t}}}{E_{\mathrm{i}}} = \frac{t_{\mathrm{F}} t_{\mathrm{E}} e^{-\mathrm{i}\Phi/2}}{1 - r_{\mathrm{F}} r_{\mathrm{E}} e^{-\mathrm{i}\Phi}} \tag{3.20}
$$

$$
g_{\mathrm{cav}}(\Phi) = \frac{E_{\mathrm{a}}}{E_{\mathrm{i}}} = \frac{t_{\mathrm{F}}}{1 - r_{\mathrm{F}} r_{\mathrm{E}} e^{-\mathrm{i}\Phi}}, \tag{3.21}
$$

where Φ is the round-trip phase in the cavity:

$$
\Phi \equiv \frac{2L\Omega_{\mathrm{l}}}{c}. \tag{3.22}
$$

When the laser beam transmitting through the front mirror interferes constructively with the circulating beam in the cavity, the cavity is said to be resonant with the incident beam. The resonance condition is written as

$$
\Phi = 0 + 2\pi n \quad (n : \text{natural number}). \tag{3.23}
$$

Under this resonance condition, t_{cav} and g_{cav} are maximized. The amplitude reflectivity on resonance results in

$$
r_{\mathrm{reso}} \equiv r_{\mathrm{cav}}(0) = -r_{\mathrm{F}} + \frac{t_{\mathrm{F}}^2 r_{\mathrm{E}}}{1 - r_{\mathrm{F}} r_{\mathrm{E}}}. \tag{3.24}
$$

[9]The amplitude gain of a cavity is defined as the ratio of the amplitude inside the cavity to that of the input beam.

3.2.2 Coupling of a cavity

The sign of the reflectivity of a Fabry-Perot cavity on resonance depends on the coupling of the cavity. The reflectivity of a Fabry-Perot cavity on resonance, Eq. (3.24), is comprised of two terms: the first term represents the beam directly reflected from the front mirror, and the second term represents the beam leaking from inside the cavity. The sign of these terms are opposite.

By neglecting the loss of the front mirror ($r_{\rm F}^2 + t_{\rm F}^2 = 1$), Eq. (3.24) is written as

$$r_{\rm reso} \simeq \frac{-r_{\rm F} + r_{\rm E}}{1 - r_{\rm F} r_{\rm E}}. \tag{3.25}$$

When $r_{\rm F} > r_{\rm E}$, the reflected beam is dominated by the directly-reflected beam with the front mirror. This cavity is called under-coupled. On the other hand, a cavity with $r_{\rm F} < r_{\rm E}$ is called over-coupled. In an over-coupled cavity, the reflected beam is dominated by the beam leaking from inside the cavity. The sign of the amplitude reflectivity of the cavity differs from each other in under- and over-coupled cavities. Arm cavities of the Michelson interferometer are usually set to be over-coupled so that the phase change signal generated inside the arm cavities should effectively leak to the detection port. In addition, $r_{\rm E}$ is usually set as high as possible to obtain a high recycling gain.

The reflectivity of a cavity on resonance is zero when $r_{\rm F} = r_{\rm E}$. This case is called optimal-coupled. An optimal-coupled cavity transmits all of the incident beam (if losses in the mirrors are neglected)[10]. This configuration is used in a mode cleaner.

The sign of the signal extracted from a power-recycled interferometer depends on the coupling of the recycling cavity. Moreover, the coupling of the recycling cavity plays an important role in the signal mixing and separation, which is described in detail in Chapter 4.

[10]This is easily shown in Eq. (3.26) by putting $r_{\rm F} = r_{\rm E}$ and $\Phi = 0$.

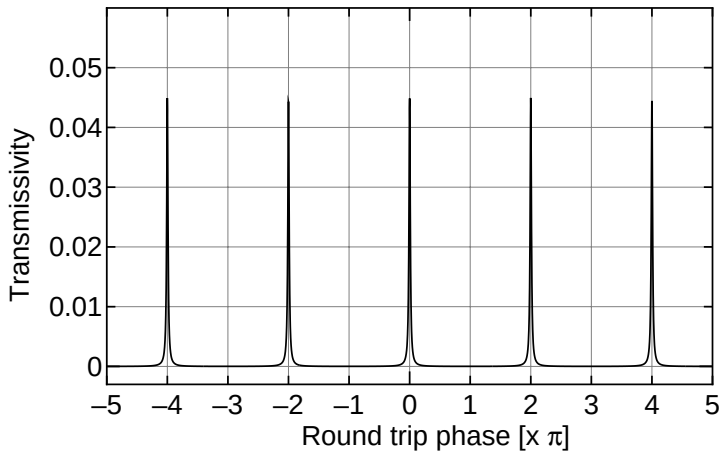

Figure 3.6: Transmissivity of a Fabry-Perot cavity as a function of Φ; the transmissivity is a periodic function of Φ.

3.2.3 FSR and finesse

From Eq. (3.20), the transmissivity of the Fabry-Perot cavity is written as

$$T_{\rm cav}(\Phi) = |t_{\rm cav}(\Phi)|^2 = \frac{(t_{\rm F}t_{\rm E})^2}{(1-r_{\rm F}r_{\rm E})^2}\frac{1}{1+F\sin^2(\Phi/2)}, \tag{3.26}$$

where a parameter F is defined by[11]

$$F \equiv \frac{4r_{\rm F}r_{\rm E}}{(1-r_{\rm F}r_{\rm E})^2}. \tag{3.27}$$

Figure 3.6 shows the transmissivity of the cavity[12] as a function of Φ; the transmissivity is a periodic function of Φ. Fixing the cavity length L, the transmissivity is a periodic function of $\Omega_{\rm l}$. The period is called as the free spectral

[11]The parameter F is related with the effective bounce number of the cavity $N_{\rm FP}$ in Eq. (3.48) by the equation

$$F = {N_{\rm FP}}^2,$$

and with the finesse $\mathcal{F}$ by

$$F = \left(\frac{2}{\pi}\mathcal{F}\right)^2.$$

[12]The parameters of the cavity used in this calculation are the same as those used in Fig. 3.4. The reflectivities are 92.5% and 99.9% for the front mirror and end mirror, respectively; the finesse is 80 and the cavity is over coupled.

range (FSR) of the cavity:

$$\nu_{\mathrm{FSR}} = \frac{\Omega_{\mathrm{FSR}}}{2\pi} = \frac{c}{2L}. \tag{3.28}$$

The FSR is determined only by the length of the cavity.

When the mirrors have high reflectivities ($r_{\mathrm{F}} \simeq 1$, $r_{\mathrm{E}} \simeq 1$), the transmittance has shape peaks at the resonance. The full width of the half maximum of the peak ν_{FWHM} is written as

$$\frac{1}{1 + F \sin^2 \frac{\pi L \nu_{\mathrm{FWHM}}}{c}} = \frac{1}{2}$$

With an approximation of $\nu_{\mathrm{FWHM}} \ll \nu_{\mathrm{FSR}}$, ν_{FWHM} is written as

$$\nu_{\mathrm{FWHM}} = \frac{1}{2\pi} \frac{1 - r_{\mathrm{F}} r_{\mathrm{E}}}{\sqrt{r_{\mathrm{F}} r_{\mathrm{E}}}} \frac{c}{L}. \tag{3.29}$$

The ratio of ν_{FSR} to ν_{FWHM} is called finesse, which represents the sharpness of the resonance of a Fabry-Perot cavity. The finesse is given by

$$\mathcal{F} = \frac{\nu_{\mathrm{FSR}}}{\nu_{\mathrm{FWHM}}} = \frac{\pi \sqrt{r_{\mathrm{F}} r_{\mathrm{E}}}}{1 - r_{\mathrm{F}} r_{\mathrm{E}}}, \tag{3.30}$$

which is determined only by the reflectivities of the mirrors.

3.2.4 Phase enhancement of a Fabry-Perot cavity

Here, we further investigate the reflectivity of a Fabry-Perot cavity. Figure 3.7 shows the absolute value and the phase of the reflectivity of a Fabry-Perot cavity $r_{\mathrm{cav}}(\Phi)$. The reflectivity of a simple mirror is shown together for comparison, which is described by setting $r_{\mathrm{F}} = 0$ and $t_{\mathrm{F}} = 1$ in $r_{\mathrm{cav}}(\Phi)$. From this figure, we can see that the phase of the reflected beam changes rapidly around the resonance point.

In order to investigate the reflectivity change for a small round-trip phase change, we differentiate $r_{\mathrm{cav}}(\Phi)$ by Φ:

$$r'_{\mathrm{cav}}(\Phi) = \frac{-i t_{\mathrm{F}}^2 r_{\mathrm{E}} e^{-\mathrm{i}\Phi}}{\left(1 - r_{\mathrm{F}} r_{\mathrm{E}} e^{-\mathrm{i}\Phi}\right)^2}. \tag{3.31}$$

From Eq. (3.31), we can see that $|r'_{\mathrm{cav}}(\Phi)|$ is maximized at the resonance; the phase of the reflected beam from a Fabry-Perot cavity is most sensitive to the

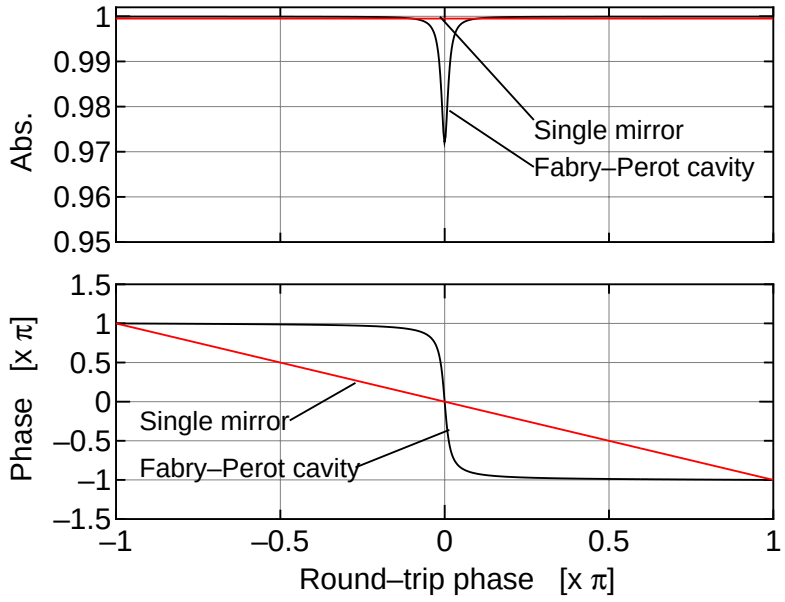

Figure 3.7: Absolute value and phase of the reflectivity of a Fabry-Perot cavity as a function of phase Φ. The reflectivity of a simple mirror is also shown for comparison. The phase of the beam reflected by a Fabry-Perot cavity changes rapidly around the resonance point.

round-trip phase change at the resonance. The reflectivity around the resonance is written as

$$r_{\rm reso}(\delta\Phi) = r_{\rm reso} + r'_{\rm reso}\delta\Phi \tag{3.32}$$

for a small change of Φ. Where $r_{\rm reso}$ and $r'_{\rm reso}$ are the reflectivity and its derivative on resonance:

$$r'_{\rm reso} = \frac{-it_{\rm F}^2 r_{\rm E}}{(1 - r_{\rm F} r_{\rm E})^2}. \tag{3.33}$$

The absolute value of the reflectivity does not change with a small $\delta\Phi$. On the other hand, the phase of the reflectivity changes largely by $\delta\Phi$. The phase of the reflected beam is more sensitive to the round-trip phase change with a Fabry-Perot cavity on resonance than with a simple mirror. This enhancement of the phase sensitivity is interpreted as the extension of the effective baseline length. Here, we define $N_{\rm cav}$ by

$$N_{\rm cav} \equiv \left| \frac{r'_{\rm reso}}{r_{\rm reso}} \right|. \tag{3.34}$$

$N_{\rm cav}$ is called the effective bounce number of the cavity because the phase change of the beam reflected by a Fabry-Perot cavity is enhanced by a factor of $N_{\rm cav}$, comparing that reflected by a simple mirror[13].

3.2.5 Response to gravitational waves

As described before, the response of a Fabry-Perot cavity to gravitational waves has a frequency dependence. We discuss the frequency response of a Fabry-Perot cavity here[14].

The time taken for a photon to make n-times' round-trips between two mirrors is written in the same manner as Eq. (3.6):

$$\Delta t_n \simeq \frac{2L}{c}n + \frac{1}{2}\int_{t-\frac{2L}{c}n}^{t} h_+(t')dt', \tag{3.35}$$

for the cavity with length L along x-direction. This equation is rewritten with a Fourier transformation Eq. (3.11) as

$$\Delta t_n \simeq \frac{2L}{c}n + \frac{1}{2}\int_{-\infty}^{\infty} h_+(\omega)\frac{1-e^{-2{\rm i}\frac{L\omega}{c}n}}{{\rm i}\omega}e^{{\rm i}\omega t}d\omega. \tag{3.36}$$

Then, the beam reflected by the Fabry-Perot cavity is written as superposition of the multi-reflected beams:

$$E_{\rm r} = E_{\rm i}\left\{-r_{\rm F} + t_{\rm F}^2 r_{\rm E}\sum_{n=1}^{\infty}(r_{\rm F}r_{\rm E})^{n-1}e^{-{\rm i}\Omega_{\rm l}\Delta t_n}\right\}. \tag{3.37}$$

Substituting Δt_n in Eq. (3.36), and using the approximation $|h_+| \ll 1$, we obtain

$$\begin{aligned} r_{\rm cav}(\Phi,\omega) = &-r_{\rm F} + \frac{t_{\rm F}^2 r_{\rm E}e^{-{\rm i}\Phi}}{1-r_{\rm F}r_{\rm E}e^{-{\rm i}\Phi}} \\ &-\frac{t_{\rm F}^2 r_{\rm E}e^{-{\rm i}\Phi}}{1-r_{\rm F}r_{\rm E}e^{-{\rm i}\Phi}}\int_{-\infty}^{\infty}\frac{\Omega_{\rm l}}{2\omega}h_+(\omega)\frac{1-e^{-2{\rm i}\gamma}}{1-r_{\rm E}r_{\rm F}e^{-{\rm i}\Phi}e^{-2{\rm i}\gamma}}e^{i\omega t}d\omega, \end{aligned} \tag{3.38}$$

where

$$\gamma \equiv \frac{L\omega}{c}. \tag{3.39}$$

[13]The reflectivity can be written as $r = ae^{-{\rm i}N\Phi}$, where a is a constant number and N is a phase enhancement factor. From this expression, we obtain the relation $N = \left|\frac{r'}{r}\right|$.

[14]Here, we consider the same gravitational waves as before: +-polarized gravitational waves propagating along the z-direction.

In the case that the incident beam is resonant with the cavity ($\Phi = 0$), the reflectivity is written as

$$r_{\rm reso}(\omega) = r_{\rm reso} - {\rm i}\int_{-\infty}^{\infty} H_{\rm FP}(\omega) h_+(\omega) e^{{\rm i}\omega t} d\omega, \tag{3.40}$$

where $H_{\rm FP}(\omega)$ is the frequency response function of a Fabry-Perot cavity to gravitational waves[15]

$$H_{\rm FP}(\omega) = \frac{a_{\rm cav}\Omega_{\rm l}}{\omega} \frac{\sin\gamma}{1 - r_{\rm F} r_{\rm E} e^{-2{\rm i}\gamma}} e^{-{\rm i}\gamma}, \tag{3.41}$$

$$a_{\rm cav} = \frac{t_{\rm F}^2 r_{\rm E}}{1 - r_{\rm F} r_{\rm E}}. \tag{3.42}$$

Since the gravitational waves cause phase changes of opposite sign in the y-direction, the frequency response function is doubled for the Fabry-Perot-Michelson interferometer, written as[16]

$$H_{\rm FPMI} = 2H_{\rm FP}(\omega). \tag{3.43}$$

3.2.6 Storage time

With a good approximation that the changes in gravitational waves are small enough within the round-trip time in the cavity ($\gamma = \frac{\omega L}{c} \ll 1$), the frequency response is written as

$$|H_{\rm FP}(\omega)| = \frac{a_{\rm cav}\Omega_{\rm l} L}{c(1 - r_{\rm F} r_{\rm E})} \frac{1}{\sqrt{1 + (\tau\omega)^2}}, \tag{3.44}$$

where τ is an average storage time of a photon in the cavity

$$\tau = \frac{\sqrt{F}L}{c} = \frac{2L}{c} \frac{\sqrt{r_{\rm F} r_{\rm E}}}{(1 - r_{\rm F} r_{\rm E})}. \tag{3.45}$$

[15]The second term of Eq. (3.40) does not represent the phase change on the reflection, but the sideband produced by the phase modulation by gravitational waves.

[16]When the arm lengths are equal in Michelson and Fabry-Perot-Michelson interferometers, the ratio of the response functions reduces to the phase-enhancement factor of the Fabry-Perot cavity in the limit $\omega \to 0$:

$$\lim_{\omega\to 0} \frac{H_{\rm FPMI}}{H_{\rm MI}} = \lim_{\omega\to 0} \frac{a_{\rm cav}}{1 - r_{\rm F} r_{\rm E} e^{-2{\rm i}\gamma}} = |r'_{\rm reso}|.$$

Equation (3.44) shows that the cavity is a low-pass filter with a cutoff frequency of

$$\nu_{\rm c} = \frac{\omega_{\rm c}}{2\pi} = \frac{1}{2\pi\tau}. \tag{3.46}$$

The storage time τ in Eq. (3.45) is written using the finesse expressed by Eq. (3.30):

$$\tau = \frac{2L}{\pi c}\mathcal{F}. \tag{3.47}$$

In addition, since τ can be considered as the average storage time in a cavity, the effective bounce number $N_{\rm FP}$ is defined by the equation

$$\tau = N_{\rm FP}\frac{L}{c}.$$

From this equation, $N_{\rm FP}$ is expressed by the finesse:

$$N_{\rm FP} = \frac{c\tau}{L} = \frac{2\mathcal{F}}{\pi}. \tag{3.48}$$

3.2.7 Response to mirror displacement

In practice, the phase of the beam reflected from a Fabry-Perot cavity is also changed by the motion of the mirrors caused by noise such as seismic noise and thermal noise. In this part, we show the response of a cavity to the mirror motion.

The time taken for a photon to make n-times' round-trips in the cavity is written as

$$\Delta t_n \simeq \frac{2L}{c}n + \frac{2}{c}\sum_{m=1}^{n}\delta L\big(t-\frac{1}{c}(2m-1)L\big) \tag{3.49}$$

with the approximation of $\delta L(t) \ll L$. With a Fourier transformation expressed by

$$\delta L(t) = \int_{-\infty}^{\infty}\delta L(\omega)e^{i\omega t}d\omega,$$

the equation is rewritten as

$$\Delta t_n \simeq \frac{2L}{c}n + \frac{2}{c}\int_{-\infty}^{\infty}\delta L(\omega)\frac{1-e^{-2{\rm i}\gamma n}}{e^{{\rm i}\gamma}-e^{-{\rm i}\gamma}}e^{i\omega t}d\omega. \tag{3.50}$$

Substrating this expression for Δt_n to

$$r_{\rm cav} = -r_{\rm F} + t_{\rm F}^2 r_{\rm E} \sum_{n=1}^{\infty} (r_{\rm F} r_{\rm E})^{n-1} e^{-{\rm i}\Omega_{\rm l}\Delta t_n}$$

and using an approximation $\delta L(\omega) \ll 1$, we obtain

$$\begin{aligned} r_{\rm cav}(\Phi,\omega) &= -r_{\rm F} + t_{\rm F}^2 r_{\rm E} \sum_{n=1}^{\infty} (r_{\rm F} r_{\rm E})^{n-1} e^{-2{\rm i}\frac{L\Omega_{\rm l}}{c}n} \left\{ 1 - {\rm i}\frac{2\Omega_{\rm l}}{c} \int_{-\infty}^{\infty} \delta L(\omega) \frac{1 - e^{-2{\rm i}\gamma n}}{e^{{\rm i}\gamma} - e^{-{\rm i}\gamma}} e^{{\rm i}\omega t} d\omega \right\} \\ &= -r_{\rm F} + \frac{t_{\rm F}^2 r_{\rm E} e^{-{\rm i}\Phi}}{1 - r_{\rm F} r_{\rm E} e^{-{\rm i}\Phi}} \\ &\quad -{\rm i}\frac{t_{\rm F}^2 r_{\rm E} e^{-{\rm i}\Phi}}{1 - r_{\rm F} r_{\rm E} e^{-{\rm i}\Phi}} \int_{-\infty}^{\infty} \frac{2\Omega_{\rm l}}{c} \delta L(\omega) \frac{e^{-{\rm i}\gamma}}{1 - r_{\rm F} r_{\rm E} e^{-{\rm i}\Phi} e^{-2{\rm i}\gamma}} e^{{\rm i}\omega t} d\omega \end{aligned} \tag{3.51}$$

When the input beam is resonant with the cavity, the reflectivity is written as

$$r_{\rm reso}(\omega) = r_{\rm reso} - {\rm i} \int_{-\infty}^{\infty} H_{\rm FP}^{\rm (L)}(\omega) \delta L(\omega) e^{{\rm i}\omega t} d\omega, \tag{3.52}$$

where $H_{\rm FP}^{\rm (L)}(\omega)$ is the response of a Fabry-Perot cavity to the change in the cavity length:

$$H_{\rm FP}^{\rm (L)}(\omega) = \frac{2 a_{\rm cav} \Omega_{\rm l}}{c} \frac{e^{-{\rm i}\gamma}}{1 - r_{\rm F} r_{\rm E} e^{-2{\rm i}\gamma}}. \tag{3.53}$$

$H_{\rm FP}^{\rm (L)}(\omega)$ is related with the response to gravitational waves $H_{\rm FP}(\omega)$ by

$$H_{\rm FP}^{\rm (L)}(\omega) = \frac{2\omega}{c \sin\gamma} H_{\rm FP}(\omega) \simeq \frac{2}{L} H_{\rm FP}(\omega). \tag{3.54}$$

This relation means that the response of the cavity to a cavity length change δL is equal to the response to gravitational waves with an amplitude $2\delta L/L$. In other words, the response of a Fabry-Perot-Michelson interferometer to the differential length change in two cavities δL_- is equal to the response to gravitational waves with an amplitude

$$h_+ = \frac{\delta L_-}{L}. \tag{3.55}$$

3.2.8 Response to frequency fluctuation

Fabry-Perot cavity is also sensitive to a frequency fluctuation of the input laser beam. Here, we consider the response of a Fabry-Perot cavity to a laser frequency noise.

A frequency noise $\delta\nu(t)$ has a following relation with a phase noise of the laser source $\delta\phi(t)$:

$$\delta\nu(t) = \frac{1}{2\pi}\frac{\partial\phi(t)}{\partial t}. \tag{3.56}$$

In a case that the phase noise is small enough, $\delta\phi(t) \ll 1$, the incident laser beam is written as

$$E_{\rm in} = E_0 e^{{\rm i}\{\Omega_{\rm l}t+\delta\phi(t)\}} = E_0 e^{{\rm i}\Omega_{\rm l}t}\{1+{\rm i}\delta\phi(t)\}. \tag{3.57}$$

This equation is rewritten as

$$E_{\rm in} = E_0 e^{{\rm i}\Omega_{\rm l}t} + {\rm i}E_0\int_{-\infty}^{\infty}\delta\phi(\omega)e^{{\rm i}(\Omega_{\rm l}+\omega)t}d\omega, \tag{3.58}$$

using a Fourier transformation

$$\delta\phi(t) = \int_{-\infty}^{\infty}\delta\phi(\omega)e^{{\rm i}\omega t}d\omega.$$

Then the reflected beam by a Fabry-Perot cavity, $E_{\rm r}$, is written as

$$E_{\rm r} = E_0 r_{\rm cav}(\Phi)e^{i\Omega_{\rm l}t} + iE_0\int_{-\infty}^{\infty}\delta\phi(\omega)r_{\rm cav}(\Phi_\omega)e^{i(\Omega_{\rm l}+\omega)t}d\omega, \tag{3.59}$$

where

$$\Phi_\omega = \frac{2L(\Omega_{\rm l}+\omega)}{c} = \Phi + 2\gamma.$$

From Eq. (3.59), we obtain with an approximation $\delta\phi(t) \ll 1$,

$$\begin{aligned} E_{\rm r} &= E_0 r_{\rm cav}(\Phi)e^{{\rm i}\{\Omega t+\delta\phi(t)\}} + {\rm i}E_0\int_{-\infty}^{\infty}\{r_{\rm cav}(\Phi_\omega)-r_{\rm cav}(\Phi)\}\,\delta\phi(\omega)e^{{\rm i}(\Omega_{\rm l}+\omega)t}d\omega \\ &\simeq E_{\rm in}r_{\rm cav}(\Phi) \\ &\quad + E_{\rm in}\frac{t_{\rm F}^2 r_{\rm E}e^{-{\rm i}\Phi}}{1-r_{\rm F}r_{\rm E}e^{-{\rm i}\Phi}}\int_{-\infty}^{\infty}\frac{2\sin\gamma}{1-r_{\rm F}r_{\rm E}e^{-{\rm i}(\Phi+2\gamma)}}e^{-{\rm i}\gamma}\delta\phi(\omega)e^{{\rm i}\omega t}d\omega. \end{aligned} \tag{3.60}$$

Under a resonant condition of the cavity[17],

$$r_{\rm reso}(\omega) = r_{\rm reso} - {\rm i}\int_{-\infty}^{\infty}H_{\rm FP}^{\rm (F)}(\omega)\delta\nu(\omega)e^{{\rm i}\omega t}d\omega, \tag{3.61}$$

[17]From Eq. (3.56), we have a relation

$$\delta\phi(\omega) = \frac{2\pi\delta\nu(\omega)}{i\omega}.$$

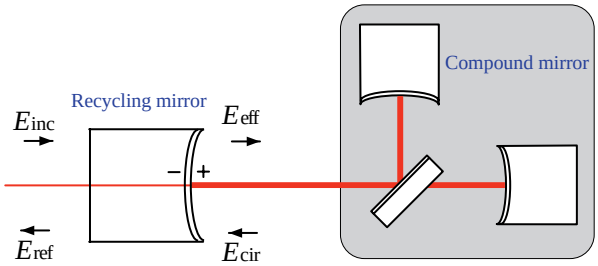

Figure 3.8: Recycling cavity formed by a recycling mirror and a compound mirror. Fields around are defined at the recycling mirror.

where $H_{\mathrm{FP}}^{(\mathrm{F})}(\omega)$ is a frequency response function of a Fabry-Perot cavity to a frequency fluctuation:

$$H_{\mathrm{FP}}^{(\mathrm{F})}(\omega) = \frac{4\pi a_{\mathrm{cav}}}{\omega} \frac{\sin\gamma}{1 - r_{\mathrm{F}} r_{\mathrm{E}} e^{-2\mathrm{i}\gamma}} e^{-\mathrm{i}\gamma}. \tag{3.62}$$

$H_{\mathrm{FP}}^{(\mathrm{F})}(\omega)$ has a following relation with $H_{\mathrm{FP}}^{(\mathrm{L})}(\omega)$ when γ is small enough:

$$H_{\mathrm{FP}}^{(\mathrm{L})}(\omega) \simeq \frac{\nu_{\mathrm{l}}}{L} H_{\mathrm{FP}}^{(\mathrm{F})}(\omega), \tag{3.63}$$

where ν_{l} is a frequency of the laser source ($\nu_{\mathrm{l}} = \Omega_{\mathrm{l}}/2\pi$). From Eq. (3.63) a frequency noise $\delta\nu_{\mathrm{l}}$ cause a same noise as

$$\delta L = \frac{\delta\nu_{\mathrm{l}}}{\nu_{\mathrm{l}}} L. \tag{3.64}$$

3.3 Power recycling

3.3.1 Principle of power recycling

Shot noise is one of fundamental noises which limit the sensitivity of an interferometer. Shot noise is a photon counting error, which is proportional to the square-root of the laser power incident in the interferometer. Since the gravitational wave signal is proportional to the incident power, the shot-noise level of an interferometer is improved with a high laser power.

Besides increasing the laser-source power, the shot-noise level is improved by a technique called power recycling [15]. In order to realize the best shot-noise level, an interferometric gravitational wave detector is usually operated under a

dark fringe condition; the reflected beams by the arm mirrors (or cavities) are set to interfere destructively at the detection port. In this case, most of the injected laser power is reflected back toward the laser source if the losses of the interferometer is low enough. This back-reflected beam is reused by reflecting back into the interferometer with a partial mirror inserted between the laser source and the interferometer, which results in the increase of power in the interferometer. This scheme is called power recycling, and the inserted mirror is called a power recycling mirror.

In another point of view, power recycling is considered to be a formation of an additional cavity, called a recycling cavity (Fig. 3.8). A Michelson interferometer operated at the dark fringe is considered to be a high-reflective compound mirror. The recycling mirror forms a recycling cavity with this compound mirror; the power in the cavity is enhanced when the cavity is resonant with the input laser beam.

3.3.2 Recycling cavity

Considering the recycling cavity as a Fabry-Perot cavity, the amplitude reflectivity and gain is written in the same way as Section 3.2. The compound mirror forms a recycling cavity together with the recycling mirror (Fig. 3.8). The fields around the recycling cavity have the relations

$$\begin{aligned} E_{\mathrm{eff}} &= t_{\mathrm{R}} E_{\mathrm{inc}} + r_{\mathrm{R}} E_{\mathrm{cir}} \\ E_{\mathrm{cir}} &= r_{\mathrm{com}} E_{\mathrm{eff}} \\ E_{\mathrm{ref}} &= -r_{\mathrm{R}} E_{\mathrm{inc}} + t_{\mathrm{R}} E_{\mathrm{cir}}, \end{aligned}$$

where index '$_{\mathrm{R}}$' denotes the recycling mirror. r_{com} is an complex reflectivity of the compound mirror; the absolute value and the phase represent the amplitude reflectivity and phase change on reflection, respectively. From above equations, we obtain the expressions for the amplitude gain of the recycling cavity g and the reflectivity of the recycling cavity r_{rec}:

$$g = \frac{E_{\mathrm{eff}}}{E_{\mathrm{inc}}} = \frac{t_{\mathrm{R}}}{1 - r_{\mathrm{R}} r_{\mathrm{com}}} \tag{3.65}$$

$$r_{\mathrm{rec}} = \frac{E_{\mathrm{ref}}}{E_{\mathrm{inc}}} = -r_{\mathrm{R}} + \frac{t_{\mathrm{R}}^2 r_{\mathrm{com}}}{1 - r_{\mathrm{R}} r_{\mathrm{com}}}. \tag{3.66}$$

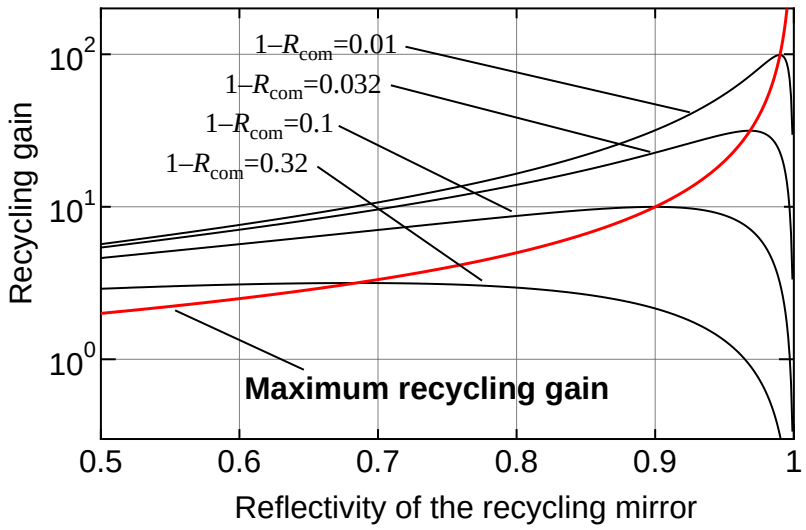

Figure 3.9: Power recycling gain as a function of the reflectivity of the recycling mirror for given reflectivities of the compound mirror. The power recycling gain is maximized when the reflectivity of the recycling mirror is equal to that of the compound mirror.

The incident beam is resonate with the recycling cavity when $r_{\rm com}$ is a real and positive number.

3.3.3 Power recycling gain

The ratio of the laser power on the beamsplitter with and without the recycling mirror, G, is called a power recycling gain or a power recycling factor:

$$G = g^2 = \frac{t_{\rm R}^2}{(1 - r_{\rm R} r_{\rm com})^2}. \tag{3.67}$$

When $G > 1$, the effective power of the laser source, i.e., the laser power incident on the interferometer, increases to $GP_{\rm I}$, and the shot-noise level is improved by $\sqrt{G}$. Figure 3.9 shows a power recycling gain as a function of the reflectivity of the recycling mirror ($R_{\rm R}$) for given reflectivities of a compound mirror ($R_{\rm com} = |r_{\rm com}|^2$). The power recycling gain is maximized when the reflectivity of the

recycling mirror is equal to that of the compound mirror[18]:

$$R_{\mathrm{R}} = R_{\mathrm{com}}. \tag{3.68}$$

Under this condition, the recycling cavity is considered to be a Fabry-Perot cavity comprised of mirrors with a same reflectivity; all of the input power is transmits through or lost in the recycling cavity. Equation (3.67) is written with the resonant condition and Eq. (3.68) as

$$G_{\mathrm{max}} = \frac{1}{1 - R_{\mathrm{com}}}. \tag{3.69}$$

$1 - R_{\mathrm{com}}$ is a total loss in the compound mirror: scattering, absorption, finite reflectivity of the end mirrors (or arm cavities), imperfect interference on the beamsplitter, and wave-front distortions[19]. Equation (3.69) shows that the maxim power recycling gain is inverse proportional to the total loss of the compound mirror.

3.4 Noise sources for an interferometer

The sensitivity of an interferometric gravitational detector can be easily degraded by a lot of noise sources. The fundamental noises for a ground-based interferometer are shot noise, thermal noise, and seismic noise. In this Section, we describe these fundamental noises and other main noise sources.

3.4.1 Optical readout noise

The sensitivity of an optical measurement system like an interferometric gravitational wave detector is limited by the optical readout noise: the shot noise and the radiation pressure noise [54].

Shot noise

Shot noise is one of fundamental noises which limit the sensitivity of an interferometer. Michelson interferometer converts differential phase changes in its arms

[18] We neglect the loss in the recycling mirror here.

[19] The wave front of a laser beam is distorted on reflection on and transmission through optics of the interferometer. This distortions are considered to be a scattering from the TEM_{00} mode to higher modes.

to power change in the interference fringe. A photo detector counts the number of photons in this fringe in a certain measurement time, and produces photo currents proportional to the incident power on it. In this process, the counted number of photons has some probability distribution[20], which results in a photon counting error called shot noise.

When a photo diode produces a DC photocurrent of $i_{\rm dc}$ [A], the shot noise current is written as a white noise

$$i_{\rm shot} = \sqrt{2ei_{\rm dc}} \quad [{\rm A}/\sqrt{\rm Hz}], \tag{3.70}$$

where e is an elementary charge[21]. The shot noise is proportional to the square-root of the photo current.

On the other hand, the signal corresponding to the phase change is proportional to the input laser power. As a result, the phase noise level due to the shot noise in a Michelson interferometer is expressed as

$$\delta\phi_{-\rm shot} = \sqrt{\frac{2e}{i_{\rm l}}} \quad [{\rm rad}/\sqrt{\rm Hz}], \tag{3.71}$$

where $i_{\rm l}$ is a photocurrent[22] caused by a incident laser power of $P_{\rm l}$. This noise level is called shot-noise limit; this noise level does not improved by a selection of the operational point nor modulation scheme. In practice, shot-noise level of an interferometer is worse than this limit because of a finite contrast and so on[23]. The DC photo current produced by the input laser power of $P_{\rm l}$ is written as

$$i_{\rm l} = \frac{e\eta}{\hbar\Omega_{\rm l}} P_{\rm l} \quad [{\rm A}], \tag{3.72}$$

[20]The counted number of photons obey a Poisson distribution. $p(N) = \frac{\bar{N}^N e^{-\bar{N}}}{N!}$, where $\bar{N}$ is a mean photon number in a counting interval. When the photon number is large enough ($\bar{N} \gg 1$), this distribution is approximated by a Gaussian distribution with a standard deviation of $\sqrt{\bar{N}}$.

[21]Elementary charge: $e = 1.60217733 \times 10^{-19}$ [C]

[22]Note that $i_{\rm l}$ is different from $i_{\rm DC}$ in Eq. (3.70).

[23]Note that sensitivity of an interferometer limited by the shot noise is improved with a Fabry-Perot cavity or optical delay-line in arms of the Michelson interferometer in a lower frequency range than the cutoff frequency. This is because these optical devices enhance the phase change caused by gravitational waves in the arms. Since the Michelson interferometer has a same phase sensitivity with or without these devices, the shot-noise limited sensitivity is determined by the input laser power when the frequency response is optimized.

where η is quantum efficiency of the photo diode, and $\hbar$ is a reduced Planck constant[24]. Substrating $i_{\rm l}$ into Eq. (3.71), we obtain[25]

$$\delta h_{\rm shot} = \frac{1}{l}\sqrt{\frac{\hbar c\lambda_{\rm l}}{4\pi\eta P_{\rm l}}} \quad [1/\sqrt{\rm Hz}]. \tag{3.73}$$

This equation shows that the shot-noise limit is inverse-proportional to the square-root of the input laser power $P_{\rm l}$. Thus, a high-power laser source is necessary to reduce the shot noise level.

Radiation pressure noise

Besides the shot noise, the quantum nature of light cause another noise in an interferometer, the radiation pressure noise. A mirror position is perturbed by the radiation pressure of the laser beam reflected back with the mirror. Thus, the fluctuation of the photon number causes a mirror displacement noise; this noise is called a radiation pressure noise. The radiation pressure noise is described by [55]

$$\delta h_{\rm radiation} = \frac{1}{Mf^2 l}\sqrt{\frac{\hbar P_{\rm l}}{\pi^3 c\lambda_{\rm l}}} \quad [1/\sqrt{\rm Hz}], \tag{3.74}$$

where M is the mass of the mirror.

Though shot noise level is reduced with a higher incident laser power, the radiation pressure noise increases proportional to the square-root of the incident power. In addition, while the shot noise is a white noise, the radiation pressure noise is proportional to f^{-2}. Thus, the incident laser power in optimized for a certain frequency to minimize the quadrature sum of these two noises, called optical readout noise. The optimized power for the frequency of $f_{\rm obs}$ is

$$P_{\rm l,opt} = \frac{\pi c\lambda_{\rm l} f_{\rm obs}^2 M}{2}, \tag{3.75}$$

and the optimized sensitivity is

$$\delta h_{\rm QL} = \frac{1}{\pi f_{\rm obs} l}\sqrt{\frac{\hbar}{M}} \quad [1/\sqrt{\rm Hz}], \tag{3.76}$$

[24]Reduced Planck constant: $\hbar = 1.055 \times 10^{-34}$ [J · s]

[25]Here, the phase noise is converted to the strain noise using the DC response of a Michelson interferometer, Eq. (3.10).

which is the quantum limit of optical readout system. The optimal laser power for $M = 10$ kg, $f_{\rm obs} = 100$ Hz, and $\lambda = 1064$ nm is 50 MW. At present, since the output power of the stable laser source is about a few ten Watt at most, the optical readout noise is dominated by the shot noise; the noise level is reduced with increase of incident laser power.

3.4.2 Thermal noise

The thermal noise is another fundamental noise source for an interferometric gravitational wave detector. Since the instrument forming an interferometer is soaked in a thermal bath, it is excited by the thermal motion. In an interferometer, the displacement noise is caused by the internal motion of the mirror and the pendulum motion of the suspension system.

Displacement noise due to dissipation

The equation of motion with a dissipation by internal friction in a material (structure damping model) is written in the frequency domain as [56]

$$m[-\omega^2 + \omega_0^2\{1 + {\rm i}\phi_{\rm k}(\omega)\}]x(\omega) = f_{\rm T}(\omega),$$

where $\phi_{\rm k}(\omega)$ is a complex elastic constant, $f_{\rm T}$ is a fluctuating force due to dissipation, and ω_0 and m is the resonant frequency and effective mass of this system, respectively. The Q-value at the resonance is written by the complex elastic constant as $Q = 1/\phi_{\rm k}(\omega_0)$. From the above equation, the power spectrum of the displacement is written as

$$\delta x = \left[\frac{4k_{\rm B}T\omega_0^2}{mQ\omega}\frac{1}{|-\omega^2 + \omega_0^2(1 + {\rm i}/Q)|^2}\right]^{1/2} \quad [{\rm m}/\sqrt{\rm Hz}], \tag{3.77}$$

where $k_{\rm B}$ and T are a Boltzmann constant[26] and temperature of the system. The complex elastic constant is believed to have little frequency dependence from results of several measurement [57, 58].

In order to reduce the thermal noise level, we must increase the Q-value by the investigation on the low-loss materials and suspension mechanics. Another way to improve the thermal noise level is to reduce the temperature by cooling down the system [59].

[26]Boltzmann constant : $k_{\rm B} = 1.381 \times 10^{-23}$ [J/K].

Thermal noise of pendulum

The resonant frequency of the pendulum mode of the suspension system ($\omega_{\rm pen}/2\pi \sim 1$ Hz) is usually much lower than the observation band (about few hundred Hertz). In this case ($\omega \gg \omega_{\rm pen}$), the thermal noise level of the suspension system is written

$$\delta x(\omega) \simeq \sqrt{\frac{4k_{\rm B}T\omega_{\rm pen}^2}{MQ\omega^5}} \quad [{\rm m}/\sqrt{\rm Hz}], \tag{3.78}$$

which is proportional to $f^{-\frac{5}{2}}$.

The violin modes of the suspension wire are also excited by the thermal disturbance [60]. The resonant frequencies are described as

$$\omega_n \simeq n\pi\omega_{\rm pen}\sqrt{\frac{M}{m_{\rm w}}}, \tag{3.79}$$

where $m_{\rm w}$ is the mass of the wire, and n is a natural number. The effective mass of each mode (m_n) is written as

$$m_n \simeq \frac{M}{2}\left(1 + n^2\pi^2\frac{M}{m_{\rm w}}\right). \tag{3.80}$$

The thermal noise level due to the wire violin modes are described by the quadrature sum of the contributions of these modes.

Thermal noise of mirror

The resonant frequency of the internal mode of the test mass ($\omega_{\rm int} \sim 10$ kHz) is usually much higher than the observation band. In this case ($\omega \ll \omega_{\rm int}$), the thermal noise level of the suspension system is written

$$\delta x(\omega) \simeq \sqrt{\frac{4k_{\rm B}T}{m_{\rm eff}Q\omega_{\rm int}^2\omega}} \quad [{\rm m}/\sqrt{\rm Hz}], \tag{3.81}$$

where $m_{\rm eff}$ is the effective mass of the internal mode; the effective mass of the lowest mode is half of the mirror mass. The thermal noise level of the internal mode of the test mass must be estimated considering the contributions from all of the internal modes. The thermal noise level of the mass internal motion is proportional to $f^{-\frac{1}{2}}$.

3.4.3 Seismic noise

Ground motion, called seismic noise, is one of the crucial noise sources for a ground-based interferometer; the ground motion excites the motions of optical components of an interferometer, resulting in a displacement noise. In addition, large ground motion in low frequency region can make the interferometer unstable.

Seismic motion and suspension system

Though the ground motion amplitude depends on the interferometer location (at city area or country area, on or under the ground, etc), the power spectrum density is roughly proportional to f^{-2}:

$$\delta x_{\rm seis}(f) \sim 10^{-7} \times \left(\frac{1}{f}\right)^2 \quad \left[\mathrm{m}/\sqrt{\mathrm{Hz}}\right], \tag{3.82}$$

in a frequency region over 0.1 Hz. The factor 10^{-7} is valid for a city area, as Tokyo city. In a quiet place like abandoned mine, the factor falls to $10^{-8} \sim 10^{-9}$.

In a ground-based interferometers, the mirrors of an interferometer are suspended as pendulums so as to behave as free test masses. This suspension system has another role to isolate the mirror from seismic noise. A vibration isolation ratio of a single pendulum, the ratio of motions of the mass to that at the suspension point called a vibration isolation ratio[27], is written as

$$H_{\rm pen}(f) = \frac{1 + \frac{\mathrm{i}}{Q}\frac{f}{f_{\rm pen}}}{1 + \frac{\mathrm{i}}{Q}\frac{f}{f_{\rm pen}} - \left(\frac{f}{f_{\rm pen}}\right)^2}, \tag{3.83}$$

where $f_{\rm pen}$ and Q are the resonant frequency and Q-value of the pendulum. Thus, the motion of the mirror is isolated from the seismic motion by $(f_{\rm pen}/f)^2$ at a higher region than the resonance frequency ($f \gg f_{\rm pen}$) when Q-value is high enough ($Q \gg f/f_{\rm pen}$).

[27] A vibration isolation ratio is sometimes defined by $1/H_{\rm pen}$.

Vibration isolation system

In practice, the seismic isolation ratio of a simple single pendulum is not sufficient for the detection of gravitational waves[28]. Since the resonant frequency, $f_{\rm pen}$, is around 1 Hz in a single pendulum with a reasonable length (a few tens of cm), the vibration isolation ratio is about 10^{-4} at 100 Hz. In a typical design of an interferometer, the vibration isolation ratio is required over $10^{-8} \sim 10^{-9}$ at 100 Hz. In order to realize such a high vibration isolation ratio, several design of the isolation system is proposed: a multi-stage pendulum, a low-resonant-frequency pendulum, combination of other isolation systems like a stack system.

In a n-stage pendulum, the vibration isolation ratio is expressed roughly[29] as $H_{n-\rm pen} = (f_{\rm pen}/f)^{2n}$. On the other hand, the vibration isolation ratio is improved by a low-resonant-frequency pendulum as implied in Eq. (3.83); it is proportional to $f_{\rm pen}^2$. A low-resonant-frequency pendulum is realized with a reasonable size by X-pendulum [61, 62], and active controlled pendulum. The seismic vibration is also isolated with a stack system. A stack is composed of multi-layers of soft rubber and dense mass, as biton and stainless.

Stable operation against a ground motion

A ground motion affects not only the sensitivity of the interferometer, but also the stability of it. Though the suspension system and other isolation system isolate the mirror from seismic motion in a high frequency region as described above, the mirror motion is largely excited in a low frequency region, especially at the resonant frequency of the pendulum. When the Q-value is high enough, the transfer function described by Eq. (3.83) is approximated as $H(\omega_{\rm pen}) \sim Q$. The large motion at the resonant frequency of the pendulum can disturb the operational condition of an interferometer, which affects the stability of the operation, and also the sensitivity of the interferometer. In addition to the longitudinal motion, the rotational motions of the mirrors are also excited at the resonant frequency,

[28] In this part, we concentrate on the vibration isolation for a displacement, the length degree of freedom, of an interferometer. However, in practice, the vertical and orientation vibrations of the mirrors cause a displacement noise coupling with the asymmetries of the isolation system, differences of the gravity direction in mirrors, and miss centering of the laser beam.

[29] In practice, the vibration isolation ratio is degraded by various resonances.

which cause misalignment of the interferometer. The interferometer can be unstable because of the angular fluctuations of the mirrors. This is a severe problem especially in a large-baseline interferometer because a small angular motion cause a large fluctuation of beam spot propagating along a long distance.

In order to operate an interferometer stable for a long observation time, it is necessary to dump the mirror motion and to control the mirror position and orientation. Usually, the resonances of the vibration isolation system is dumped locally, and precise position and orientation are controlled globally.

3.4.4 Noises of the laser source

The laser source for an interferometer is not ideal; it has a frequency noise, intensity noise, and so on. These noises affects the sensitivity coupling with asymmetries of the interferometer and fluctuations around the operational point.

Laser frequency noise

If the both arms of the Michelson interferometer is completely symmetric, the frequency noise of the laser source is rejected at the interference. This rejection ratio is called common-mode-noise rejection ratio (CMRR).

In a Michelson interferometer (including delay-line-Michelson interferometer), the CMRR is mainly limited by the difference of the optical length of the arms, l_-;

$$\delta h_{\rm FM} = \frac{l_-}{l}\frac{\delta\nu_{\rm l}(\omega)}{\nu_{\rm l}} \quad [1/\sqrt{\rm Hz}] \tag{3.84}$$

In the case of Fabry-Perot-Michelson interferometer, the phase fluctuation of the beam reflected by Fabry-Perot cavity is written as

$$\delta\phi^{\rm (F)}_{\rm FP} = \int_{-\infty}^{\infty} H^{\rm (F)}_{\rm FP}(\omega)\delta\nu(\omega)e^{i\omega t}\delta\omega$$

as described in Eq. (3.61). This phase change is canceled out by take the difference in both arm cavities, $\delta\phi^{\rm (F)}_{\rm FPMI} = \epsilon_{\rm CMRR}\delta\phi^{\rm (F)}_{\rm FP}$, where CMRR is written as

$$\epsilon_{\rm CMRR} = 2\left|\frac{H^{\rm (F)}_{{\rm FP}x} - H^{\rm (F)}_{{\rm FP}y}}{H^{\rm (F)}_{{\rm FP}x} + H^{\rm (F)}_{{\rm FP}y}}\right| \tag{3.85}$$

With approximations $r_{\mathrm{E}} \simeq 1$ and $\omega \ll \omega_{\mathrm{c}}$, ϵ_{CMRR} is written as

$$\epsilon_{\mathrm{CMRR}} \sim \frac{L_-}{L} + \frac{\mathcal{F}_-}{\mathcal{F}}. \tag{3.86}$$

This equation shows that the CMRR is limited by the difference of the arm length and finesse, in other words, by the difference of total optical path length.

By using high-quality optical components, it is believed that a CMRR of 1/100 is achievable. So far, a CMRR of 1/300 is experimentally realized with a prototype interferometer [31].

Even if an interferometer has a good CMRR of 1/100, the frequency fluctuation is still a large noise source for the detection of gravitational waves. Thus, the laser frequency is stabilized using cavities: a rigid cavity with a length about a few tens of cm, a independently suspended cavity like mode cleaner, and the arm cavity of the interferometer itself.

Laser intensity noise

A Michelson interferometer converts a phase information of the laser beam to a intensity change at the photo detector. Thus, it is necessary to exclude the effect of intensity fluctuation from the signal port. By setting the operational point to dark fringe, the effect of intensity noise is reduced. In addition, in a modulation scheme, the modulation frequency is usually selected to be over 10 MHz, in which the intensity noise of the laser source is smaller than the shot noise.

However, in practice, there remains a fluctuation around the dark point because of a finite control gain. The residual motion around the fringe couples with the intensity noise of the laser source[30]:

$$\delta x_{\mathrm{int}} = \frac{\delta P}{P} \delta x_{\mathrm{rms}} \quad [\mathrm{m}/\sqrt{\mathrm{Hz}}], \tag{3.87}$$

where δx_{rms} is the residual RMS (root mean square) fluctuation around the dark fringe. Thus, the control gain have to be large enough to suppress the residual RMS deviation, as well as the intensity stabilization of the laser source.

[30] In a power-recycled interferometer, the intensity noise includes the fluctuation of the recycling gain.

Laser mode noise

The fluctuations of the orientation (called beam jitter) and radius of the laser source can be a noise source coupling with misalignment of the interferometer or inhomogeneity of the photo detector [63, 64]. These fluctuations are interpreted to be a fluctuation of the mode of the laser source: the beam orientation error is the mixing of the first-order (and higher) Hermite-Gaussian modes, the beam radius error is the mixing of the second-order (and higher) Hermite-Gaussian modes.

These higher-mode beams are usually rejected by a mode cleaner placed between the laser source and the interferometer. Mode cleaner is, in principle, a Fabry-Perot cavity formed by two mirrors with same and high reflectivity, which has a high finesse and transmissivity[31]. The mode cleaner is set to resonate with the TEM_{00} mode beam, and not to resonate with the higher-mode beams. In this condition, only TEM_{00} mode beam transmits through the mode cleaner and higher-mode beam is reflected back. In order to reduce the effect of the seismic noise, the mode cleaner has a long baseline, and its mirrors are suspended to isolate from the seismic motion [65, 66, 67].

3.4.5 Residual gas noise

The fluctuation of the gas along the optical pass cause a fluctuation of a reflective index, resulting in the change in optical pass length. Thus, the interferometer is housed in a vacuum system[32]. The residual noise level is written as [68]

$$\delta h_{\mathrm{rg}} = \left[\frac{4\sqrt{2\pi}}{L} \frac{(n_0 - 1)^2}{(A_0/V_0) u_0 \sqrt{L\lambda_{\mathrm{l}}}} \left(\frac{p}{p_0} \right) \left(\frac{T_0}{T} \right)^{3/2} \right]^{1/2} \quad [1/\sqrt{\mathrm{Hz}}], \tag{3.88}$$

[31] A ring-type cavity comprised of three or four mirrors is often used as a mode cleaner. Compared with ring-type, a mode cleaner formed by two mirrors are called linear-type mode cleaner. In principle, there is little difference between a ring-type and linear-type as long as the angle of the the incident and reflected beams on the mirror is small enough. However, a ring-type cavity has an advantage that the main interferometer is less affected by the back-scattered light from the mode cleaner.

[32] The vacuum system has other roles: to avoid a loss of laser power by the absorption and scattering of the gas, to keep the optical components from shaken by a fluctuation of gas, and from the contamination of the optics by dusts.

where A_0: Avogadro's number[33], V_0: volume of one mole gas at standard temperature (T_0) and pressure (p_0)[34], n_0: reflective index of the gas, and u_0: mean velocity of the gas molecule at standard state. In order to reduce this level to 10^{-24} $1/\sqrt{\mathrm{Hz}}$ with a 3 km baseline length, the pressure of 10^{-6} Pa is required.

3.4.6 Noises due to control of the interferometer

In order to operate an interferometric gravitational wave detector, it is necessary to control the position of the optical components. However, the control system can introduce noises without a proper design. Though this is not a fundamental noise, careful consideration and design are required to avoid this noise in practice.

Noises due to the control loops

In case of Fabry-Perot-type interferometer, if the arm cavities are controlled to resonate with the incident laser beam independently, the control system also suppresses the gravitational wave signal, resulting in the increase of noise level. This affect is avoided by narrowing the control frequency band for the arm mirrors than the observation band (called loose lock). However, with a narrow control band, the fluctuation of the interferometer remain because of a low control gain. This residual fluctuation cause additional noises. Moreover the interferometer will not be operated stably for a long observation time with a narrow control band. Thus, the arm mirrors must be controlled using the differential motion signal of arms, i.e., the signal for a gravitational wave. In this case, the interferometer can be operated with wide frequency band (called tight lock) without suppressing the signal of gravitational waves. The gravitational wave signal is obtained from the feedback signal to the mirrors.

Besides the differential motion of the arms, the other degrees of freedom must be controlled with auxiliary control loops. However, in general, S/N (signal-to-noise ratio) of the signal for these control is not as good as that for the main control loop. Thus, the control loops must be designed so that the optical components would not be shaken by feeding back worse S/N signals. In most cases,

[33]Avogadro's number: $A_0 = 6.02 \times 10^{23}$.

[34]Volume of one mole gas at standard state: $V_0 = 22.4 \times 10^{-3}$ [m^3/mol].

the control bandwidth of the auxiliary control loops must be much narrower than the observation frequency band.

Actuator noise and dynamic range

The mirror actuator driver also has an electronic noise. Since the driver noise shakes a mirror directly, it should be designed to have extremely low noise. The driver noise is reduced by decreasing the efficiency of the actuator. However, in this case, the dynamic range of the actuator is also reduced. Since the actuator must have sufficient dynamic range to compensate the motion of the interferometer, the efficiency of the actuator is optimized considering the driver noise and the required dynamic range. A multi-stage actuator, the combination of a high-dynamic-range actuator and a low-noise actuator will be useful if one actuator does not satisfy the noise level and dynamic range simultaneously.

Chapter 4

Signal separation scheme

In this Chapter, we describe the signal extraction and control scheme of a power-recycled Fabry-Perot-Michelson interferometer.

To behave as a free mass, each mirror of an interferometric gravitational wave detector is suspended as pendulum. Though the suspension system has another role to isolate the mirror from the seismic motion at the observation frequency band, the mirror is largely excited by the the seismic motion at the resonant frequency of the pendulum. Thus, it is necessary to control an interferometer and keep it at the operational point. The signals necessary for control of a power-recycled Fabry-Perot-Michelson interferometer is extracted with a scheme called frontal modulation. However, the control signal for the recycling cavity length cannot be separated independently of other signals.

In order to solve this signal mixing problem, we have invented a new scheme to separate the control signals by an adjustment of the optical parameters of the interferometer. One of the advantage of this scheme is that this scheme does not require any additional optical components nor modulation to separate signals.

In the first half of this Chapter, we describe the signal-extraction scheme with frontal modulation, which is the basis of our signal-separation scheme. The principle of the signal-separation scheme is described in the latter half of this Chapter. This Chapter contains the following Sections.

- **Overview of the control system.** The overview of the signal-extraction and control scheme of a power-recycled Fabry-Perot-Michelson interferometer.

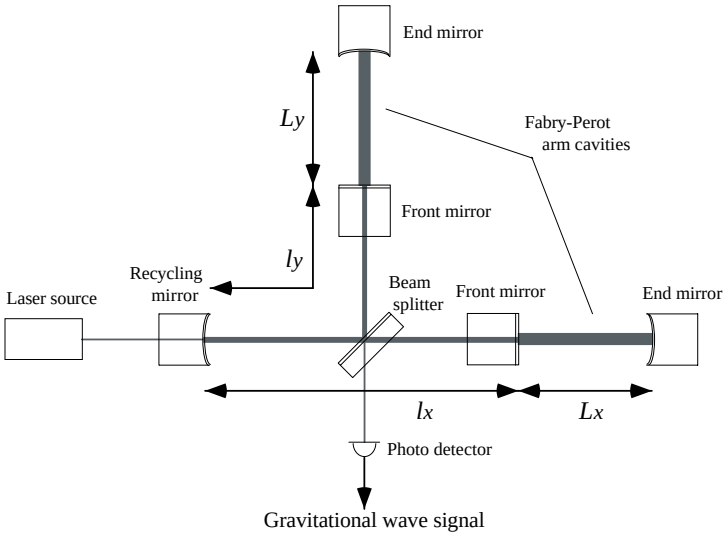

Figure 4.1: Power recycled Fabry-Perot-Michelson interferometer. Four degrees of freedom must be controlled to operate the interferometer.

- **Frontal modulation.** Modulation and demodulation for signal extraction. Response of the interferometer.
- **Signal sensitivity.** Sensitivities of the signals expected with frontal modulation under operational conditions.
- **Signal-separation scheme.** The signal-separation scheme with adjustment of optical parameters.

4.1 Overview of control schemes

4.1.1 Power-recycled Fabry-Perot-Michelson interferometer

Figure. 4.1 shows the optical configuration of a Fabry-Perot-Michelson interferometer with power recycling. To operate this interferometer, four degrees of longitudinal freedom must be controlled: the lengths of the arm cavities (δL_x and δL_y), the lengths between the recycling mirror and the front mirrors (δl_x and δl_y). The operational point is selected so that the interferometer would be oper-

ated at its highest sensitivity, i.e., so that the phase changes due to gravitational waves are maximized. Thus, the operational condition is described as follows. (1) The arm cavities are controlled to resonate with the incident laser beam to have maximum phase enhancement. (2) The interference fringe is set dark to maximize the differential phase change information and minimize the effect of the shot noise at the detection port. In addition, the dark fringe condition is indispensable for power recycling. (3) The recycling cavity is controlled to resonate with the incident laser beam to maximize the laser power on the beamsplitter.

It is convenient to describe the operational point of the interferometer by the round-trip phases which beams experience between mirrors. The operational point of the arm cavities are described by the round-trip phase Φ_x and Φ_y,

$$\Phi_{\mathrm{dof}} = \frac{2L_{\mathrm{dof}}\Omega_{\mathrm{l}}}{c}, \tag{4.1}$$

where the index '$_{\mathrm{dof}}$' represents '$_x$' and '$_y$'. The round-trip phases between the recycling mirror and the front mirrors are represented by ϕ_x and ϕ_y:

$$\phi_{\mathrm{dof}} = \frac{2l_{\mathrm{dof}}\Omega_{\mathrm{l}}}{c}. \tag{4.2}$$

The operational point of the interferometer, the four longitudinal freedom of a power-recycled Fabry-Perot-Michelson interferometer, is expressed by Φ_x, Φ_y, ϕ_x, and ϕ_y.

The operational condition of the interferometer is described as

$$\Phi_x = \Phi_y = \phi_x = \phi_y = 0. \tag{4.3}$$

Details of the operational condition is explained in the following Sections.

4.1.2 Frontal modulation

Frontal modulation[1] is the scheme to extract the phase information from the interferometer: the phase changes due to gravitational waves, mirror motion, and the fluctuation of the laser frequency [19, 20]. Figure 4.2 shows the schematic diagram of with frontal modulation. The incident laser beam is phase-modulated in front of the interferometer, and an asymmetry is introduced between l_x and l_y.

[1]This scheme is also called pre-modulation or Schnupp modulation.

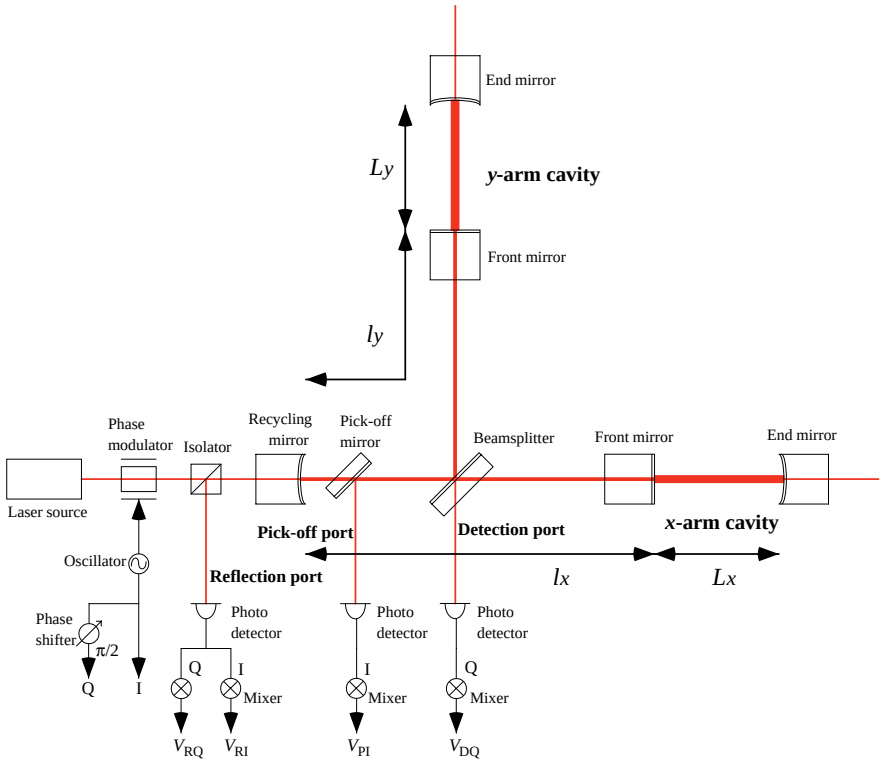

Figure 4.2: Schematic diagram of frontal modulation. An asymmetry (l_-) is introduced between l_x and l_y, and the incident laser beam is phase-modulated at an angular frequency of $\omega_{\rm m}$. Each output of a photo detector is demodulated with a mixer. 'I' and 'Q' represents demodulation phase: I: in-phase, Q: quadrature-phase.

Using frontal modulation, signals necessary for the control of the interferometer are extracted as the differential and common phase change in the arm cavities ($\delta\Phi_- = \delta\Phi_x - \delta\Phi_y$, $\delta\Phi_+ = \delta\Phi_x + \delta\Phi_y$) and the differential and common phase change in the recycling mirror and front mirrors ($\delta\phi_- = \delta\phi_x - \delta\phi_y$, $\delta\phi_+ = \delta\phi_x + \delta\phi_y$). $\delta\Phi_-$ contains the gravitational wave signal, and $\delta\Phi_+$ contains the frequency fluctuation signal.

The beam from the laser source is phase-modulated at an angular frequency of $\omega_{\rm m}$. The laser beam after the phase modulation can be considered to contain three frequency beams[2]: the carrier which has the same angular frequency as that of the original laser beam, and the sidebands which have an angular frequency

[2]Here we assume that the modulation index is small enough for simplicity of the explanation.

higher and lower by $\omega_{\rm m}$ than that of the original laser beam. The modulation angular frequency is selected so that the sidebands should not resonate with the arm cavities, and the length of the recycling cavity $l_+/2$ is selected so that the sidebands should resonate with the recycling cavity.

The phase-modulated laser beam is introduced into the interferometer, divided in two orthogonal direction with the beamsplitter, reflected with the arm cavity, and recombined again on the beamsplitter. Under the operational condition, the interference fringe of the carrier is dark at the detection port[3], and bright in the direction toward the laser source[4]. On the other hand, the interference fringe of the sidebands is not dark at the detection port in general because an asymmetry is introduced between l_x and l_y; the sidebands have different interference condition from the carrier. When the fringe of the carrier changes by gravitational waves, the carrier leaks to the detection port and beats with the residual sidebands. Gravitational waves are detected as signals by demodulating this beat at the modulation frequency with suitable phase (quadrature-phase).

Besides the detection port signal, signals for the control of the interferometer is extracted by demodulating the output of photo detectors at the pick-off port and reflection port with two phases (in-phase and quadrature-phase). In Fig. 4.2, the extracted signals are written as $V_{\rm DQ}$, $V_{\rm RQ}$, $V_{\rm PI}$, and $V_{\rm RI}$, which are used for the control of $\delta\Phi_-$, $\delta\phi_-$, $\delta\Phi_+$, and $\delta\phi_+$, respectively. Where the index '$_{\rm D}$', '$_{\rm R}$', and '$_{\rm P}$' denote the corresponding output ports of the interferometer, and the index '$_{\rm I}$' and '$_{\rm Q}$' denote the corresponding demodulation phases.

One of the advantages of this scheme is its simplicity: a frontal modulation scheme does not require any additional optical components or additional degree of freedom to be controlled. In addition, since the phase modulator is placed out of the interferometer, we can use a modulator with smaller aperture and lower power. The effect of wave front distortions by the modulator can be reduced by putting it in front of the mode cleaner, which result in a higher contrast of the interferometer.

[3]This port is also called the antisymmetric port or the dark port. The term 'dark port' is not used in this thesis, because the reflection port also becomes dark with a proper selection of the recycling mirror under the operational condition.

[4]This direction is called the symmetric port of the beamsplitter.

4.1.3 Signal separation

As described above, all of the signals necessary for the longitudinal control of a power-recycled Fabry-Perot-Michelson interferometer are extracted using a frontal modulation scheme. However, there is a difficulty in extracting the signal for the control of the recycling cavity length ($\delta\phi_+$) independently; this signal is mixed with the large $\delta\Phi_+$ signal[5]. The mixing among the signals complicates the design of the control system which maintains the stability and high sensitivity at the same time [19]. It is therefore desirable to obtain well-separated signals. Such signals would simplify the design and study of the control system, and the operation of the interferometer. Some methods to obtain such signals have been proposed or tested.

One method to separate signals is to combine the signals linearly by electronic circuits (the decoding circuits) or by digital processing [19, 20, 69, 70]. Though the four signals are extracted separately by this linear-combination operation, the signal-to-noise ratios of these signals can decrease with a proper design because the noises, such as the shot noise, are also combined.

The other method to separate signals is to use an additional carrier, called a subcarrier [21, 22, 70]. The frequency of the subcarrier is offset from that of the main carrier. The frequency-shifted subcarrier is superimposed on the main carrier with a beamsplitter after phase modulation. The frequency offset and the modulation frequency for the subcarrier are selected so that the subcarrier and its RF sidebands do not resonate with the arm cavities, but resonate with the recycling cavity. Using a frequency-shifted subcarrier, the information about the power-recycled Michelson part of the interferometer ($\delta\phi_-$ and $\delta\phi_+$) is obtained independently of $\delta\Phi_-$ and $\delta\Phi_+$ because the subcarrier and its sidebands are unaffected by the phase changes in the arm cavities. However, this method complicates the optical setup for introduction of the subcarrier.

The scheme described in this thesis is a signal-separation technique by adjusting the optical parameters of the interferometer [33]. The point of this method is to adjust the reflectivity of the recycling mirror so as to maximize the gain of

[5]This problem is not a characteristic one with frontal modulation. The phase change of the carrier is much more sensitive to $\delta\Phi_+$ than $\delta\phi_+$ at the bright fringe of the interference. This is because $\delta\Phi_+$ information is enhanced in the arm cavities.

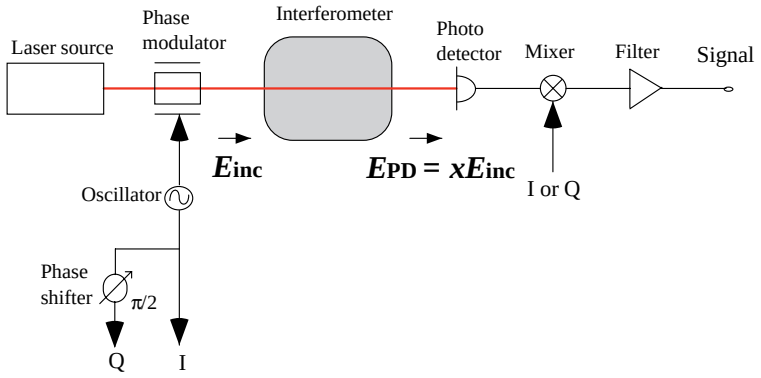

Figure 4.3: Signal extraction scheme using modulation and demodulation. The interferometer is regarded as a black box which causes amplitude and phase change onto the incident laser beams.

the sidebands, not the gain of the carrier. By this modification of the optical parameters, the signals are extracted separately at only a little expense of the recycling gain. This scheme does not call for any additional optics or electronic components to extract the δl_+ signal, and maintains the advantage of simplicity with a frontal modulation technique.

4.2 Frontal modulation

In this Section, the general expressions of the signals extracted with frontal modulation are described. In frontal modulation, it is possible to consider the modulation system and the interferometer separately. The signal extraction system with modulation and demodulation is described in the first half of this Section, and the response of the interferometer is described in the latter half.

4.2.1 Modulation and demodulation

A laser-interferometric gravitational wave detector is a device to detect the phase change of the laser beam caused by gravitational waves. However, the phase of the laser beam is not detected directly with a photo detector, because the frequency

of the laser beam is much higher than the response speed of a photo diode[6]. A photo diode detects the power of the laser beam averaged during the response time scale. The phase information of the laser beam is lost in the averaging process.

Thus, the phase modulation scheme is used to detect the phase change in the laser beam[7]. Figure 4.3 shows the diagram of the phase detection scheme using modulation and demodulation. In a frontal modulation technique, the laser beam from the laser source is phase-modulated in front of the interferometer. The phase-modulated beam is considered as the super position of monochromatic laser beams: a carrier and sidebands. The carrier has the same frequency as that of the original laser beam. On the other hand, the frequency of the sidebands are shifted by integral multiples of the modulation frequency. The laser beam is detected with the photo detector after experiencing amplitude and phase change in the interferometer. The amplitude and phase change in the interferometer is detected by demodulating the output of the photo detector.

Phase modulation

The laser beam from the laser source is expressed as

$$E_{\mathrm{l}} = E_0 e^{\mathrm{i}\Omega_{\mathrm{l}} t}, \tag{4.4}$$

where E_0 is the amplitude of the laser beam. In this thesis, amplitudes of laser beam are normalized to have a unit of $\sqrt{\mathrm{W}}$. Thus the output power of the laser source is written as

$$P_{\mathrm{l}} = |E_{\mathrm{l}}|^2 \quad [\mathrm{W}]. \tag{4.5}$$

This laser beam is introduced into the interferometer after phase modulation at an angular frequency of ω_{m} and a modulation index of m_{m}. The modulation

[6]The frequency of a Nd:YAG laser (infrared) is about 300 THz. The response speed of a photo diode is about 100 MHz at best.

[7]The phase change in the laser beam can be detected without phase modulation by proper selection of the operational point. The Michelson interferometer converts the phase change to the power change in the interference fringe as described in Eq. (3.2). This phase detection scheme is called DC-scheme or differential scheme. Though the differential scheme is simple and convenient, it is incompatible with power recycling.

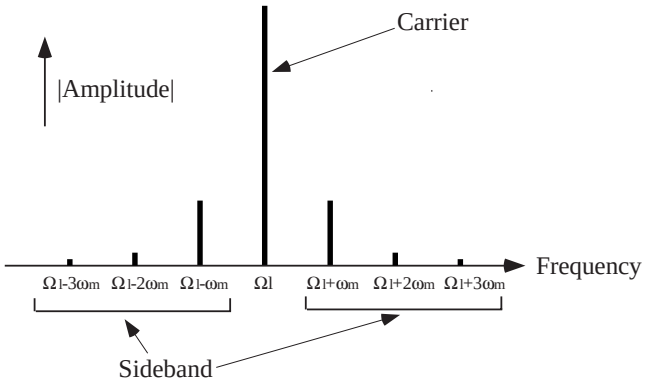

Figure 4.4: Phase modulated laser beam is considered to be the superposition of monochromatic beams; the angular frequencies are separated by the modulation frequency ($\omega_{\rm m}/2\pi$). The laser beam which has the same frequency as that of the original laser beam is called carrier, and the laser beam generated by the modulation is called sidebands.

frequency is usually selected to be a few tens of megahertz in order to avoid the intensity noise of the laser source. The incident laser beam into the interferometer is written as

$$E_{\rm inc} = E_{\rm l} e^{{\rm i}m_{\rm m}\cos\omega_{\rm m}t}. \tag{4.6}$$

Here, Eq. (4.6) is rewritten using Bessel functions J_n as[8]

$$E_{\rm inc} = E_{\rm l}\sum_{n=-\infty}^{\infty} {\rm i}^n J_n e^{{\rm i}n\omega_{\rm m}t} \tag{4.7}$$

$$= E_0\sum_{n=-\infty}^{\infty}\left\{{\rm i}^n J_n e^{{\rm i}(\Omega_{\rm l}+n\omega_{\rm m})t}\right\}. \tag{4.8}$$

[8]The exponential part is expanded as

$$e^{{\rm i}m_{\rm m}\cos\omega_{\rm m}t} = \sum_{n=-\infty}^{\infty}{\rm i}^n J_n e^{{\rm i}n\omega_{\rm m}t}.$$

Bessel functions satisfy the following expressions:

$$J_{-n} = (-1)^n J_n$$
$$J_n \simeq \frac{1}{n!}\left(\frac{m_{\rm m}}{2}\right)^n \quad (m_{\rm m}\ll 1).$$

The Bessel functions $J_n(m_{\rm m})$ are written as J_n for simplicity of expressions in this thesis.

Equation (4.8) show that the laser beam after the phase modulation is considered as the superposition of laser beams which have the angular frequency of $\Omega_{\rm l}+n\omega_{\rm m}$ (Fig. 4.4). The laser beam with the same angular frequency as that of the beam from the laser source ($\Omega_{\rm l}$) is called carrier. The laser beams with shifted angular frequencies from the carrier ($\Omega_{\rm l}+n\omega_{\rm m}$, n: integer) are called n-th order sidebands. In addition, the sidebands with higher frequency than the carrier ($n>0$) are called upper sidebands, and the sidebands with lower frequency than the carrier ($n<0$) are called lower sidebands. The incident laser beam, Eq. (4.7), is rewritten as

$$E_{\rm inc} = \sum_{n=-\infty}^{\infty} E_{{\rm inc}n} e^{{\rm i}n\omega_{\rm m}t} \tag{4.9}$$

$$E_{{\rm inc}n} = {\rm i}^n J_n E_{\rm l}, \tag{4.10}$$

where, $E_{{\rm inc}n}$ represents each monochromatic laser beams superimposed in the incident laser beam; $E_{\rm inc0}$ represents the carrier, and $E_{{\rm inc}n}$ ($n\neq 0$) represents the nth-order sidebands[9]. $E_{{\rm inc}n}$ satisfies the following equations:

$$E_{{\rm inc}-n} = E_{{\rm inc}n} \tag{4.11}$$

$$E_{{\rm inc}n+1} E_{{\rm inc}n}^{*} = {\rm i} J_n J_{n+1} P_{\rm l}. \tag{4.12}$$

Photo detection

When a photo detector receives a laser beam with sidebands written as

$$E_{\rm PD} = \sum_{n=-\infty}^{\infty} E_{{\rm PD}n} e^{{\rm i}n\omega_{\rm m}t},$$

[9]The carrier and the low-order sidebands are written as

$$E_{\rm inc0} = J_0 E_{\rm l}$$
$$E_{\rm inc1} = E_{\rm inc-1} = {\rm i} J_1 E_{\rm l}$$
$$E_{\rm inc2} = E_{\rm inc-2} = -J_2 E_{\rm l},$$

the photo current caused by the input beam is written as

$$I_{\mathrm{PD}} = \eta |E_{\mathrm{PD}}|^2 = \eta \left[\sum_{n=-\infty}^{\infty} \sum_{m=-\infty}^{\infty} E_{\mathrm{PD}m} E_{\mathrm{PD}m-n}^{*} e^{\mathrm{i}n\omega_{\mathrm{m}}t} \right]$$
$$= \sum_{n=-\infty}^{\infty} I_{\mathrm{PD}n} e^{\mathrm{i}n\omega_{\mathrm{m}}t} \quad [\mathrm{A}], \tag{4.13}$$

where η [A/W] is the photo efficiency of the photo diode. $I_{\mathrm{PD}n}$ represents the photo current at the angular frequency of $n\omega_{\mathrm{m}}$:

$$I_{\mathrm{PD}n} = \eta \sum_{m=-\infty}^{\infty} E_{\mathrm{PD}m} E_{\mathrm{PD}m-n}^{*}. \tag{4.14}$$

Equation (4.13) shows that the photo current contain DC photo current and integer multiple element of the modulation frequency. The photo current at the modulation frequency ($n = 1$) is written as[10]

$$I_{\mathrm{PD1}} = \eta \sum_{m=0}^{\infty} \left[E_{\mathrm{PD}m+1} E_{\mathrm{PD}m}^{*} + E_{\mathrm{PD}-m} E_{\mathrm{PD}-m-1}^{*} \right]. \tag{4.15}$$

Demodulation

The modulation frequency element of the photo current (I_{PD1}) is extracted by demodulating the the output of the photo diode at the angular frequency of ω_{m}. The demodulation is realized with a mixer and a low pass filter. The mixer down-converts the ω_{m} elements of the photo current to the frequency region near DC by multiplying the output of the photo diode and local oscillator which has the angular frequency of ω_{m}. The low pass filter rejects the higher frequency elements over ω_{m} from the output of the mixer.

Two independent outputs are obtained by the demodulation depending on the phase of the local oscillator: in-phase and quadrature-phase. The output of

[10] $I_{\mathrm{PD}n}$ satisfies the equation

$$I_{\mathrm{PD}-n} = I_{\mathrm{PD}n}^{*}.$$

the demodulator is described as

$$\begin{aligned} V_{\mathrm{PDI}} &= \frac{g_{\mathrm{det}}}{T}\int_{t-T}^{t} I_{\mathrm{PD}}(t')\cos\omega_{\mathrm{m}}t'dt' \\ &= \frac{g_{\mathrm{det}}}{2}\left(I_{\mathrm{PD1}}+I_{\mathrm{PD}-1}\right) = g_{\mathrm{det}}\mathrm{Re}\{I_{\mathrm{PD1}}\} \\ &= g_{\mathrm{det}}\eta\sum_{n=0}^{\infty}\mathrm{Re}\left\{E_{\mathrm{PD}n+1}E_{\mathrm{PD}n}^{*}+E_{\mathrm{PD}-n}E_{\mathrm{PD}-n-1}^{*}\right\}, \end{aligned} \tag{4.16}$$

when $\cos\omega_{\mathrm{m}}t$ (in-phase) is used as the local oscillator. The gain of the photo detector and the efficiency of the demodulator are represented by the coefficient g_{det} [Ω]. On the other hand, when $\sin\omega_{\mathrm{m}}t$ (quadrature-phase) is used as the local oscillator, the output of the demodulator is written as

$$\begin{aligned} V_{\mathrm{PDQ}} &= \frac{g_{\mathrm{det}}}{T}\int_{t-T}^{t} I_{\mathrm{PD}}(t')\sin\omega_{\mathrm{m}}t'dt' \\ &= \frac{g_{\mathrm{det}}}{2\mathrm{i}}\left(-I_{\mathrm{PD1}}+I_{\mathrm{PD}-1}\right) = -g_{\mathrm{det}}\mathrm{Im}\{I_{\mathrm{PD1}}\} \\ &= -g_{\mathrm{det}}\eta\sum_{n=0}^{\infty}\mathrm{Im}\left\{E_{\mathrm{PD}n+1}E_{\mathrm{PD}n}^{*}+E_{\mathrm{PD}-n}E_{\mathrm{PD}-n-1}^{*}\right\}. \end{aligned} \tag{4.17}$$

Equations (4.16) and (4.17) show that the real and imaginary part of I_{PD1} are extracted depending on the phase of the local oscillator[11].

Signal corresponding to the response of the interferometer

The phase-modulated laser beam E_{inc} is detected with the photo detector after experiencing amplitude and phase change in the interferometer. The each frequency element of the input laser beam on the photo detector is written as

$$E_{\mathrm{PD}n} = x_n E_{\mathrm{inc}n}, \tag{4.18}$$

[11] In general, since the local oscillator with the phase of θ_{m} is written as

$$\cos(\omega_{\mathrm{m}}t+\theta_{\mathrm{m}}) = \cos\omega_{\mathrm{m}}t\cos\theta_{\mathrm{m}} - \sin\omega_{\mathrm{m}}t\sin\theta_{\mathrm{m}},$$

the output of the demodulator is written as the linear combination of the in-phase and quadrature-phase outputs:

$$\begin{aligned} V_{\mathrm{PD}\theta_{\mathrm{m}}} &= \frac{g_{\mathrm{det}}}{T}\int_{t-T}^{t} I_{\mathrm{PD}}(t')\cos(\omega_{\mathrm{m}}t'+\theta_{\mathrm{m}})dt' \\ &= V_{\mathrm{PDI}}\cos\theta_{\mathrm{m}} - V_{\mathrm{PDQ}}\sin\theta_{\mathrm{m}}. \end{aligned}$$

where x_n is a complex number which represents the amplitude and phase change of the the carrier and the nth-order sidebands. Substituting this equation into Eq. (4.16), we obtain the in-phase demodulation output:

$$\begin{aligned} V_{\rm PDI} &= g_{\rm det}\eta \sum_{n=0}^{\infty} {\rm Re}\left\{ x_{n+1} E_{{\rm inc}n+1} x_n^* E_{{\rm inc}_n}^* + x_{-n} E_{{\rm inc}-n} x_{-n-1}^* E_{{\rm inc}_{-n-1}}^* \right\} \\ &= g_{\rm det}\eta P_{\rm l} \sum_{n=0}^{\infty} J_n J_{n+1} {\rm Im}\{ x_n x_{n+1}^* + x_{-n} x_{-n-1}^* \}, \end{aligned} \tag{4.19}$$

where we use Eq. (4.12). In the quadrature-phase demodulation case, we obtain the following expression from Eq. (4.17):

$$\begin{aligned} V_{\rm PDQ} &= -g_{\rm det}\eta \sum_{n=0}^{\infty} {\rm Im}\left\{ x_{n+1} E_{{\rm inc}n+1} x_n^* E_{{\rm inc}_n}^* + x_{-n} E_{{\rm inc}-n} x_{-n-1}^* E_{{\rm inc}_{-n-1}}^* \right\} \\ &= g_{\rm det}\eta P_{\rm l} \sum_{n=0}^{\infty} J_n J_{n+1} {\rm Re}\{ -x_n x_{n+1}^* + x_{-n} x_{-n-1}^* \}. \end{aligned} \tag{4.20}$$

The expressions for the extracted signals from the interferometer are obtained by substituting x_n into Eqs. (4.19) and (4.20)[12]. These equations show that the signal is produced by the product of the nth-order beam and the $n+1$th-order beam; taking only the first order of the modulation index, the signal is produced by the product of the carrier and the first order sidebands.

Shot noise

Here, we describe the expressions for the effect of the shot noise in the signal[13]. The DC current of the photo diode is written as

$$\begin{aligned} I_{\rm PD0} &= \eta \sum_{n=-\infty}^{\infty} x_n E_{{\rm inc}n} x_n^* E_{{\rm inc}_n}^* \\ &= \eta P_{\rm l} \sum_{n=-\infty}^{\infty} J_n^2 x_n x_n^* \quad [{\rm A}]. \end{aligned} \tag{4.21}$$

[12]These equations are written as

$$\begin{aligned} V_{\rm PDI} &= g_{\rm det}\eta P_{\rm l} \times \left[J_0 J_1 {\rm Im}\{ x_0 x_1^* + x_0 x_{-1}^* \} + J_1 J_2 {\rm Im}\{ x_1 x_2^* + x_{-1} x_{-2}^* \} + \cdots \right], \\ V_{\rm PDQ} &= g_{\rm det}\eta P_{\rm l} \times \left[J_0 J_1 {\rm Re}\{ -x_0 x_1^* + x_0 x_{-1}^* \} + J_1 J_2 {\rm Re}\{ -x_1 x_2^* + x_{-1} x_{-2}^* \} + \cdots \right]. \end{aligned}$$

[13]Here, we neglect the effect of the non-stationary shot noise.

The shot noise is written as

$$I_{\mathrm{PDshot}n} = \sqrt{2eI_{\mathrm{PD0}}} \quad [\mathrm{A}/\sqrt{\mathrm{Hz}}]. \tag{4.22}$$

Since the $e^{\mathrm{i}\omega_{\mathrm{m}}t}$ element (I_{PDshot1}) and the $e^{-\mathrm{i}\omega_{\mathrm{m}}t}$ element ($I_{\mathrm{PDshot}-1}$) of the photo current caused by the shot noise have no correlation, the effect of the shot noise in the output of the demodulator is written as

$$V_{\mathrm{PDshot}} = \frac{g_{\mathrm{det}}}{2}\sqrt{I_{\mathrm{PDshot1}}^2 + I_{\mathrm{PDshot}-1}^2} = g_{\mathrm{det}}\sqrt{eI_{\mathrm{PD0}}} \quad [\mathrm{V}/\sqrt{\mathrm{Hz}}]. \tag{4.23}$$

Sensitivity of the signal

The sensitivity of a signal is represented by the change in the signal corresponding to the change in the interferometer. When the change in the interferometer is small enough, the signal is considered to have a linear response:

$$\delta V_{\mathrm{PDdem}} = \frac{\partial V_{\mathrm{PDdem}}}{\partial\theta}\delta\theta, \tag{4.24}$$

where θ represents the phase (Φ_-, ϕ_-, Φ_+, and ϕ_+), and index '$_{\mathrm{dem}}$' represents the demodulation phase ('$_{\mathrm{I}}$' or '$_{\mathrm{Q}}$'). In this equation, the derivative $\partial V_{\mathrm{PDdem}}/\partial\theta$ represents the sensitivity of the signal V_{PDdem} to the degree of freedom θ. From Eqs. (4.19) and (4.20), the sensitivity of the signal is written as

$$\begin{aligned}\frac{\partial V_{\mathrm{PDI}}}{\partial\theta} &= g_{\mathrm{det}}\eta P_{\mathrm{I}}\sum_{n=0}^{\infty} J_n J_{n+1} \times \\ &\quad \mathrm{Im}\left\{x_n\frac{\partial x_{n+1}^*}{\partial\theta} + x_{-n}\frac{\partial x_{-n-1}^*}{\partial\theta} + \frac{\partial x_n}{\partial\theta}x_{n+1}^* + \frac{\partial x_{-n}}{\partial\theta}x_{-n-1}^*\right\} \qquad (4.25)\\ \frac{\partial V_{\mathrm{PDQ}}}{\partial\theta} &= g_{\mathrm{det}}\eta P_{\mathrm{I}}\sum_{n=0}^{\infty} J_n J_{n+1} \times \\ &\quad \mathrm{Re}\left\{-x_n\frac{\partial x_{n+1}^*}{\partial\theta} + x_{-n}\frac{\partial x_{-n-1}^*}{\partial\theta} - \frac{\partial x_n}{\partial\theta}x_{n+1}^* + \frac{\partial x_{-n}}{\partial\theta}x_{-n-1}^*\right\} \qquad (4.26)\end{aligned}$$

The sensitivity of the signal limited by the shot noise (the shot-noise level) is written as the ratio of the shot noise and the sensitivity of the signal:

$$\theta_{\mathrm{shot}} = \frac{V_{\mathrm{PDshot}}}{\left(\dfrac{\partial V_{\mathrm{PDdem}}}{\partial\theta}\right)}. \tag{4.27}$$

Table 4.1: Notations of indexes for reflectivity and transmissivity used in this thesis.

Notations of indexes	
Index	Object
F	Front mirror
E	End mirror
R	Recycling mirror
BS	Beam splitter
P	Pick-off mirror
cav	Fabry-Perot cavity
com	Compound mirror
rec	Recycling cavity, reflection port
det	Detection port
pick	Pick-off port

4.2.2 Static response of an interferometer

We have shown the expressions for the signals and its sensitivities obtained by the modulation and demodulation system in Eqs. (4.19), (4.20), (4.25), (4.26). Here, we describe the response of the power-recycled Fabry-Perot-Michelson interferometer (x_n): the transmissivities and reflectivity of the interferometer from the input port to the output ports. We consider three output ports: the detection port, the reflection port, and the pick-off port.

Fabry-Perot-Michelson interferometer

The reflectivity of a Fabry-Perot cavity is shown is Section 3.2.

$$r_{\rm cav}(\Phi) = -r_{\rm F} + \frac{t_{\rm F}^2 r_{\rm E} e^{-{\rm i}\Phi}}{1 - r_{\rm F} r_{\rm E} e^{-{\rm i}\Phi}}.$$

The reflected laser beams from the arm cavities are recombined on the beamsplitter (Fig. 4.5). After the interference, the transmissivity of the compound mirror to the detection port $t_{\rm com}$ and the reflectivity toward the laser source $r_{\rm com}$

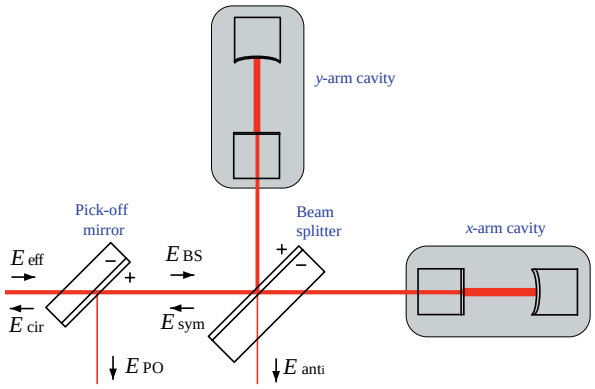

Figure 4.5: Field around the beamsplitter of Fabry-Perot-Michelson interferometer. The beam going upward of this figure from the pick-off mirror and the transmitted beams through the cavities are not drawn.

are written as[14]

$$r_{\rm com}(\theta_{\rm op}) = \frac{E_{\rm cir}}{E_{\rm eff}} = t_{\rm P}^2 \left\{ t_{\rm BS}^2 r_{{\rm cav}x}(\Phi_x) e^{-{\rm i}\phi_x} + r_{\rm BS}^2 r_{{\rm cav}y}(\Phi_y) e^{-{\rm i}\phi_y} \right\} \tag{4.28}$$

$$t_{\rm com}(\theta_{\rm op}) = \frac{E_{\rm anti}}{E_{\rm eff}} = t_{\rm BS} r_{\rm BS} t_{\rm P} \left\{ r_{{\rm cav}x}(\Phi_x) e^{-{\rm i}\phi_x} - r_{{\rm cav}y}(\Phi_y) e^{-{\rm i}\phi_y} \right\}, \tag{4.29}$$

where indexes '$_{\rm BS}$' and '$_{\rm P}$' denote the beamsplitter and the pick-off mirror, respectively. $\theta_{\rm op}$ represents the operational point of the interferometer, the function of Φ_x, Φ_y, ϕ_x, and ϕ_y (or Φ_-, ϕ_-, Φ_+, and ϕ_+).

Here, Eq. (4.28) is rewritten using the sum and difference of ϕ_+ and ϕ_- as

$$r_{\rm com}(\theta_{\rm op}) = e^{-{\rm i}\frac{\phi_+}{2}} \left\{ r_{\rm com+} \cos\left(\frac{\phi_-}{2}\right) - {\rm i} r_{\rm com-} \sin\left(\frac{\phi_-}{2}\right) \right\}, \tag{4.30}$$

where $r_{\rm com+}$ and $r_{\rm com-}$ correspond to the sum and difference of two arms:

$$r_{\rm com+} = t_{\rm P}^2 \left\{ t_{\rm BS}^2 r_{{\rm cav}x}(\Phi_x) + r_{\rm BS}^2 r_{{\rm cav}y}(\Phi_y) \right\} \tag{4.31}$$

$$r_{\rm com-} = t_{\rm P}^2 \left\{ t_{\rm BS}^2 r_{{\rm cav}x}(\Phi_x) - r_{\rm BS}^2 r_{{\rm cav}y}(\Phi_y) \right\}. \tag{4.32}$$

If both arm is completely symmetric, $r_{\rm com-} = 0$.

Same as $r_{\rm com}$, $t_{\rm com}$ in Eq. (4.29) is rewritten as

$$t_{\rm com}(\theta_{\rm op}) = e^{-{\rm i}\frac{\phi_+}{2}} \left\{ t_{\rm com-} \cos\left(\frac{\phi_-}{2}\right) - {\rm i} t_{\rm com+} \sin\left(\frac{\phi_-}{2}\right) \right\}. \tag{4.33}$$

[14] In the calculation, we consider that the recycling mirror, the pick-off mirror, and the beamsplitter are placed close to one another, and that the photo detectors at the output ports of the interferometer are placed at the same distance from the interferometer.

Where $t_{\mathrm{com}+}$ and $t_{\mathrm{com}-}$ correspond to the sum and difference of two arms:

$$t_{\mathrm{com}+} = t_{\mathrm{BS}} r_{\mathrm{BS}} t_{\mathrm{P}} \left\{ r_{\mathrm{cav}x}(\Phi_x) + r_{\mathrm{cav}y}(\Phi_y) \right\} \tag{4.34}$$

$$t_{\mathrm{com}-} = t_{\mathrm{BS}} r_{\mathrm{BS}} t_{\mathrm{P}} \left\{ r_{\mathrm{cav}x}(\Phi_x) - r_{\mathrm{cav}y}(\Phi_y) \right\}. \tag{4.35}$$

The compound mirror also transmits the input laser beam to the pick-off port. This transmissivity t_{comP} is

$$t_{\mathrm{comP}}(\theta_{\mathrm{op}}) = \frac{r_{\mathrm{P}}}{t_{\mathrm{P}}} r_{\mathrm{com}}. \tag{4.36}$$

Recycling cavity

The response of the recycling cavity is shown in Section 3.3.

$$g(\theta_{\mathrm{op}}) = \frac{E_{\mathrm{eff}}}{E_{\mathrm{inc}}} = \frac{t_{\mathrm{R}}}{1 - r_{\mathrm{R}} r_{\mathrm{com}}} \tag{4.37}$$

$$r_{\mathrm{rec}}(\theta_{\mathrm{op}}) = \frac{E_{\mathrm{ref}}}{E_{\mathrm{inc}}} = -r_{\mathrm{R}} + \frac{t_{\mathrm{R}}^2 r_{\mathrm{com}}}{1 - r_{\mathrm{R}} r_{\mathrm{com}}}, \tag{4.38}$$

where fields are defined in Fig. 3.8. The transmissivity of the recycling cavity to the detection port and the pick-off port are written as

$$t_{\mathrm{det}}(\theta_{\mathrm{op}}) = g t_{\mathrm{com}} \tag{4.39}$$

$$t_{\mathrm{pick}}(\theta_{\mathrm{op}}) = g t_{\mathrm{comP}} = g \frac{r_{\mathrm{P}}}{t_{\mathrm{P}}} r_{\mathrm{com}}. \tag{4.40}$$

4.2.3 Derivative of the response

The sensitivities of the signals are written by the derivatives of the response. Here, we describe the derivative of the response.

Phase derivatives

The partial derivatives by $\Phi_\pm$ and $\phi_\pm$ are written as

$$\frac{\partial}{\partial \Phi_-} = \frac{\partial \Phi_x}{\partial \Phi_-} \frac{\partial}{\partial \Phi_x} + \frac{\partial \Phi_y}{\partial \Phi_-} \frac{\partial}{\partial \Phi_y} = \frac{1}{2} \left(\frac{\partial}{\partial \Phi_x} - \frac{\partial}{\partial \Phi_y} \right) \tag{4.41}$$

$$\frac{\partial}{\partial \Phi_+} = \frac{\partial \Phi_x}{\partial \Phi_+} \frac{\partial}{\partial \Phi_x} + \frac{\partial \Phi_y}{\partial \Phi_+} \frac{\partial}{\partial \Phi_y} = \frac{1}{2} \left(\frac{\partial}{\partial \Phi_x} + \frac{\partial}{\partial \Phi_y} \right), \tag{4.42}$$

and

$$\frac{\partial}{\partial\phi_-} = \frac{1}{2}\left(\frac{\partial}{\partial\phi_x} - \frac{\partial}{\partial\phi_y}\right) \tag{4.43}$$

$$\frac{\partial}{\partial\phi_+} = \frac{1}{2}\left(\frac{\partial}{\partial\phi_x} + \frac{\partial}{\partial\phi_y}\right). \tag{4.44}$$

Fabry-Perot-Michelson interferometer

The derivation of the reflectivity of the Fabry-Perot cavity described in Eq. (3.19) by the round-trip phase Φ, we obtain

$$r'_{\rm cav}(\Phi) = \frac{\partial}{\partial\Phi} r_{\rm cav}(\Phi) = \frac{-{\rm i}t_{\rm F}^2 r_{\rm E} e^{-{\rm i}\Phi}}{(1 - r_{\rm F} r_{\rm E} e^{-{\rm i}\Phi})}.$$

By deriving the reflectivity of the compound mirror $r_{\rm com}$ written in Eq. (4.28) by Φ_+ or Φ_-, we obtain

$$\begin{aligned}\frac{\partial}{\partial\Phi_+} r_{\rm com} &= \frac{1}{2} t_{\rm P}^2 \left\{ t_{\rm BS}^2 r'_{{\rm cav}x}(\Phi_x) e^{-{\rm i}\phi_x} + r_{\rm BS}^2 r'_{{\rm cav}y}(\Phi_y) e^{-{\rm i}\phi_y} \right\} \\ &= \frac{1}{2} e^{-{\rm i}\frac{\phi_+}{2}} \left\{ r'_{{\rm com}+} \cos\left(\frac{\phi_-}{2}\right) - {\rm i} r'_{{\rm com}-} \sin\left(\frac{\phi_-}{2}\right) \right\} \qquad (4.45) \\ \frac{\partial}{\partial\Phi_-} r_{\rm com} &= \frac{1}{2} t_{\rm P}^2 \left\{ t_{\rm BS}^2 r'_{{\rm cav}x}(\Phi_x) e^{-{\rm i}\phi_x} - r_{\rm BS}^2 r'_{{\rm cav}y}(\Phi_y) e^{-{\rm i}\phi_y} \right\} \\ &= \frac{1}{2} e^{-{\rm i}\frac{\phi_+}{2}} \left\{ r'_{{\rm com}-} \cos\left(\frac{\phi_-}{2}\right) - {\rm i} r'_{{\rm com}+} \sin\left(\frac{\phi_-}{2}\right) \right\}. \qquad (4.46)\end{aligned}$$

Where $r'_{{\rm com}+}$ and $r'_{{\rm com}-}$ correspond to the common and differential component of two arms, defined by

$$r'_{{\rm com}+} = t_{\rm P}^2 \left\{ t_{\rm BS}^2 r'_{{\rm cav}x}(\Phi_x) + r_{\rm BS}^2 r'_{{\rm cav}y}(\Phi_y) \right\} \tag{4.47}$$

$$r'_{{\rm com}-} = t_{\rm P}^2 \left\{ t_{\rm BS}^2 r'_{{\rm cav}x}(\Phi_x) - r_{\rm BS}^2 r'_{{\rm cav}y}(\Phi_y) \right\}. \tag{4.48}$$

The derivatives by ϕ_+ or ϕ_- are written as

$$\frac{\partial}{\partial\phi_+} r_{\rm com} = -\frac{1}{2}{\rm i} e^{-{\rm i}\frac{\phi_+}{2}} \left\{ r_{{\rm com}+} \cos\left(\frac{\phi_-}{2}\right) - {\rm i} r_{{\rm com}-} \sin\left(\frac{\phi_-}{2}\right) \right\} \tag{4.49}$$

$$\frac{\partial}{\partial\phi_-} r_{\rm com} = -\frac{1}{2}{\rm i} e^{-{\rm i}\frac{\phi_+}{2}} \left\{ r_{{\rm com}-} \cos\left(\frac{\phi_-}{2}\right) - {\rm i} r_{{\rm com}+} \sin\left(\frac{\phi_-}{2}\right) \right\}, \tag{4.50}$$

where $r_{{\rm com}-}$ and $r_{{\rm com}+}$ are defined in Eqs. (4.31) and (4.32).

The derivatives of the transmissivity to the detection port $t_{\rm com}$ is calculated in the same way. Deriving Eq. (4.29) by Φ_+ or Φ_-, we obtain

$$\frac{\partial}{\partial\Phi_+}t_{\rm com} = \frac{1}{2}e^{-{\rm i}\frac{\phi_+}{2}}\left\{t'_{\rm com-}\cos\left(\frac{\phi_-}{2}\right) - {\rm i}t'_{\rm com+}\sin\left(\frac{\phi_-}{2}\right)\right\} \tag{4.51}$$

$$\frac{\partial}{\partial\Phi_-}t_{\rm com} = \frac{1}{2}e^{-{\rm i}\frac{\phi_+}{2}}\left\{t'_{\rm com+}\cos\left(\frac{\phi_-}{2}\right) - {\rm i}t'_{\rm com-}\sin\left(\frac{\phi_-}{2}\right)\right\}. \tag{4.52}$$

Where $t'_{\rm com+}$ and $t'_{\rm com-}$ correspond to the common and differential component of two arms:

$$t'_{\rm com+} = t_{\rm BS}r_{\rm BS}t_{\rm P}\left\{r'_{{\rm cav}x}(\Phi_x) + r'_{{\rm cav}y}(\Phi_y)\right\} \tag{4.53}$$

$$t'_{\rm com-} = t_{\rm BS}r_{\rm BS}t_{\rm P}\left\{r'_{{\rm cav}x}(\Phi_x) - r'_{{\rm cav}y}(\Phi_y)\right\}. \tag{4.54}$$

The derivatives by ϕ_+ or ϕ_- are

$$\frac{\partial}{\partial\phi_+}t_{\rm com} = -\frac{1}{2}{\rm i}e^{-{\rm i}\frac{\phi_+}{2}}\left\{t_{\rm com-}\cos\left(\frac{\phi_-}{2}\right) - {\rm i}t_{\rm com+}\sin\left(\frac{\phi_-}{2}\right)\right\} \tag{4.55}$$

$$\frac{\partial}{\partial\phi_-}t_{\rm com} = -\frac{1}{2}{\rm i}e^{-{\rm i}\frac{\phi_+}{2}}\left\{t_{\rm com+}\cos\left(\frac{\phi_-}{2}\right) - {\rm i}t_{\rm com-}\sin\left(\frac{\phi_-}{2}\right)\right\}. \tag{4.56}$$

If both arms are completely symmetric, $r'_{\rm com-} = t'_{\rm com-} = 0$.

Recycling cavity

The derivative expressions for the recycling cavity (the whole interferometer) are written as functions of the derivatives of the compound mirror and so on. From Eq. (4.37), the derivative of the gain of the recycling cavity is written as

$$\frac{\partial}{\partial\theta}g = \frac{t_{\rm R}r_{\rm R}}{(1-r_{\rm R}r_{\rm com})^2}\frac{\partial r_{\rm com}}{\partial\theta} = \frac{r_{\rm R}}{t_{\rm R}}g^2\frac{\partial r_{\rm com}}{\partial\theta}, \tag{4.57}$$

where θ represents Φ_+, Φ_-, ϕ_+, or ϕ_-. The derivatives of the reflectivity and transmissivities of the recycling cavity is calculated from Eqs. (4.38), (4.39), and (4.40), as

$$\frac{\partial}{\partial\theta}r_{\rm rec} = \frac{t_{\rm R}^2}{(1-r_{\rm R}r_{\rm com})^2}\frac{\partial r_{\rm com}}{\partial\theta} = g^2\frac{\partial r_{\rm com}}{\partial\theta} \tag{4.58}$$

$$\frac{\partial}{\partial\theta}t_{\rm det} = \frac{r_{\rm R}}{t_{\rm R}}g^2\frac{\partial r_{\rm com}}{\partial\theta}t_{\rm com} + g\frac{\partial t_{\rm com}}{\partial\theta} \tag{4.59}$$

$$\frac{\partial}{\partial\theta}t_{\rm pick} = \frac{r_{\rm P}}{t_{\rm P}t_{\rm R}}g^2\frac{\partial r_{\rm com}}{\partial\theta} \tag{4.60}$$

Displacement and frequency sensitivities

In order to estimate the displacement sensitivity ([V/m]) or frequency sensitivity ([V/Hz]) of the signals, it is necessary to convert the phase sensitivity ([V/rad]) of the signals with coefficients.

The round-trip phase θ (Φ_+, Φ_-, ϕ_+, and ϕ_-) is written as

$$\theta = \frac{2X\Omega_\mathrm{l}}{c},$$

where X represents the corresponding length (L_+, L_-, l_+, and l_-). Thus, to convert the phase sensitivity to displacement sensitivity, we should multiply

$$\frac{\partial\theta}{\partial X} = \frac{2\Omega_\mathrm{l}}{c} = \frac{4\pi}{\lambda_\mathrm{l}} \quad [\mathrm{rad/m}], \tag{4.61}$$

where λ_l is the wavelength of the laser beam[15].

On the other hand, in order to convert the phase sensitivity to the frequency sensitivity, we should use the coefficient

$$\frac{\partial\theta}{\partial\nu_\mathrm{l}} = \frac{4\pi X}{c} \quad [\mathrm{rad/Hz}], \tag{4.62}$$

where $\nu_\mathrm{l} = \Omega_\mathrm{l}/2\pi$ is the frequency of the laser beam.

4.3 Sensitivities of the signals under operational conditions

In this section, we calculate the sensitivities of the signals to the motions of the interferometer. In order to simplify the calculation, we assume that the interferometer is ideal[16] and the it is operated at the best operational point.

[15]Exactly, the wavelength of the sidebands are different from that of the carrier. However, since this difference is small enough comparing to the wavelength of the carrier, we can neglect this difference.

[16]We assume the following idealizations. (1) The optical parameters of the two arm cavities are equal:

$$r_{\mathrm{cav}\,x}(\Phi) = r_{\mathrm{cav}\,y}(\Phi).$$

(2) The reflectivity and transmissivity of the beamsplitter is equal, and the beamsplitter has no losses:

$$r_\mathrm{BS} = t_\mathrm{BS} = \sqrt{2}.$$

(3) Neglect the effect of the loss in the substrates and AR surface of the optical components.

4.3.1 Operational point

The operational point of an interferometric gravitational wave detector is selected to realize the highest sensitivity. Thus, the operational point of a power-recycled Fabry-Perot-Michelson interferometer is usually locked and operated under the following conditions.

Arm cavities

Both arm cavities are set to resonate with the incident laser beam because the phase of the reflected beam from a Fabry-Perot cavity is most sensitive to gravitational waves. The resonant conditions of the arm cavities with the incident laser beam (the carrier) are written as

$$\Phi_{x0} = 0 + 2\pi n_1 \quad (n_1 : \text{integer}) \tag{4.63}$$

$$\Phi_{y0} = 0 + 2\pi n_2 \quad (n_2 : \text{integer}), \tag{4.64}$$

where the subscript '$_0$' denotes the operational conditions for the carrier.

Interference fringe

The detection port of the interferometer has to be a dark fringe. The signal-to-shot-noise ratio is maximized when the interference fringe is dark at the detection port: $t_{\text{det}0} = 0$. From Eqs. (4.33) and (4.39), this condition is written as

$$\phi_{-0} = 0 + 2\pi n_3 \quad (n_3 : \text{integer}). \tag{4.65}$$

The dark-fringe condition at the Michelson interferometer is indispensable for power recycling as well as for the improvement of the shot-noise level.

Recycling cavity

The recycling cavity has to be resonate with the incident laser beam to obtain maximum enhancement of the laser power in the interferometer. From Eq. (4.37), this condition is satisfied when $r_{\text{com}0} = 1$. Thus, ϕ_+ has to satisfy the condition:

$$\phi_{+0} = \phi_{-0} + 4\pi n_4 \quad (n_4 : \text{integer}). \tag{4.66}$$

From the Eqs. (4.63) to (4.66), the best operational point of the interferometer is described as

$$\Phi_{x0} = \Phi_{y0} = \phi_{-0} = \phi_{+0} = 0. \tag{4.67}$$

4.3.2 Conditions for the sidebands

In addition to the operational conditions for the carrier, we put a few conditions on the modulation frequency and the length of the recycling cavity.

Phases of the sidebands

Since the carrier and sidebands have different frequencies, the round-trip phases are different in each beam. The angular frequency of the carrier is the same as that of the laser source ($\Omega_{\rm l}$). Thus, we get the equations

$$\Phi_{\rm dof0} = \frac{2L_{\rm dof}\Omega_{\rm l}}{c} \tag{4.68}$$

$$\phi_{\rm dof0} = \frac{2l_{\rm dof}\Omega_{\rm l}}{c}, \tag{4.69}$$

where index '$_{\rm dof}$' represents '$_x$', '$_y$', '$_+$', and '$_-$'. Since the angular frequency of the n-th order sideband is $\Omega_{\rm l} + n\omega_{\rm m}$, we get the following equations:

$$\Phi_{{\rm dof}\,n} = \frac{2L_{\rm dof}(\Omega_{\rm l} + n\omega_{\rm m})}{c} = \Phi_{\rm dof0} + \frac{2nL_{\rm dof}\omega_{\rm m}}{c} \tag{4.70}$$

$$\phi_{{\rm dof}\,n} = \frac{2l_{\rm dof}(\Omega_{\rm l} + n\omega_{\rm m})}{c} = \phi_{\rm dof0} + \frac{2nl_{\rm dof}\omega_{\rm m}}{c}. \tag{4.71}$$

Here, defining the parameters α and β by

$$\alpha = \frac{l_-\omega_{\rm m}}{c} \tag{4.72}$$

$$\beta = \frac{l_+\omega_{\rm m}}{c}, \tag{4.73}$$

we get the equation

$$\phi_{-n} = \phi_{-0} + 2n\alpha \tag{4.74}$$

$$\phi_{+n} = \phi_{+0} + 2n\beta. \tag{4.75}$$

Modulation frequency

The sidebands do not resonate with the arm cavity. The modulation frequency is selected so that the first-order sidebands are near antiresonant with the arm cavities:

$$\Phi_{x1} = \frac{2L_x\omega_{\rm m}}{c} \simeq \pi + 2\pi n_5 \quad (n_5 : \text{integer}) \tag{4.76}$$

$$\Phi_{y1} = \frac{2L_y\omega_{\rm m}}{c} \simeq \pi + 2\pi n_6 \quad (n_6 : \text{integer}) \tag{4.77}$$

The first-order sidebands are slightly shifted from the antiresonant condition so that the even-order sideband should not resonate with the arm cavities. When the finesse of the arm cavities is high enough, it is a good approximation to assume all of the sidebands are antiresonant with the arm cavities.

Length of the recycling cavity

The first-order sidebands resonate with the recycling cavity. It is necessary to leak the first-order sidebands to the detection port effectively, in order to increase the sensitivity to gravitational waves. This condition is written as $r_{\rm com\pm1} = 1$, same as the resonant condition for the carrier. Considering that the the sign of the sidebands flips on the reflection with the arm cavities, we get the equation

$$\beta = \pi + 2\pi n_7 \quad (n_7 : \text{integer}). \tag{4.78}$$

From this equation, the length of the recycling cavity ($l_+/2$) is determined depending on the modulation frequency:

$$\frac{l_+}{2} = \frac{c}{2\nu_{\rm m}}\left(\frac{1}{2} + n_7\right), \tag{4.79}$$

where $\nu_{\rm m} = \omega_{\rm m}/2\pi$ is the modulation frequency. The smallest modulation frequency which satisfies the resonant condition is half of the FSR of the recycling cavity. In practice, the length of the recycling cavity is slightly shifted from the value obtained from Eq. (4.79), because the phase change in the sidebands by the arm cavities is not exactly π.

When the modulation frequency is slightly shifted from the antisymmetric condition of the the arm cavity, the higher-order sidebands ($|n| \geq 2$) can be considered not to resonate with the recycling cavity, as well as the arm cavity.

4.3.3 Response of the interferometer at the operational point

Here, we show the expressions for the statistic response of the interferometer substituting the operational conditions. In the calculation, we assume some idealization: the two arm cavities are identical, the beamsplitter divides the input beam equally without any losses, and the interferometer is kept exactly at its operational point. In addition, we neglect the effect of higher order ($|n| \geq 2$) sidebands.

Since the carrier beam is resonant with the arm cavities, the amplitude reflectivity of a Fabry-Perot cavity for the carrier is written as

$$r_{\mathrm{cav}0} = r_{\mathrm{reso}} = -r_{\mathrm{F}} + \frac{t_{\mathrm{F}}^2 r_{\mathrm{E}}}{1 - r_{\mathrm{F}} r_{\mathrm{E}}}. \tag{4.80}$$

Since the sidebands are considered to be antiresonant with the arm cavities, the reflectivity of the cavity for sidebands is written as

$$r_{\mathrm{cav}\pm1} \simeq r_{\mathrm{anti}} = -r_{\mathrm{F}} - \frac{t_{\mathrm{F}}^2 r_{\mathrm{E}}}{1 + r_{\mathrm{F}} r_{\mathrm{E}}} \ . \tag{4.81}$$

Differentiating the reflectivity of a Fabry-Perot cavity by the round-trip phase, and substituting the operational conditions, we obtain

$$r'_{\mathrm{cav}0} = r'_{\mathrm{reso}} = \frac{-\mathrm{i} t_{\mathrm{F}}^2 r_{\mathrm{E}}}{(1 - r_{\mathrm{F}} r_{\mathrm{E}})^2} \tag{4.82}$$

$$r'_{\mathrm{cav}\pm1} \simeq r'_{\mathrm{anti}} = \frac{\mathrm{i} t_{\mathrm{F}}^2 r_{\mathrm{E}}}{(1 + r_{\mathrm{F}} r_{\mathrm{E}})^2} \ , \tag{4.83}$$

for the carrier and the sidebands, respectively.

The reflected beams by the arm cavities are recombined on the beamsplitter. Considering the dark-fringe condition and the resonance condition of the recycling cavity, we obtain the following equations for the reflectivity of the whole interferometer for the carrier and the sidebands:

$$r_{\mathrm{rec}0} = -r_{\mathrm{R}} + \frac{t_{\mathrm{R}}^2 t_{\mathrm{P}}^2 r_{\mathrm{reso}}}{1 - r_{\mathrm{R}} t_{\mathrm{P}}^2 r_{\mathrm{reso}}} \tag{4.84}$$

$$r_{\mathrm{rec}1} = -r_{\mathrm{R}} - \frac{t_{\mathrm{R}}^2 t_{\mathrm{P}}^2 r_{\mathrm{anti}} \cos\alpha}{1 + r_{\mathrm{R}} t_{\mathrm{P}}^2 r_{\mathrm{anti}} \cos\alpha} \ . \tag{4.85}$$

Table 4.2: Table of the sensitivities of the signals to the deviations in the differential (upper block) and common (lower block) degrees of freedom. The common factors, such as the laser power and demodulation gain, are not displayed.

Signal sensitivities		
	$\delta\Phi_-$	$\delta\phi_-$
$\delta V_{\rm DQ}$	$g_0 g_1 \lvert r'_{\rm reso}\rvert r_{\rm anti} \sin\alpha$	$g_0 g_1 r_{\rm reso} r_{\rm anti} \sin\alpha$
$\delta V_{\rm RQ}$	$g_1^2 r_{\rm rec0} \lvert r'_{\rm anti}\rvert \sin\alpha$	$-g_1^2 r_{\rm rec0} r_{\rm anti} \sin\alpha$
	$\delta\Phi_+$	$\delta\phi_+$
$\delta V_{\rm PI}$	$g_0 g_1 \dfrac{r_{\rm P}^2}{t_{\rm R}} \left(g_0 \lvert r'_{\rm reso}\rvert r_{\rm anti} + g_1 r_{\rm reso} \lvert r'_{\rm anti}\rvert\right) \cos\alpha$	$g_0 g_1 \dfrac{r_{\rm P}^2}{t_{\rm R}} (g_0 - g_1) r_{\rm reso} r_{\rm anti} \cos\alpha$
$\delta V_{\rm RI}$	$-g_0^2 \lvert r'_{\rm reso}\rvert r_{\rm rec1} + g_1^2 r_{\rm rec0} \lvert r'_{\rm anti}\rvert \cos\alpha$	$-g_0^2 r_{\rm reso} r_{\rm rec1} - g_1^2 r_{\rm rec0} r_{\rm anti} \cos\alpha$

Compared with the non-recycling case, the amplitude of the field inside the recycling cavity is enhanced by the factor g:

$$g_0 = \frac{t_{\rm R}}{1 - r_{\rm R} t_{\rm P}^2 r_{\rm reso}} \tag{4.86}$$

$$g_1 = \frac{t_{\rm R}}{1 + r_{\rm R} t_{\rm P}^2 r_{\rm anti} \cos\alpha} \ , \tag{4.87}$$

for the carrier and the sidebands, respectively. The recycling gain is defined as the power enhancement for the carrier: $G_0 = g_0^2$.

4.3.4 Signals extracted using frontal modulation

The calculated sensitivities of the signals ($V_{\rm DQ}$, $V_{\rm RQ}$, $V_{\rm PI}$, and $V_{\rm RI}$) to the deviations in four degrees of freedom ($\delta\Phi_-$, $\delta\Phi_+$, $\delta\phi_-$, and $\delta\phi_+$) are summarized in Table 4.2. Here, $V_{\rm DQ}$ and $V_{\rm RQ}$ are not sensitive to $\delta\Phi_+$ nor $\delta\phi_+$. $V_{\rm DQ}$ and $V_{\rm RQ}$ are not sensitive to $\delta\Phi_-$ nor $\delta\phi_-$.

Conventional selection of optical parameters

Here, we show the conventional selection of optical parameters for a power-recycled Fabry-Perot-Michelson interferometer with the frontal modulation tech-

nique [19], and estimate of the sensitivities of the signals approximately from Table 4.2.

The reflectivity of the end mirrors is set high so as to realize a high recycling gain. The reflectivity of the front mirrors is selected to be slightly less than that of the end mirror, optimizing the frequency response of the arm cavities to the target gravitational waves. In this case, we can approximate that $r_{\rm reso}$ is slightly less than unity, $r_{\rm anti} \simeq -1$ and $|r'_{\rm reso}| \gg 1 \gg |r'_{\rm anti}|$. The reflectivity of the recycling mirror is selected so as to realize a high recycling gain. From Eq. (3.68), we can show that the recycling gain is maximized when

$$r_{\rm R} = r_{\rm com0} = t_{\rm P}^2 r_{\rm reso}. \tag{4.88}$$

Neglecting the loss in the recycling mirror, the condition expressed by Eq. (4.88) is also written as

$$r_{\rm rec0} = 0. \tag{4.89}$$

In practice, however, $r_{\rm R}$ is set to slightly less than $r_{\rm com0}$ for insurance against a decrease in $r_{\rm reso}$ due to contamination of the mirrors. The parameter α is selected to be small so that the reflectivity of the compound mirror for the sidebands ($r_{\rm com1} = -t_{\rm P}^2 r_{\rm anti} \cos\alpha$) is larger than $r_{\rm com0}$ in order to avoid a gain constraint on the control system [19]. Normally, the amplitude gains (g_0 and g_1) have almost the same-order values. The reflectivity of the whole interferometer for the carrier ($r_{\rm rec0}$) and for the sidebands ($r_{\rm rec1}$) also takes the same-order value. The reflectivity of the pick-off mirror is determined considering the recycling gain and the signal-to-noise ratio of the signal extracted from the pick-off port.

Estimation of signal sensitivity

The sensitivities of the signals are estimated from Table 4.2 with the approximated parameters.

The $V_{\rm DQ}$ signal is more sensitive to a $\delta\Phi_-$ deviation than to δl_- by the phase-change enhancement factor of the Fabry-Perot arm cavity, i.e., by the effective bounce number of the cavity, $N_{\rm cav}$. On the other hand, the $V_{\rm RQ}$ signal is more sensitive to a $\delta\phi_-$ deviation than to $\delta\Phi_-$. Thus, the signals for differential deviations of the interferometer are well-separated: the sensitivity matrix is almost diagonal.

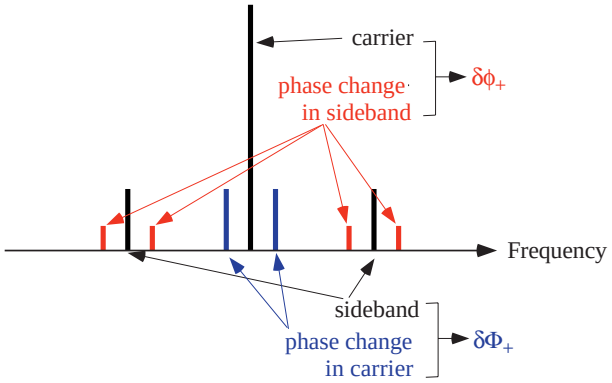

Figure 4.6: The amplitude of the laser beam output from the interferometer. The carrier and sidebands experience amplitude and phase change in the interferometer; the phase changes caused in the interferometer are shown as phase-modulated sidebands (audio sidebands) in this Figure. The phase change in the carrier mainly contains the enhanced $\delta\Phi_+$ information. On the other hand, the phase change in the first-order sidebands mainly contains the $\delta\phi_+$ information,

As for the common deviation, however, the sensitivity matrix is far from diagonal. Since $|r'_{\rm reso}| \gg 1 \gg |r'_{\rm anti}|$, the sensitivity values are dominated by the first terms in the $\delta\Phi_+$ column of Table 4.2. In the $\delta\phi_+$ column, the sensitivity values are subtraction of almost the same-order terms. Thus, both $V_{\rm PI}$ and $V_{\rm RI}$ are much more sensitive to the $\delta\Phi_+$ deviation than to $\delta\phi_+$. These poorly separated signals complicate the design of the control system.

4.4 Signal-separation method

The $V_{\rm PI}$ and $V_{\rm RI}$ signals are more sensitive to $\delta\Phi_+$ than to $\delta\phi_+$ with the conventional selection of the optical parameters. However, by selecting the optical parameters properly, we can make the $V_{\rm RI}$ signal sensitive only to the $\delta\phi_+$ deviation. In this Section, we describe a new signal separation scheme by adjusting the optical parameters.

4.4.1 Signal mixing problem

Here, we review the signal mixing problem in a power-recycled interferometer from different viewpoint.

The signal mixing originates in the mixing of the phase change of the laser beam. The deviations of the interferometer from the operational point cause phase changes in the laser beam (Figure 4.6), which are detected as signals with modulation scheme. As described in Eqs. (4.19) and (4.20), the error signals extracted by demodulation at the modulation frequency mainly contain the information of the phase of the carrier and first-order sidebands (x_0 and $x_{\pm 1}$). Thus, the signal sensitivities are mainly contributed by two terms: the product of the sidebands with the phase change in the carrier, and the product of the carrier with the phase change in the sidebands.

With respect to the common motion of the interferometer ($\delta\Phi_+$ and $\delta\phi_+$), the phase change in the carrier mainly contains the enhanced $\delta\Phi_+$ information and little information about the motion in the recycling cavity. This is because the carrier beam is resonant with the arm cavities and quite sensitive to their phase changes. On the other hand, the phase change in the first-order sidebands mainly contains the $\delta\phi_+$ information, because the sideband beams are not resonant with the arm cavities but resonant with the recycling cavity. The phase of the sidebands are not effected by the arm cavity motion and sensitive to the recycling cavity motion.

Both in the carrier and the sidebands, the phase change information (contained in the audio sidebands) leak to the bright fringe at interference, i.e., to the pick-off port and reflection port. In addition, the contribution from the phase changes in the carrier and the sidebands appear in the same demodulation phase (in-phase). Thus, the error signals for the common motion of the interferometer (V_{PI} and V_{RI}) are much more sensitive to $\delta\Phi_+$ than to $\delta\phi_+$.

4.4.2 Sideband elimination

As described above, the signals are comprised of two terms: the product of the sidebands and the phase change in the carrier, and the product of the carrier and the phase change in the sidebands. Thus, if the sidebands are absent and the

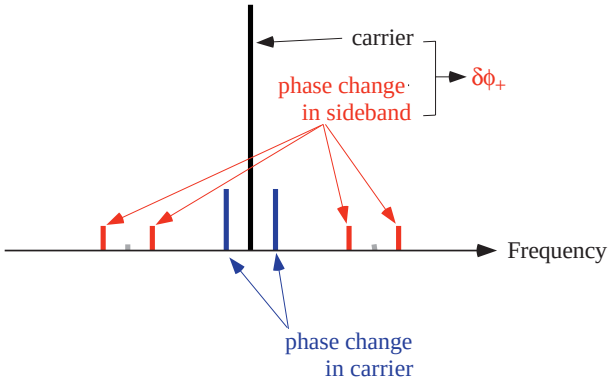

Figure 4.7: The amplitude of the laser beam output from the interferometer with sideband elimination. The signal is only sensitive to the $\delta\phi_+$ deviation.

carrier is present in the beam incident on a photo detector, the signal contains only information about the recycling cavity motion (Figure 4.7). This is the essence of our signal-separation method.

It is possible to realize this condition at the reflection port, from which the $V_{\rm RI}$ signal is extracted. This condition is written by the reflectivity of the interferometer to the reflection port ($r_{\rm rec}$) as

$$r_{\rm rec1} = 0 \tag{4.90}$$

for the sidebands, and

$$r_{\rm rec0} \neq 0 \tag{4.91}$$

for the carrier.

4.4.3 Adjustment of the optical parameters

From Eq. (4.38), Eq. (4.90) is also written as

$$r_{\rm R} = -t_{\rm P}^2 r_{\rm anti} \cos\alpha = r_{\rm com1}. \tag{4.92}$$

This equation shows that the reflectivity of the compound mirror for sidebands is equal to that of the recycling mirror. In other words, the gain of the sidebands is maximized.

Table 4.3: Main parameters of a model interferometer used in the calculation. The parameters in parentheses represent the conventionally selected parameters.

Parameters of a model interferometer		
Parameter	Symbol	Value
Power of the laser source	$P_{\rm l}$	10 W
Wavelength of the laser beam	$\lambda_{\rm l}$	1064 nm
Length of the arm cavities	L_x, L_y	3 km
Reflectivity of the front mirrors	$R_{\rm F}$	97.00 %
Reflectivity of the end mirrors	$R_{\rm E}$	99.99 %
Modulation frequency	$\omega_{\rm m}/2\pi$	15 MHz
Length of the recycling cavity	$l_+/2$	5 m
Asymmetry	l_-	75 (50) cm
Reflectivity of the recycling mirror	$R_{\rm R}$	92.33 (94.00) %
Reflectivity of the pick-off mirror	$R_{\rm P}$	0.5 %
Loss in an optical component		100 ppm
Reflectivity of an AR coat		0.1 %
Contrast		99 %

Since the first terms in the $V_{\rm RI}$ row of Table 4.2 vanish under this condition, the $V_{\rm RI}$ signal almost becomes insensitive to $\delta\Phi_+$, and sensitive to $\delta\phi_+$. In fact, because of the small phase change in the sidebands caused by the arm cavity motion, there is a residual sensitivity represented by the second term in $\partial V_{\rm RI}/\partial\Phi_+$. However, the residual sensitivity of the $V_{\rm RI}$ signal to $\delta\Phi_+$ is much smaller than that to $\delta\phi_+$. Moreover, it is possible to cancel $\partial V_{\rm RI}/\partial\Phi_+$ by a slight shift of the reflectivity of the recycling mirror.

Since the recycling gain is maximized when $r_{\rm rec0} = 0$, the condition expressed in Eq. (4.91) implies a decrease in the recycling gain. The decrease depends on the difference between $r_{\rm com0}$ and $r_{\rm com1}$.

Table 4.4: Sensitivities of the signals in the deviation in the four degrees of freedom (extracted by the conventional frontal modulation technique).

Signal sensitivities (without signal separation)				
	$\delta\Phi_-$	$\delta\phi_-$	$\delta\Phi_+$	$\delta\phi_+$
V_{DQ}	1	7.6×10^{-3}	0	0
V_{RQ}	7.6×10^{-3}	1	0	0
V_{PI}	0	0	1	1.1×10^{-4}
V_{RI}	0	0	**1**	$\mathbf{8.0 \times 10^{-4}}$

4.4.4 Calculation of the signals in a model interferometer

In order to evaluate our signal-separation method, we prepared a model interferometric gravitational wave detector and calculated the sensitivities of the extracted signals. The parameters of the model interferometer are shown in Table 4.3. The parameters in the parentheses represent the conventionally selected parameters. In this numerical calculation, the effect of losses in the optical parameters and contrast defect were considered.

Without signal separation

At first, we calculated the sensitivities of the signals extracted by the conventional frontal modulation technique. The reflectivity of the recycling mirror ($R_{\mathrm{R}} = 0.9400$) is slightly less than that of the compound mirror for the carrier ($R_{\mathrm{com0}} = 0.9513$). The asymmetry ($l_- = 50$ cm) is selected so as to avoid any gain constraint. Table 4.4 gives the sensitivity matrix of the model interferometer. The values in the matrix are normalized so that the largest sensitivity value in each row is equal to unity. Though the signals corresponding to the deviations in the four degrees of freedom are extracted, both the V_{PI} and V_{RI} signals are more sensitive to $\delta\Phi_+$ than to $\delta\phi_+$. The calculated recycling gain is 20.2.

With signal separation

Next, we calculated the sensitivities of the signals by our method. In this calculation, the asymmetry was 75 cm, and thus, the reflectivity of the recycling

Table 4.5: Sensitivities of the signals to the deviations in the four degrees of freedom (extracted by modified frontal modulation technique).

Signal sensitivities (with signal separation)				
	$\delta\Phi_-$	$\delta\phi_-$	$\delta\Phi_+$	$\delta\phi_+$
$V_{\rm DQ}$	1	7.6×10^{-3}	0	0
$V_{\rm RQ}$	7.6×10^{-3}	1	0	0
$V_{\rm PI}$	0	0	1	1.3×10^{-3}
$V_{\rm RI}$	0	0	$\mathbf{7.8 \times 10^{-3}}$	**1**

mirror became 92.33% from Eq. (4.92). Table 4.5 is the sensitivity matrix of the extracted signals with these parameters. The diagonal values are the main signals necessary for controlling the interferometer, while the off-diagonal values represent the mixing of unnecessary signals. The $V_{\rm DQ}$, $V_{\rm RQ}$, $V_{\rm PI}$, and $V_{\rm RI}$ signals are most sensitive to the deviations $\delta\Phi_-$, $\delta\phi_-$, $\delta\Phi_+$, and $\delta\phi_+$, respectively. The off-diagonal terms in the sensitivity matrix are less than 1 % of the diagonal terms. The calculated recycling gain is 19.4; this is 96% of the value when the reflectivity of the recycling mirror is set to maximize it. The shot-noise level of $V_{\rm DQ}$ signal for δL_- is 5.3×10^{-20} m/$\sqrt{\rm Hz}$, which corresponds to a strain sensitivity of 1.8×10^{-23} /$\sqrt{\rm Hz}$ for the gravitational wave signal.

4.4.5 Requirements for signal separation

Reflectivity matching

Our power recycling scheme differs from the conventional one in only one point; the condition $r_{\rm rec1} = 0$, Eq. (4.90), is required in place of $r_{\rm rec0} = 0$, Eq. (4.89). The sensitivity matrix is diagonalized remarkably well if Eq. (4.90) is satisfied. However, it is difficult to realize this condition exactly because a high accuracy is required for the reflectivity of the recycling mirror. Figure 4.8 shows the required accuracy as a function of the reflectivity of the recycling mirror when the sensitivity of the $V_{\rm RI}$ signal to $\delta\Phi_+$ is required to be less than 10% of that to $\delta\phi_+$ in the model interferometer. The reflectivity of the recycling mirror is changed together with the asymmetry under the condition represented by Eq. (4.92). The

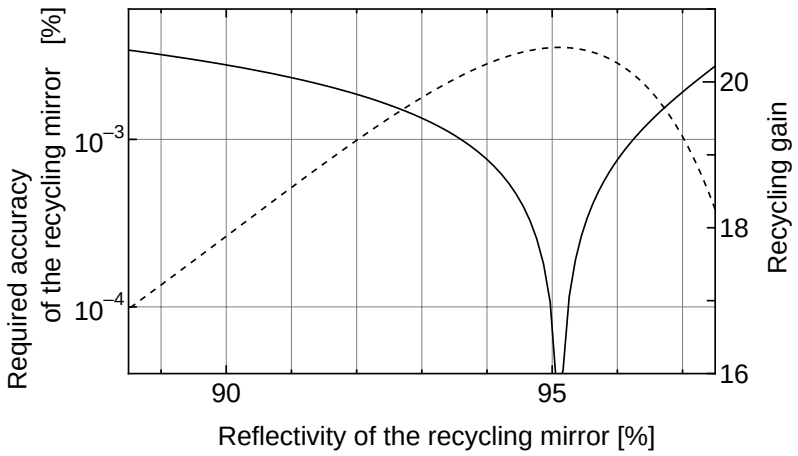

Figure 4.8: Required accuracy for the reflectivity of the recycling mirror (solid line), and the recycling gain (broken line) as functions of the reflectivity of the recycling mirror.

recycling gain as a function of the reflectivity of the recycling mirror is shown together. If $r_{\mathrm{com}\ 0}$ and r_{R} have close values ($R_{\mathrm{R}} \simeq R_{\mathrm{com0}} = 0.9513$), which result in a high recycling gain, the accuracy requirement for the reflectivity of the recycling mirror becomes more severe. Thus, the difference between R_{com0} and R_{R} ($= R_{\mathrm{com1}}$) must be determined considering the possible accuracy, the long-term stability of these parameters, and the required recycling gain.

In the case that the reflectivity of the recycling mirror is 92.33%, the reflectivity error of the recycling mirror has to be less than 2×10^{-3}% (20 ppm). Since it is difficult to produce a mirror with such an accuracy in practice, it is necessary to adjust other optical parameters so as to satisfy Eq. (4.92) after producing the recycling mirror. The parameter α is a function of the asymmetry and modulation frequency, defined by Eq. (4.72). The reflectivity error of 2×10^{-3} % corresponds to an asymmetry error of about 0.1 mm. It is possible to adjust the asymmetry to an accuracy of 0.1 mm by using motorized stages.

In the experiments on the 3-m prototype interferometer, the coupling of the recycling cavity is optimized using a pick-off mirror. The reflectivity of the compound mirror is adjusted by changing the transmissivity of the pick-off mirror (Chapter 5, Chapter 6).

Fluctuation of the reflectivity

In addition to the initial deviation from the optimal coupling described above, the fluctuation of the interferometer can cause the signal mixing. The reflectivity of the compound mirror fluctuates because the fluctuation of the interferometer is suppressed only with finite control gains.

The fluctuation of the arm cavity length (δL_-, δL_+) cause a very small effect on the reflectivity change of the compound mirror for the sidebands because sidebands are almost antiresonant with the arm cavity. However, the fluctuation of interference fringe (δl_-) changes the reflectivity of the compound mirror. To keep the reflectivity fluctuation less than $2 \times 10^{-3}\%$, the residual RMS deviation from the operational point should be less than 5×10^{-10} m. This value is about the same order as that required from rejection of intensity noise level in the interferometer.

The fluctuation of mirror orientation also changes the reflectivity of the compound mirror because of imperfect interference on the beamsplitter. To keep the reflectivity fluctuation less than $2 \times 10^{-3}\%$, the RMS deviation of the mirror orientation should be less than 8×10^{-8} rad in the model interferometer [71].

Effects of the higher-order sidebands

In the calculation of signal sensitivity (Section 4.3), we neglected the effect of the higher-order sidebands. However, the higher-order sidebands can extinguish the δl_+ signal under the signal-separation condition.

In the reflection port, the effect of second-order sidebands are relatively enhanced. The reflectivity of the interferometer to the reflection port is small for the carrier and the first-order sidebands because the carrier and the first-order sidebands are resonant with the recycling cavity. On the other hand, since the second-order sidebands are antiresonant with the recycling cavity, almost all power of the second-order sidebands is reflected back to the reflection port. The second-order sidebands produce the δl_+ signals coupling with the phase change in the first-order sidebands, which can cancel out the δl_+ signal in the error signal without proper selection of the optical parameters.

Adjustment of recycling cavity length

The length of the recycling cavity is determined so that the first-order sidebands as well as the carrier are resonant with the recycling cavity. Here, if the recycling cavity length is not set properly, the sidebands cannot be rejected from the reflection port. The misadjustment of the recycling cavity length and the modulation frequency cause a mixing of δL_+ signal to the reflection port signals (δl_-, δl_+), and excess intensity noise coupling with the frequency noise.

Putting the same requirement for the residual sidebands at the reflection port as the above requirements, the recycling cavity length error has to be less than 2×10^{-5} m. This length error corresponds to the modulation frequency error of 50 Hz.

Chapter 5

3-m Fabry-Perot-Michelson interferometer

In this Chapter, we describe the experimental setup of a 3-m prototype interferometer placed at the University of Tokyo (Fig. 5.1, Table 5.1, Table 5.2). This is a Fabry-Perot-Michelson interferometer with power recycling. The arm cavities have a length of 3 m and a finesse of about 240. The pick-off in the recycling cavity is comprised of a quarter-wave plate and two polarizers. This pick-off is used to adjust the reflectivity of the compound mirror to realize the signal separation scheme described in Section 4.4.

- **Optical design.** We describe the specifications of main optics (the mirrors, the beamsplitter, and the pick-off) and the optical design of the interferometer in Section 5.1.

- **Suspension system.** The mirrors and the beamsplitter are suspended as double pendulums. The upper mass of the double pendulum is dumped by eddy current with permanent magnets placed around it. The positions of suspended optics are controlled with coil-magnet actuators. Motorized stages and coil-magnet actuators are used to adjust the orientation of these suspended optics.

- **Laser.** An LD-pumped Nd:YAG laser with the wavelength of 1064 nm and the output power of 50 mW is used as a laser source. The laser source is

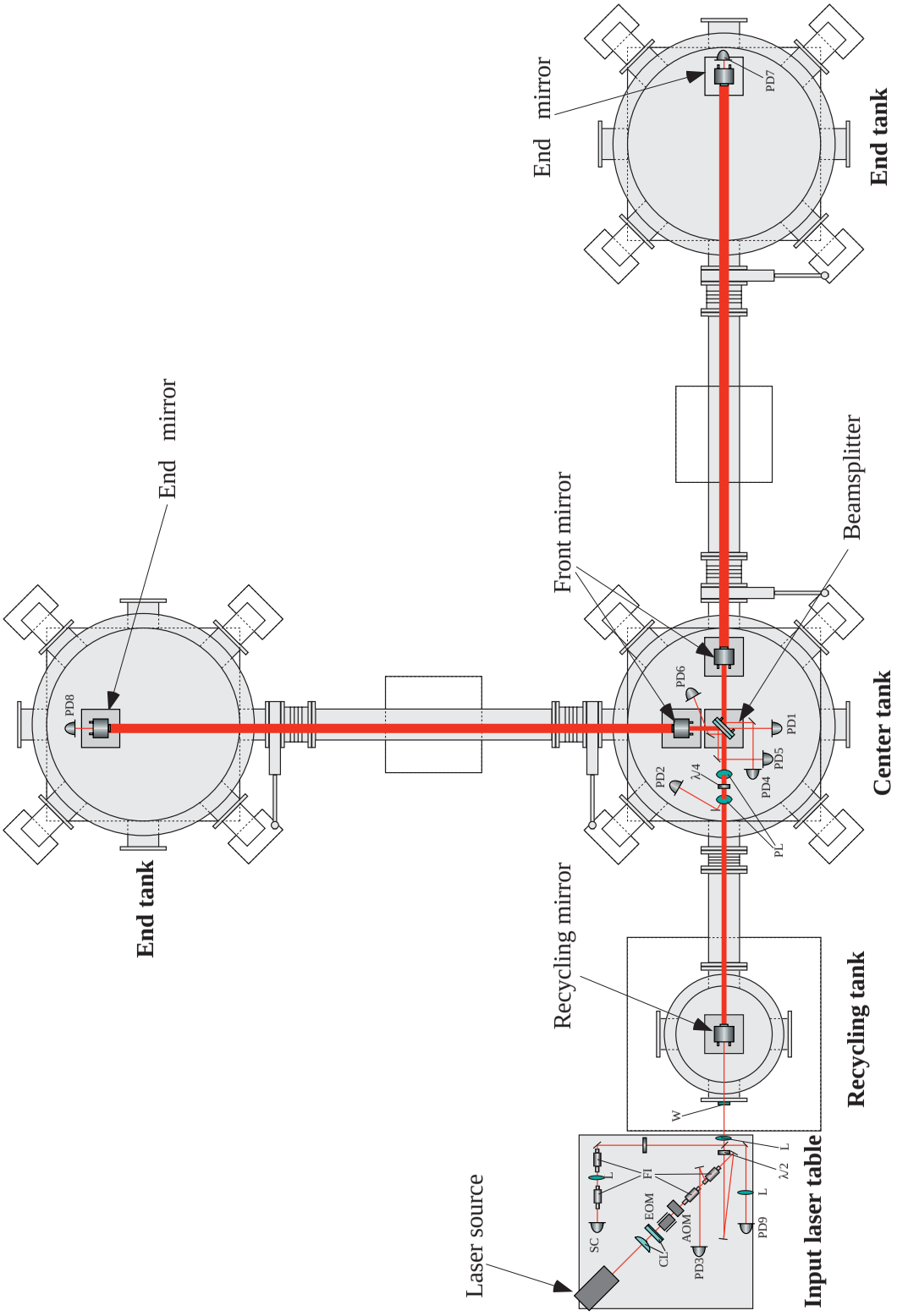

Figure 5.1: Experimental setup of 3m Fabry-Perot-Michelson interferometer.

Table 5.1: Main features of the 3-m prototype interferometer.

Features of the 3-m prototype interferometer	
Interferometer type	Fabry-Perot-Michelson interferometer with power recycling
Laser source	LD-pumped Nd:YAG laser (1064 nm)
Suspension system	Double pendulum damped by eddy current
Signal extraction	Frontal modulation with the signal separation scheme
Vacuum system	Four tanks connected with vacuum tubes evacuated with a scroll pump

placed on an input table. The laser beam is introduced to the interferometer after passing through lenses for mode matching, an EOM for phase modulation, an AOM for intensity modulation, and Faraday isolators.

- **Signal-extraction and control system.** The interferometer is kept at the operational point by controlling the lengths between the mirrors. The control signals are extracted with the signal-separation scheme described in Chapter 4; the modulation, demodulation and control system is shown in Section 5.4. The photo detectors for the control of the interferometer are placed in the center tank and the input table.

- **Devices for monitor and measurement.** Several devices are placed to diagnose the status of the interferometer: AF photo detectors for monitoring the laser power, and an optical spectrum analyzer for the measurement of the reflected sidebands.

- **Vacuum system.** The interferometer is housed in a vacuum system comprised of a recycling tank, center tank, two end tanks, and vacuum tubes. The vacuum system is evacuated with a scroll pump.

Table 5.2: Main parameters of the 3-m prototype interferometer.

Parameters of the 3-m prototype interferometer		
Parameter	Symbol	Value
Power of the laser source	P_{l}	35 mW
Wavelength of the laser beam	λ_{l}	1064 nm
Modulation frequency	$\omega_{\mathrm{m}}/2\pi$	40.265 MHz
Modulation index	m_{m}	0.58 rad
Length of the arm cavities	L_x, L_y	2.95 m
Length of the recycling cavity	$l_+/2$	1.82 m
Asymmetry	l_-	15 cm
Reflectivity of the front mirrors	R_{F}	97.4 %, 97.1 %
Reflectivity of the end mirrors	R_{E}	99.6 %, 99.9 %
Reflectivity of the recycling mirror	R_{R}	63.6 %
Reflectivity of the pick-off mirror	R_{P}	adjustable
Finesse of the arm cavities	$\mathcal{F}$	230
Power recycling gain	G_0	2.5 ($T_{\mathrm{P}} = 0.872$)
Power gain for the sidebands	G_1	3.3 ($T_{\mathrm{P}} = 0.872$)

Table 5.3: Specifications of the mirrors of the 3-m interferometer.

Mirrors				
		Front mirror	End mirror	Recycling mirror
Diameter		30 mm	30 mm	30 mm
Thickness		5 mm	5 mm	5 mm
Curvature		∞ (flat)	4.5 m	4.28 m
Reflectivity		97.5%	99.9%	60%
Measured	(x arm)	97.4%	99.6%	63.6%
reflectivity	(y arm)	97.1%	99.9%	

5.1 Optical design

In this Section, we show the optical design of the 3-m prototype interferometer. This interferometer is a Michelson interferometer with Fabry-Perot arm cavities. In addition, power recycling is applied to this interferometer.

5.1.1 Mirrors

The interferometer is comprised of five main mirrors: two front mirrors, two end mirrors, and a recycling mirror. Table 5.3 shows the specifications of these mirrors. Though the reflectivities of mirrors are selected in a similar way as a real large gravitational wave detector, they are selected to be suitable values for our experimental purposes. The reflectivity of the front mirrors is selected to realize sufficiently high finesse about a few hundred[1]. The reflectivity of the end mirrors is selected high so as to obtain a high reflectivity of the cavities, which is necessary to realize a high recycling gain[2]. With the reflectivities of 97.5 % (front mirror) and 99.9 % (end mirror), the arm cavity have a finesse of about 240 and

[1]The finesse is usually selected so that the cut-off frequency of the cavity would be near the observation band of gravitational waves in a real gravitational wave detector. A finesse of one hundred results in a cut-off frequency about a few hundred hertz in a km-class interferometer. In the 3-m interferometer the cut-off frequency is about one hundred kHz.

[2]It is possible to make a mirror with higher reflectivity. However, it is not easy to keep such a high reflectivity with our experimental environment. For the purpose of our experiment, the reflectivity of 99.9% for the end mirrors is sufficient.

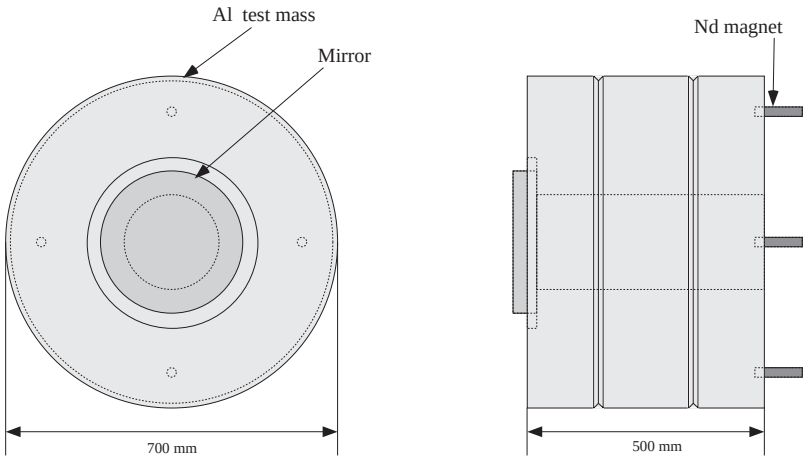

Figure 5.2: Each mirror is attached to a cylinder test mass made of aluminum, and suspended by a double pendulum. Four permanent magnets are attached to the test mass, which form coil-magnet actuators. The test mass is suspended with two turns of tungsten wire.

a reflectivity of 83.0% (calculation).

The reflectivity of the recycling mirror is usually selected to realize a high recycling gain in a real gravitational wave detector, which usually becomes larger than 90 %. In the 3-m interferometer, the designed recycling gain is around three, and the reflectivity of the recycling mirror is designed to be 60%. We selected this reflectivity with two reasons. One reason is to avoid an unnecessary difficulty for demonstration of power recycling. One of the purposes of our experiment is to realize power recycling and investigate the lock-acquisition properties with a suspended Fabry-Perot-Michelson interferometer. For this purpose, a recycling gain around three is sufficient. Another reason is to evaluate the signal-separation scheme, which is the other purpose of our experiment: the reflectivity of the recycling mirror is selected so that the recycling cavity could be varied from the under-coupled condition to the over-coupled condition for the sidebands by adjusting the transmissivity of the pick-off mirror.

The diameter and thickness of the mirrors are 30 mm and 5 mm, respectively. Each mirror is attached to a cylinder test mass made of aluminum (Fig. 5.2), and suspended as a double pendulum (Section 5.2). Another side of the mirror substrate is anti-reflection (AR) coated. The reflectivity of the AR coat is 0.6%.

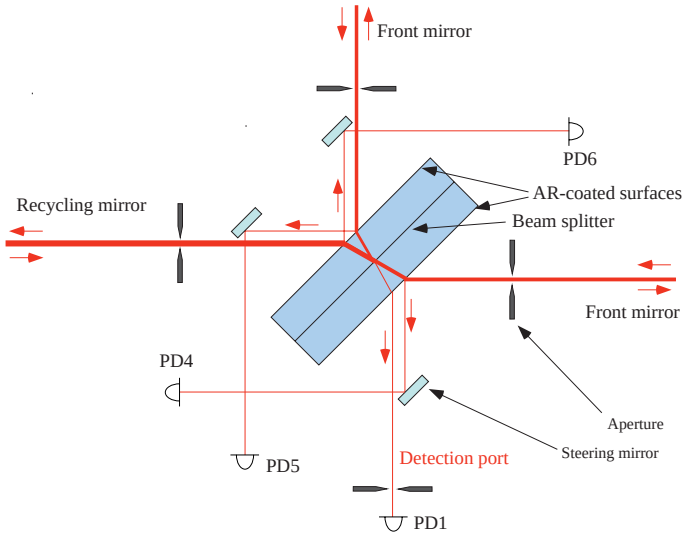

Figure 5.3: Laser beams around the beamsplitter. The reflected beams by the AR surfaces are used to monitor the laser power inside the recycling cavity (PD6), and to lock the arm cavities independently in a lock acquisition step (PD4 and PD5). Unnecessary beams by multi-reflection on the AR and BS surfaces are rejected with apertures.

5.1.2 Beam splitter

The beamsplitter (BS) plate is made by bonding two glass substrates (Fig. 5.3). The diameter of the beamsplitter is 100 mm, and the thickness is 30 mm. Both sides of the beamsplitter plate are AR-coated; the reflectivity of the AR surfaces is 0.6%. The reflected beams on the AR surfaces are used to monitor the laser power inside the recycling cavity (PD6), and to lock the arm cavities independently in a lock acquisition step (PD4 and PD5, Section 6.1). Unnecessary beams by multi-reflection on the AR and BS surfaces are rejected with apertures.

The beamsplitter is designed to separate the input beam equally in two direction for p-polarized laser beam. The measured reflectivity and transmissivity are 52.5% and 46.4%, respectively.

The beamsplitter plate is also suspended as a double pendulum.

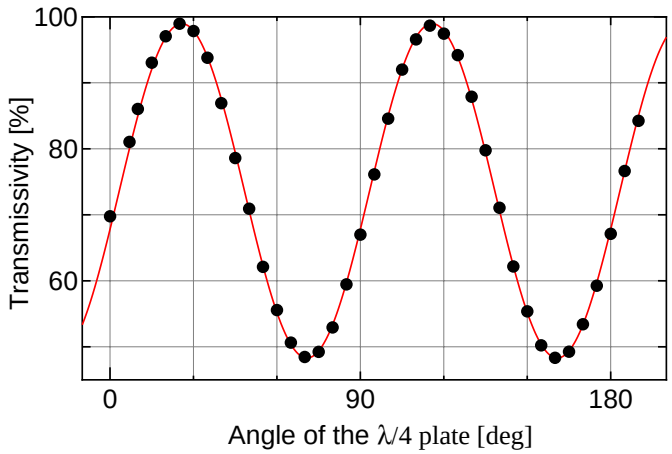

Figure 5.4: The transmissivity of the pick-off mirror composed with a $\lambda/4$ plate and two polarizers. The dots and the solid curve represent the measured and fitted transmissivity. The transmissivity is varied by rotating the $\lambda/4$ plate. The maxim and minimum transmissivities of this pick-off are 98.9% and 48.3%, respectively.

5.1.3 Pick-off mirror

In order to realize the signal-separation scheme (Chapter 4), the reflectivity of the recycling mirror $R_{\rm R}$ has to be set equal to that of the compound mirror for the sidebands $R_{\rm com1}$. However, it is not easy to produce a mirror setting the reflectivity in a high accuracy. In addition, the reflectivity of the compound mirror depends on the condition of the interferometer: the mirror contamination and the alignment of the interferometer[3].

The signal-separation condition is written by the equation $R_{\rm R} = R_{\rm com1} \simeq T_{\rm P}^2 \cos^2\alpha$ as described in Eq. 4.92. Thus, instead of adjusting the reflectivity of the recycling mirror, the signal separation is also realized by adjusting the reflectivity of the compound mirror for the sidebands. In the 3-m interferometer, the pick-off in the recycling cavity is formed with a $\lambda/4$ plate and two polarizers; the transmissivity of the pick-off mirror is variable by rotating the $\lambda/4$ plate, which is mounted in a motorized rotary stage. Figure 5.4 shows the measured transmissivity of the pick-off mirror. The maxim and minimum transmissivities of

[3]However, the effect of the mirror contamination is not as serious for $R_{\rm com1}$ as that for $R_{\rm com0}$ because the sidebands do not enter the arm cavity.

Table 5.4: Parameters of the arm cavity of a 3-m Fabry-Perot-Michelson interferometer.

Arm cavity		
Parameter	Symbol	Value
Length	L	2.95 m
FSR	ν_{FSR}	50.8 MHz
Finesse	$\mathcal{F}$	240
Cut-off frequency	f_{cav}	106 kHz
Reflectivity	r^2_{reso}	83.0%

this pick-off are 98.9% and 48.3%, respectively. The resolution of transmissivity adjustment is smaller than 0.02%, which is limited by the resolution of the rotary stage of the $\lambda/4$ plate[4].

5.1.4 Fabry-Perot arm cavity

Table 5.4 shows the parameters of the arm cavity. The length is 2.95 m, corresponding to the FSR of 50.8 MHz. The calculated finesse is about 240, while the measured finesse using a sideband method is about 230 for both arm cavities. The reflectivity of the cavity is calculated to be 83.0%, assuming a mirror loss of 100 ppm. The measured cavity reflectivities are 84.7% and 82.6%.

5.1.5 Michelson interferometer and power recycling

The asymmetry between the distance from the recycling mirror to the front mirrors are set to be 15 cm. This is the largest value to place the mirror suspensions in the vacuum tank[5]. With a modulation frequency of 40.265 MHz, $\alpha = 0.13$ rad; the transmissivity of the RF sidebands to the detection port is 1.62%.

[4]The resolution of transmissivity adjustment depends on the transmissivity. When the transmissivity is set around the highest or lowest, the resolution is negligibly small.

[5]The asymmetry and modulation index is usually determined so as to optimize the shot noise level at the detection port. In a 3-m interferometer, the RF sideband power at the detection port cannot be optimized even with the maximum asymmetry and modulation index.

Table 5.5: Parameters of power recycling of a 3-m Fabry-Perot-Michelson interferometer when the transmissivity of the pick-off is 87.2%.

Power recycling		
Parameter	Symbol	Value
Recycling gain	G_0	2.5
Power gain for the sidebands	G_1	3.3
Power gain on the beamsplitter	$G_{\rm BS}$	2.6
Length of the recycling cavity	$l_+/2$	1.82 m

With a pick-off transmissivity of 87.2% (the signal-separation condition, Section 6.3) the recycling gain is calculated to be 2.5 and the power gain for the RF sidebands is 3.3 (Table. 5.5)[6]. From these values and the modulation index, the power gain on the beamsplitter is calculated to be 2.6.

5.2 Suspension system

5.2.1 Double pendulum

The main optics (the front, end, and recycling mirrors, and the beamsplitter) are suspended as double pendulums (Fig. 5.5). The upper stage of the double pendulum (a upper mass) is dumped by eddy current; strong permanent magnets are placed around the upper mass. Since the dumping magnets are supported by a bending spring, the upper mass is not dumped over the resonant frequency of the bending spring. This bending spring realizes stability of the pendulum in lower frequency range around the resonant frequencies of the double pendulum, and at the same time, high vibration isolation ratio in a higher frequency range. The vertical seismic motion is isolated with the leaf springs and the coil springs at the top of the suspension system.

The orientation of each mirror is adjusted using optical stages at the suspension point, and coil-magnet actuators at the test mass. In a vacuum, mirrors are

[6]When the pick-off has the maximum transmissivity, the recycling gain is calculated to be 4.1.

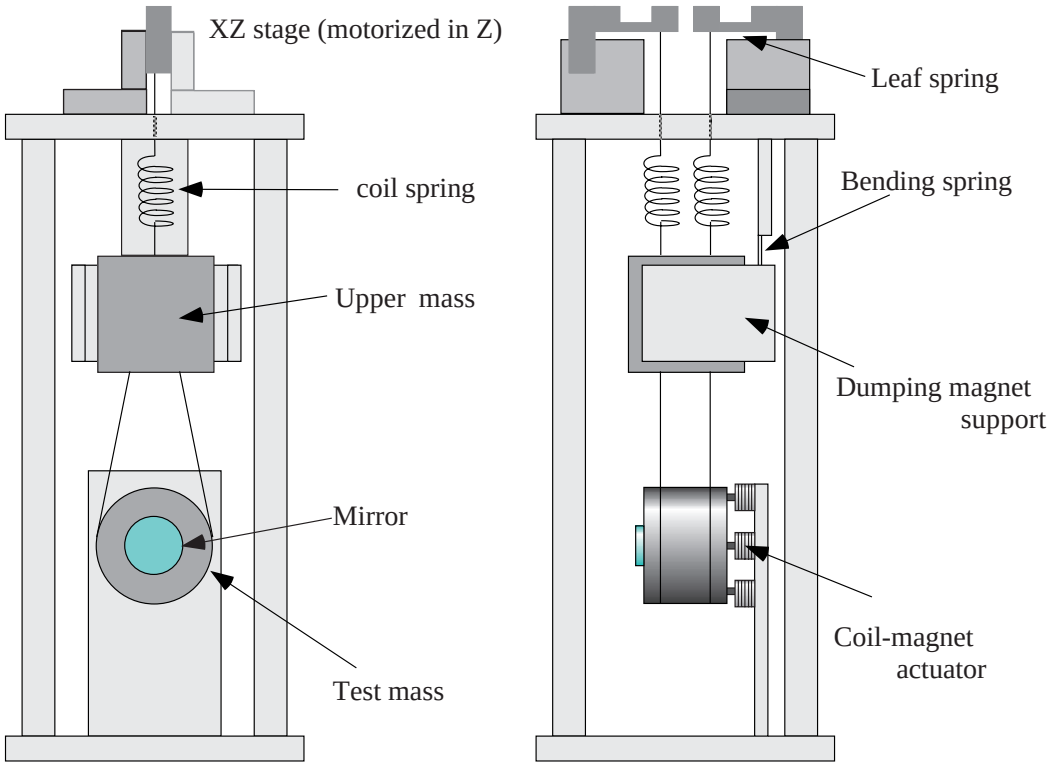

Figure 5.5: Suspension system for the mirror. The mirror is suspended as a double pendulum. The upper mass is dumped by a strong permanent magnets placed around it. The position and orientation of the mirror is controlled or adjusted with motorized stage and the coil-magnet actuators.

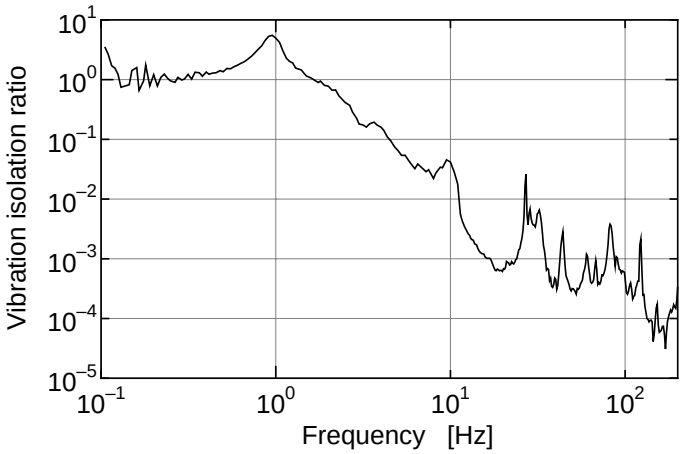

Figure 5.6: Vibration isolation ratio of the suspension system. The isolation ratio is degraded by resonances of the suspension system.

aligned with motorized micro stages (in a pitch direction) and the coil-magnet actuators (in a yaw direction). No active control of the alignment is applied to the 3-m interferometer.

5.2.2 Isolation ratio

The vibration isolation ratio, the ratio of the motion of the suspension point to that of the mirror mass, is measured by shaking the suspension system. The measured vibration isolation ratio is shown in Fig. 5.6 [72]. The mirror motion at the resonance of the pendulum around 1 Hz is damped with the permanent magnets. The vibration isolation ratio is about 3×10^{-2} at 10 Hz, and 3×10^{-4} at 100 Hz. The ratio is degraded from the ideal case because of the resonances of the suspension system.

5.2.3 Coil-magnet actuator

In order to to keep the interferometer at the operational point, it is necessary to control the position of the suspended optical components. The mirror position is controlled with permanent magnets attached on the back of a mirror test mass and coils placed nearby the magnets. The strong Nd permanent magnets attached to the test mass have a length of 10 mm and a diameter of 2 mm.

Table 5.6: Actuator efficiencies at 3 kHz; the mirror displacement caused by voltage input to the coil driver. The efficiency of the PZT on the laser source is shown together.

Actuators	
Actuator	Efficiency
Front mirror (x)	5.2×10^{-12} m/V
Front mirror (y)	3.4×10^{-12} m/V
Beam splitter	2.0×10^{-12} m/V
Recycling mirror	3.8×10^{-12} m/V
PZT	2.59 MHz/V

Two coil-magnet actuators (upper and lower actuators) are used to control the longitudinal position (in the direction along the laser beam) of the test mass. The other two actuators are used to adjust the angle of the test mass (in the yaw direction).

Calibration of the mirror actuators

The efficiency of a coil-magnet actuator is described by the transfer function from the input voltage into the coil diver to the displacement of the test mass. The actuator efficiencies of the front mirrors and the beamsplitter are calibrated with the simple front-mirror Michelson interferometer controlled with a differential method.

The efficiency of the actuator of the recycling mirror is measured with a cavity comprised of the recycling mirror and one of the front mirror, comparing the output signal when each of the front mirror and the recycling mirror is shaken.

The measured efficiency of the actuators measured at 3 kHz are summarized in Table 5.6. The efficiency of the PZT on the laser head is also described together. These efficiencies of the actuators are used to calibrate the error signals and to estimate the signal-mixing ratio under operation of the interferometer.

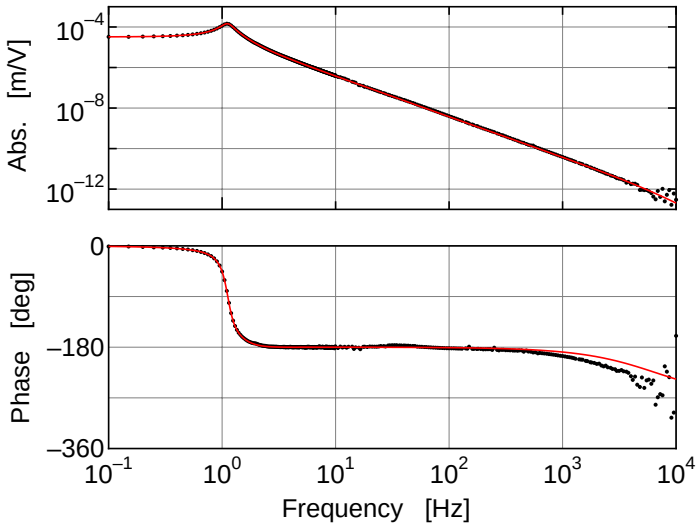

Figure 5.7: Bode diagram of the frequency response of the coil-magnet actuator. The dots represent measured responses using photo sensor (below 10 Hz) and front mirror Michelson interferometer (above 10 Hz). The solid curve shows the fitted response of the actuator.

Frequency response of a mirror actuator

Figure 5.7 is the measured frequency response of the coil-magnet actuator: a transfer function from the voltage into the coil driver to the displacement of the test mass. The dots and the solid curve represent the measured and fitted response. The displacement below 10 Hz is measured using photo sensor. The displacement above 10 Hz is measured with a front mirror Michelson interferometer, locking with a differential method. The phase delays by π at the resonant frequency of the pendulum around 1 Hz. The Q-value of the pendulum mode is estimated to be 2.6. The phase delay around kHz region is due to the inductance of the coil.

5.3 Laser

Figure 5.8 shows the optical setup on the laser table; the laser source, input optics, and the reflection-port detectors are placed on this table. The optical path is steered with high-reflection mirrors to adjust the axis of the input beam.

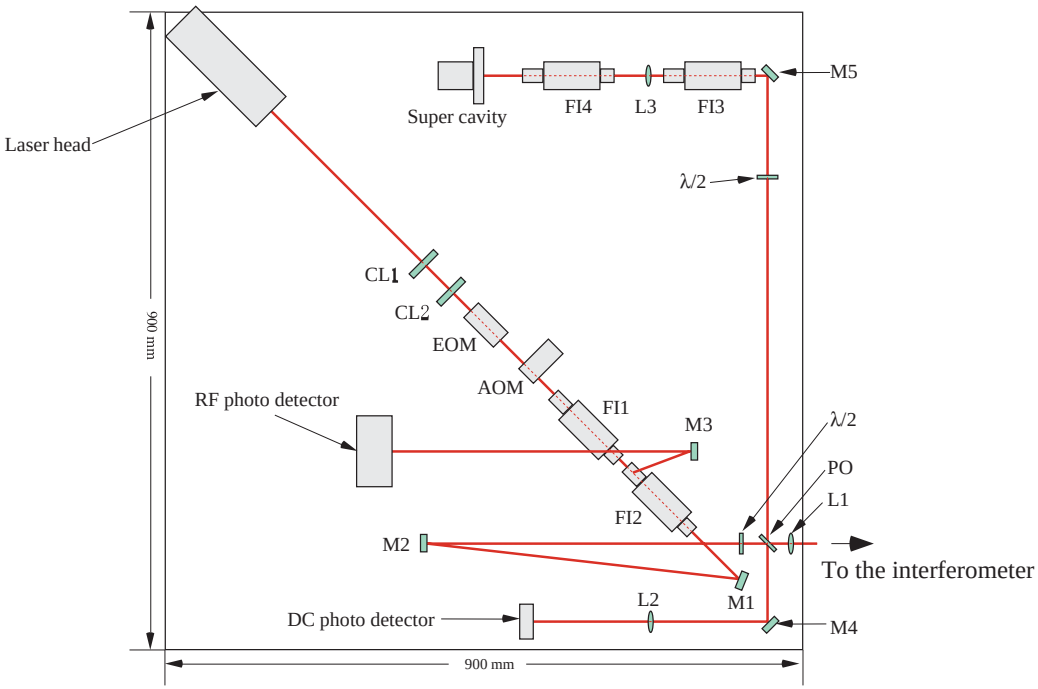

Figure 5.8: Optical setup on the laser table. The laser beam is introduced into the vacuum tank after passing through a phase modulator (EOM), an intensity modulator (AOM), optical isolators (FI), and mode-matching lenses (L, CL). M: steering mirror, PO: beam sampler, $\lambda/2$: half-wave plate.

Table 5.7: Specifications of the laser source. Intensity and frequency noise levels are measured value at 1 kHz.

Laser source		
Parameter	Symbol	Value
Wavelength	λ_l	1064 nm
Output power	P_l	35 mW
Intensity noise	$\delta P_l/P_l$	1×10^{-7} $1/\sqrt{\text{Hz}}$
Frequency noise	$\delta\nu_l/\nu_l$	6 Hz/$\sqrt{\text{Hz}}$
Fast frequency tuning		2.59 MHz/V

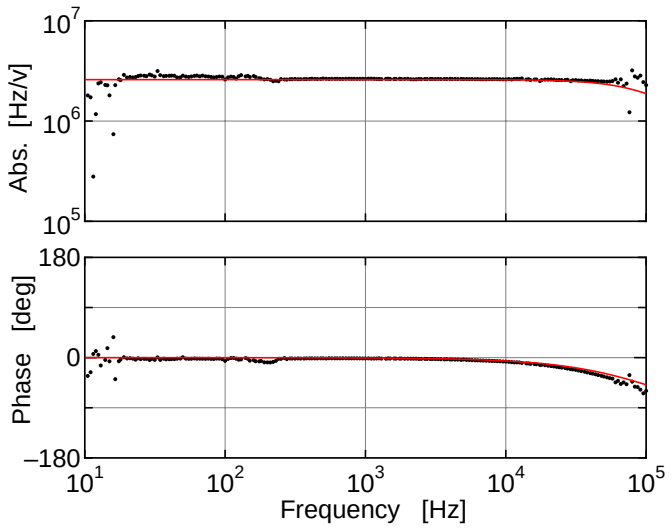

Figure 5.9: Bode diagram of frequency response of the PZT actuator of the laser source measured by one of the arm cavities. The response of the PZT is almost flat up to 100 kHz. The phase dilation is due to the cut-off of the cavity. The frequency tuning efficiency of the PZT is estimated to be 2.59 MHz/V from this measurement.

5.3.1 Laser source

As a laser source, we use a laser-diode pumped Nd:YAG laser[7] (LIGHTWAVE electronics, model 124-1064-050-F) comprised of a monolithic non-planar ring oscillator (NPRO). The specifications of the laser source is summarized in Table 5.7. The wavelength is 1064 nm and the output power is about 50 mW. However, the laser power introduced into the interferometer is reduced to 35 mW because of the insertion losses of a phase modulator and isolators and so on.

The output frequency can be tuned with a piezoelectric element (PZT) bonded onto the laser crystal, and with a thermoelectric cooler under the crystal. Figure 5.9 shows a measured frequency response of PZT using one of the arm cavities. The response of the PZT actuator is almost flat up to 100 kHz, and the frequency tuning efficiency is 2.59 MHz/V. Using a relation of the response of a Fabry-Perot cavity to the frequency and displacement changes: $|\delta L| = |\delta\nu_1/\nu_1|\, L$, the corre-

[7]Since Nd:YAG laser has good frequency and intensity noise properties, it will also be used in interferometric gravitational wave detectors under construction [11, 12, 13, 14].

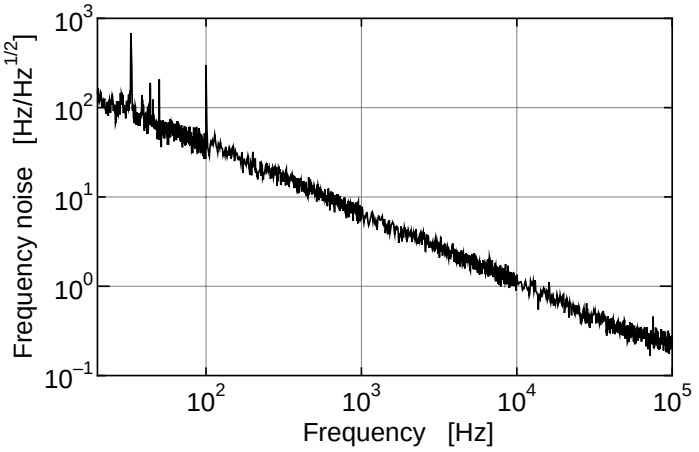

Figure 5.10: Frequency noise spectrum of the laser source without frequency stabilization (under free-running condition). The frequency noise is 6 Hz/$\sqrt{\text{Hz}}$ at 1 kHz.

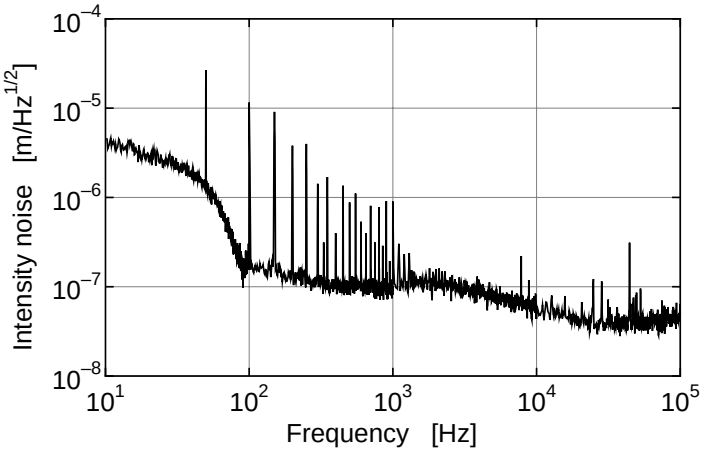

Figure 5.11: Intensity noise spectrum of the laser source under free-run condition. The intensity noise is 1×10^{-7} $[1/\sqrt{\text{Hz}}]$ at 1 kHz.

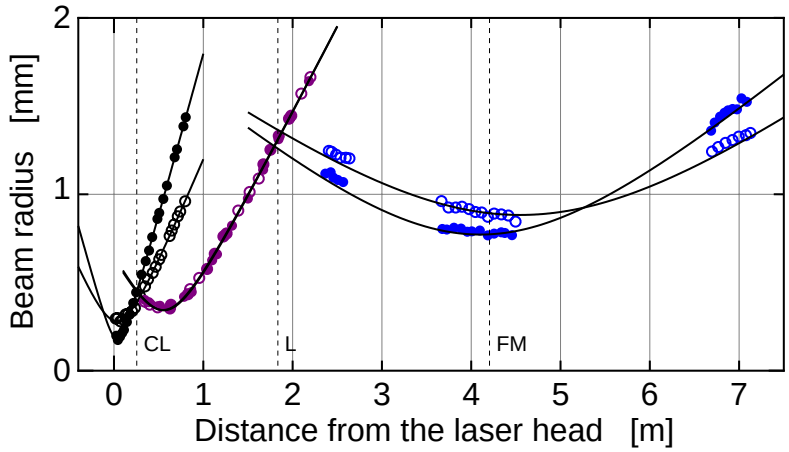

Figure 5.12: Beam profile of the incident beam. The mode of the incident beam is transformed with three lenses to match with the interferometer. The closed and open circles represent the beam radius in horizontal and vertical direction, respectively. Solid curves represent the fitted beam profiles.

sponding displacement of the arm mirror is 2.71×10^{-8} m/V. Where ν_1 is the frequency of the laser source, and L is the length of the cavity. The phase of the measured response delays because of the cut-off frequency of the cavity. We do not use the thermoelectric cooler for the frequency control.

Using one of the arm cavities, the frequency noise of the laser source is measured (Fig 5.10). The frequency noise level without any frequency control is almost proportional to f^{-1}, 6 Hz/$\sqrt{\text{Hz}}$ at 1 kHz. This frequency noise corresponds to the displacement noise of 6×10^{-14} m/$\sqrt{\text{Hz}}$ for the 3-m arm cavity. The intensity noise of the laser source is also shown in Fig. 5.11. The noise level is 1×10^{-7} $1/\sqrt{\text{Hz}}$ at 1 kHz.

5.3.2 Mode matching

The shape of the output laser beam is elliptical because the beam is emitted from a ring cavity. This means that the output beam contains higher-order transverse modes besides the TEM_{00} mode. These higher-order modes degrade the visibility of the cavities and the contrast at the detection port. Thus we shape the elliptical

Table 5.8: Maximum coupling ratios with TEM_{00} mode estimated from beam profiles of the laser beam measured at the output of the laser source, after the cylindrical lenses, and after convex lens. The measured mode matching ratio is 99.1 %.

Mode matching	
Position	Maximum coupling ratio
Laser source	0.977
After the cylindrical lenses	0.999
After the convex lens	0.996
Measured matching ratio	0.991

beam into a circular beam as described below[8].

In order to realize a high mode-matching ratio, two cylindrical lenses and a concave lens are used to transform the mode of the input laser beam. The two cylindrical lenses are used to transform this elliptical beam to a circular beam. The maxim coupling ratio of the beam with a TEM_{00} mode indicates the maxim mode-matching ratio of the elliptic beam with a cavity [74]. This ratio is not changed with an ideal coaxial lens. By the transformation of the beam with cylindrical lenses, the coupling ratio is improved, which results in a good mode-matching ratio of 99.1%. The transformation of the beam profile is summarized in Table 5.8 and Fig. 5.12.

5.3.3 Optical isolators

In order to prevent the back-reflected beam from entering the laser source again, two Faraday isolators (OFR,Inc., model IO-2-YAG) are used. Each optical isolator eliminates the back reflected beam less than 100 ppm (specification).

The laser beam coming back from the interferometer is reflected with the second isolator (FI2). This beam, called the reflection port beam, is steered with a mirror and detected by a RF photo detector (PD3). The δl_- and δl_+ signals

[8]In an usual configuration of an interferometric gravitational wave detector, higher-order transverse modes are rejected with a mode cleaner in front of the interferometer [73]. However, a mode cleaner is not used in the 3-m prototype interferometer.

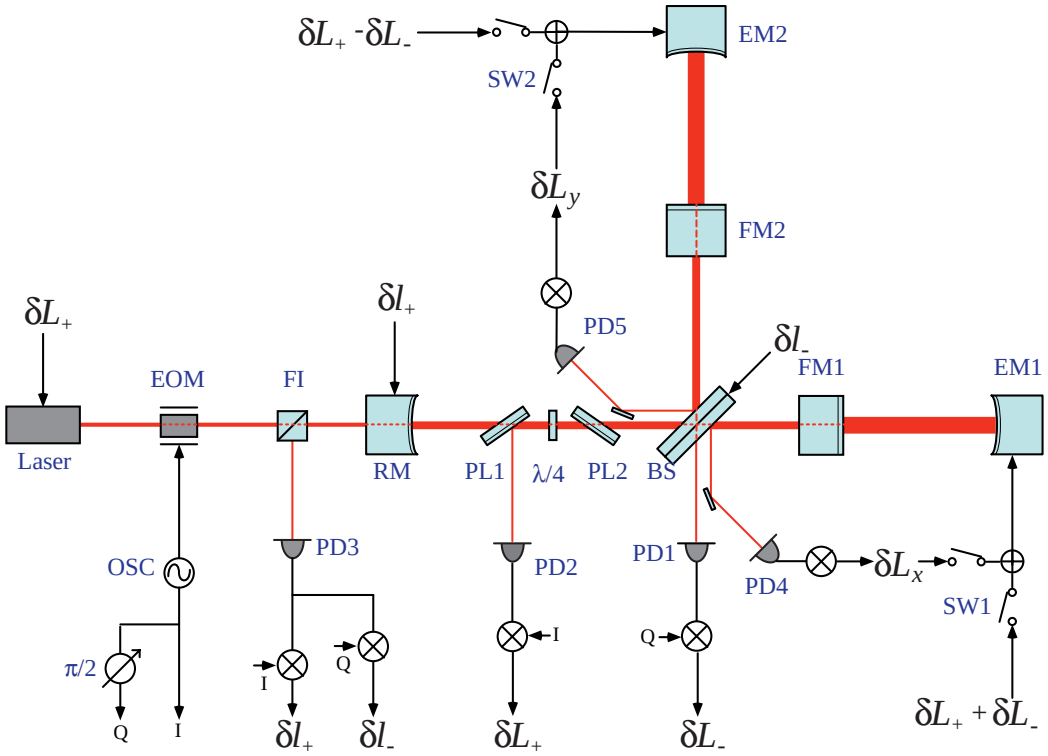

Figure 5.13: Diagram of the signal-extraction and control system of a 3-m Fabry-Perot-Michelson interferometer. The δL_- and δL_+ signals are fed back to the actuators of the end mirrors differentially and commonly, respectively. The δL_+ signal is also used to control the frequency of the laser source. The δl_- and δl_+ signals are used to control the beamsplitter and the recycling mirror, respectively.

are extracted by demodulating the output of PD3.

5.4 Signal extraction and control system

Figure 5.13 is a diagram of the signal-extraction and control system of the 3-m Fabry-Perot-Michelson interferometer. The four signals necessary for the control of the interferometer are extracted with frontal modulation, and fed back to the corresponding actuators after processed with electronic filters.

Table 5.9: Modulation parameters of a 3-m Fabry-Perot-Michelson interferometer.

Modulation		
Parameter	Symbol	Value
Asymmetry	l_-	15 cm
Modulation frequency	$\nu_{\rm m}$	40.265 MHz
Modulation index	$m_{\rm m}$	0.58 red.

5.4.1 Modulation, demodulation, and control

The modulation signal is buffered and divided with a RF power divider. Each output of the power divider is shifted in phase with a phase shifter and input to a demodulator as a local oscillator signal. A demodulator contains the mixer, a low-pass filter, and an amplifier. As a mixer, a passive double-balanced-mixer (DBM) is used, which multiplies the output of the photo detector by the local oscillator and down-converts the frequency components around the modulation frequency to a lower frequency around DC. The output of the mixer is followed with a low-pass filter and amplified.

The δL_- signal is obtained by demodulating the output of PD1 in quadrature-phase ($V_{\rm DQ}$), and fed back to the actuators of the end mirrors differentially. The δL_+ signal is obtained by demodulating the output of PD2 in in-phase ($V_{\rm PI}$). This signal is used to control the frequency of the laser source in a higher frequency range as well as the common control of the end mirrors in a lower frequency range. The crossover frequency of these control loops is about 10 Hz. From the output of PD3, the δl_- and δl_+ signals are obtained by demodulating it in quadrature-phase and in-phase, respectively ($V_{\rm RQ}$ and $V_{\rm RI}$). These signals are used to control the beamsplitter and the recycling mirror, respectively.

The reflected beams from the arm cavities are picked-off with the AR surface of the beamsplitter. These beams are received with RF photo detectors (PD4, PD5), and produce the δL_x, δL_y signals. The δL_x, δL_y signals are sensitive to the corresponding arm cavity motions, and fed back to corresponding end mirrors in a lock-acquisition step. Details of the lock-acquisition scheme are described in Section 6.1.

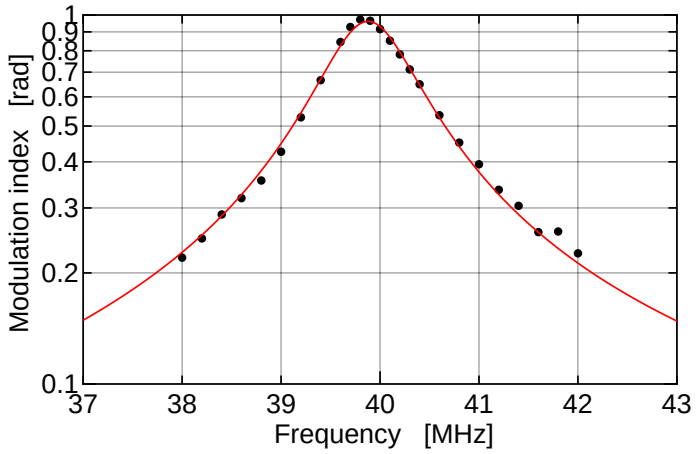

Figure 5.14: Measured frequency response of the phase modulator. The center frequency of the resonance is 39.88 MHz and a Q-value is 42.5.

5.4.2 Oscillator

The RF signal for phase modulation and demodulation is generated by a function synthesizer. The modulation frequency is set to be 40.265 MHz, which is adjusted to satisfy the resonant condition of the RF sidebands with the recycling cavity. The modulation signal of 10 V_{pp} from a function synthesizer (SONY TEKTRONIX Inc., model AFG2020) is applied to the phase modulator. This RF modulation signal is buffered by a power divider and distributed to the demodulators as local oscillators. The phase of each local oscillator signal is adjusted with a phase shifter so as to minimize the unnecessary signals.

5.4.3 Phase modulator

In order to control and operate the interferometer, the input laser beam is phase-modulated in front of the interferometer. The modulation frequency is usually set over about 10 MHz, where the intensity noise of the laser source is below the shot noise level. The phase modulation around RF frequency is realized with an electro-optic-modulator (EOM). We use a resonant-type EOM (NEW FOCUS Inc., model 4003); the electro-optic crystal ($LiTaO_3$) is combined with an inductor to form a resonant circuit, resulting in a high modulation index with a small input voltage. Figure 5.14 and 5.15 show the measured performance of the EOM. The

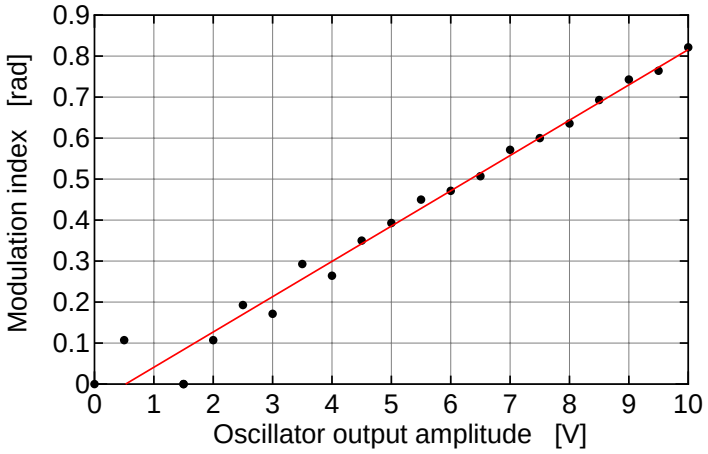

Figure 5.15: Modulation efficiency of the phase modulator at 40.265 MHz. The efficiency is estimated to be 0.086 rad/V from this figure.

modulation indices are measured by the transmitted power through a cavity with and without the modulation ($P_{\rm mod}$ and $P_{\rm non-mod}$).

$$\frac{P_{\rm mod}}{P_{\rm non-mod}} = \left(\frac{J_0(0)}{J_0(m_{\rm m})} \right)^2 .$$

Figure 5.14 shows the frequency response of the modulator. The center frequency of the resonance is 39.88 MHz and a Q-value is 42.5. Figure 5.14 shows the modulation efficiency of the modulator at 40.265 MHz. The efficiency is estimated to be 0.086 rad/V from this figure.

In practice, the RF modulation signal is degraded because of the losses in connectors and cables. The modulation index is 0.58 rad when the interferometer is under operation.

5.4.4 RF photo detector

To detect and obtain the control signals from the intensity change in the laser beam at the modulation frequency, it is necessary to use high-speed and low-noise photo detectors.

We made RF photo detectors using InGaAs photo diode with a diameter of 1 mm (EG&G optoelectronics Inc., C30641). This diode has a good response at the modulation frequency of 40 MHz, and a good efficiency of 0.75 A/W for the

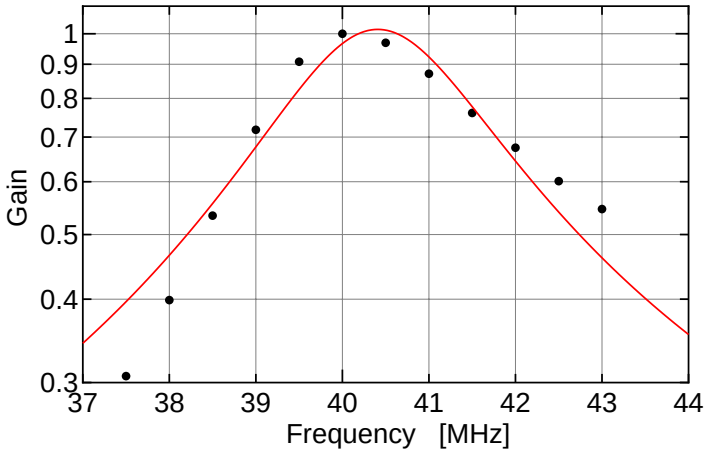

Figure 5.16: Frequency response of a RF photo detector (PD1). The dots and solid curve represent the measured and fitted response of the detector. The center frequency of the resonance is 40.4 MHz and the Q-value is 16.

Nd:YAG laser beam with a wavelength of 1064 nm. The photo current around the modulation frequency is converted to voltage and amplified with an LC tank circuit. Figure 5.16 shows the frequency response of the photo detector. The center frequency is tuned to be around 40 MHz. The Q-value of the resonant circuit is estimated to be 16 from this measurement[9].

The DC photo current is also monitored with this detector, which is used for the estimation of the shot-noise level, and investigation of the operational point of the interferometer.

5.4.5 Demodulator

In order to obtain the error signals corresponding to the interferometer deviations, the outputs of the photo detectors are demodulated with double-balanced modulators (DBM). A DBM down-converts the signal at the RF modulation frequency to a signal around audio frequency (AF) region, by multiplying the RF signal from a photo detector with a local oscillator signal. The local oscillator signal for each DBM is provided from the power divider, and its phase is adjusted

[9]It is possible to obtain a Q-value over 60. In this experiment, the Q-value is dumped so as to maintain the detector bandwidth wide.

Table 5.10: Gain and noise of the demodulation systems. The gain of each demodulation system is attenuated properly to avoid the saturation of RF signal.

Demodulation						
Signal	Control	Beam port	PD	Phase	$g_{\rm det}$ [Ω]	$i_{\rm det}$ [mA]
$V_{\rm DQ}$	δL_-	Detection	PD1	Q	7.1×10^3	0.26
$V_{\rm RQ}$	δl_-	Reflection	PD3	Q	1.4×10^4	0.30
$V_{\rm PI}$	δL_+	Pick off	PD2	I	2.1×10^4	0.22
$V_{\rm RI}$	δl_+	Reflection	PD3	I	1.4×10^4	0.23

with a phase modulator. The output of a DBM is processed with a low-pass filter to reject the up-converted signal and the leaking RF signal at the modulation frequency and its harmonics. The low-pass filter is followed by a buffer amplifier.

The noise performance of the modulation-demodulation system is measured by changing the input laser power on the photo detector (Fig. 5.17). The detection system noise is described by the corresponding photocurrent. The relation of the noise level and the photocurrent is written as Eq. (4.23)

$$V_{\rm det} = g_{\rm det}\sqrt{e(i_{\rm DC} + i_{\rm det})} \quad [{\rm V}/\sqrt{\rm Hz}], \tag{5.1}$$

where $i_{\rm DC}$ is the DC photocurrent, $g_{\rm det}$ is the total demodulation gain (the conversion ratio of RF photocurrent to the error signal), and $i_{\rm det}$ is the dark current corresponding to the noise of the demodulation system. When the input power is high enough ($i_{\rm DC} > i_{\rm det}$), the floor level of the error signal is dominated by shot noise, which is proportional to the square-root of the photocurrent. On the other hand, when the input power is small ($i_{\rm DC} < i_{\rm det}$), the noise level is determined by the noise of the detection system. The gain and noise of each demodulation system is summarized in Table 5.10.

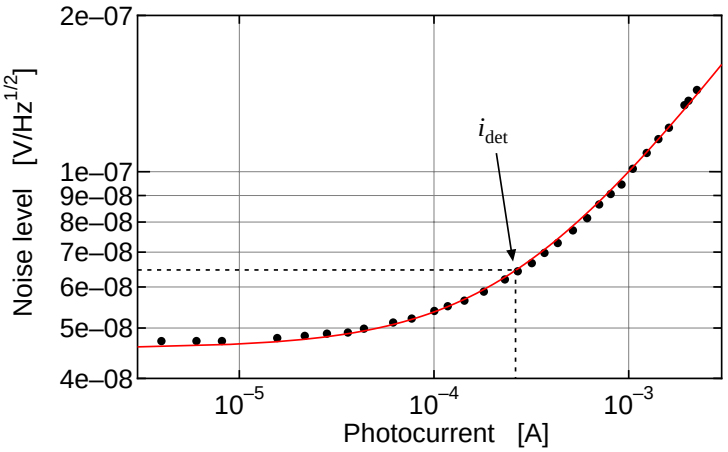

Figure 5.17: Measured noise level of the demodulated signal for δL_- in a function of photocurrent. Dots and solid curve represent the measured and fitted noise levels, respectively. The correspond noise current of the demodulation system ($i_{\rm det}$) is 0.26 mA.

5.5 Devices for monitor and measurement

5.5.1 AF photo detector

Besides the RF photo detector, photo detectors are placed to monitor powers of laser beams from the interferometer. The power on the beamsplitter is monitored with PD6 detecting the reflected beam on the AR surface of the beamsplitter. The transmitted beams through the arm cavities are monitored with PD7 and PD8. The incident laser power into the interferometer is monitored with PD9 placed on the input laser table.

5.5.2 Intensity modulator

An acousto-optic-modulator (AOM) placed in the input laser table is used to modulate the intensity of the input beam. The effect of intensity noise is estimated by modulating the input laser power.

The input laser beam into the interferometer is picked off by a partial mirror (a reflectivity of about 10%), and its intensity noise is monitored with a photo detector (PD9). The intensity of the input laser beam can be stabilized by feeding

back the output of PD9 to the AOM after filtering. However, we do not use this intensity stabilization system because the intensity noise of the input beam does not affect the current sensitivity of the interferometer (Section 6.4).

5.5.3 Optical spectrum analyzer

The transmissivity of the pick-off of the interferometer is adjusted so that the signals from the reflection port are insensitive to the δL_+ deviation. This condition is described as $r_{\mathrm{rec1}} = 0$; no first-order sidebands are reflected back to the laser source (Chapter 4). We monitor the power of the sidebands at the reflection port with an optical spectrum analyzer in order to adjust and investigate the signal-separation scheme.

The power of the carrier and sidebands are monitored with a Super Cavity (NEWPORT Inc., model SR-100), which has the frequency resolution about 1 MHz.

5.6 Vacuum system

The main part of the interferometer is housed in a vacuum system in order to avoid the effects of air fluctuation and sound noise (Fig. 5.18). The vacuum system is comprised of a scroll pump and four vacuum tanks connected with vacuum pipes with bellows. The diameter of the center and end tanks is 1 m, and that of the recycling mirror tank is 70 cm. The vacuum pipes have a diameter of 18 cm. The system is evacuated with a scroll pump connected to the center tank. During operation of the interferometer, the pump is turned off to avoid the vibration noises. The vacuum system keeps a pressure of about a few Torr with the pump stopped.

The laser beam from the laser table is introduced in the vacuum system through a window plate attached on the flange of the recycling mirror tank. Each tank has connectors for input to actuators and outputs of the photo detectors.

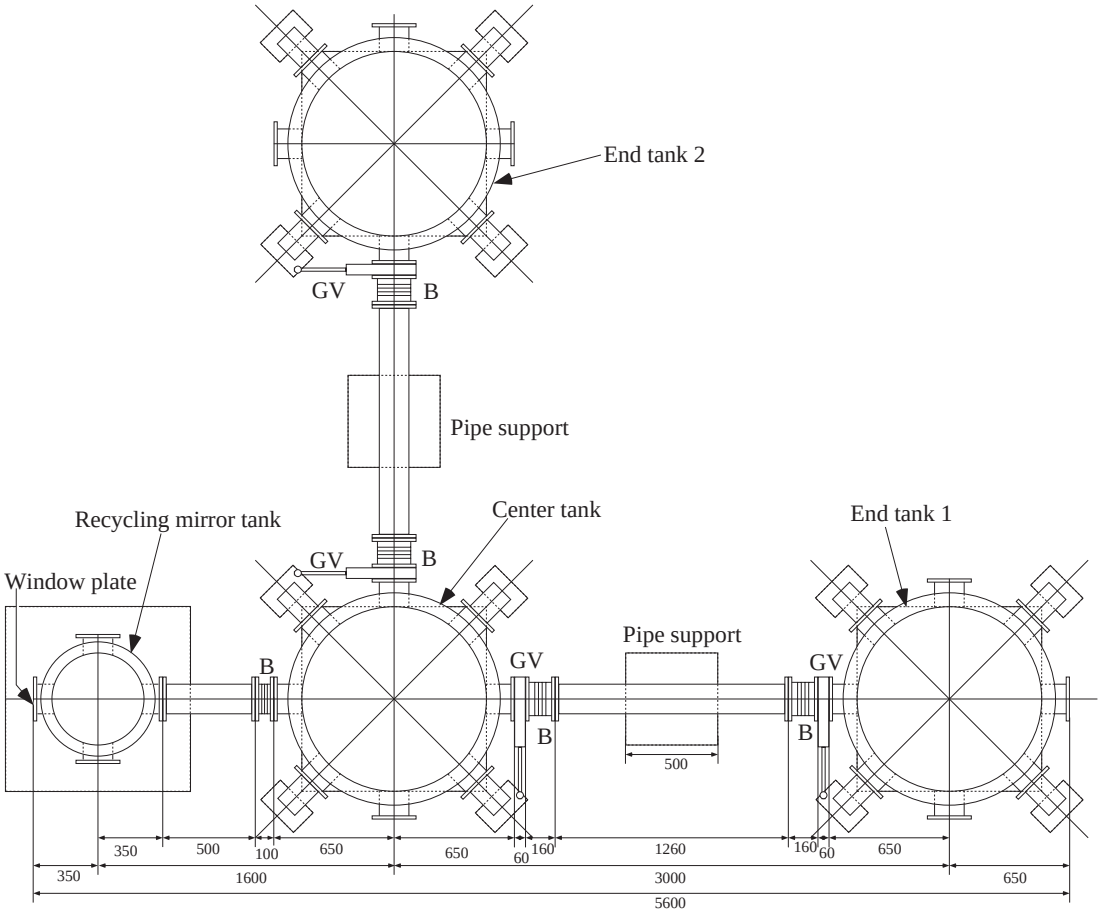

Figure 5.18: Vacuum system of the 3-m Fabry-Perot-Michelson interferometer. The vacuum system is comprised of a scroll pump and four vacuum tanks connected with vacuum pipes, gate valves (GV), and bellows (B).

Chapter 6

Experiment

With the 3-m prototype interferometer, we have developed the control system for a power-recycled interferometer. The experiment contains three topics. The first topic is the lock-acquisition and operation of this prototype interferometer with power recycling [32]. Since power recycling was not demonstrated in a Fabry-Perot-Michelson interferometer with suspended mirrors before this research, it was quite significant to investigate the lock acquisition process experimentally. The second topic of this research is to test the signal-separation scheme for the control of a power-recycled Fabry-Perot-Michelson interferometer [33]. The third topic of this research is to estimate the effect of noise sources in the prototype interferometer. The role of the control system is to maintain the stability, and at the same time, sensitivity of the interferometer. Thus, the control system of the 3-m prototype interferometer is designed not to degrade the sensitivity of the interferometer.

In this Chapter, we describe the results of the power recycling experiments on the 3-m prototype interferometer.

- **Lock acquisition.** Correlation diagram. Lock acquisition schemes: a guide locking scheme and an automatic locking scheme.
- **Operation with power recycling.** Evaluations of the power-recycled interferometer: power recycling gain, stability of the interferometer.
- **Signal separation.** Realization of the signal-separation scheme.

- **Sensitivity of the interferometer.** Displacement noise level and evaluation of noise sources.

6.1 Lock acquisition

With frontal modulation, each control signal is linear to the motion in the corresponding degree of freedom only when the positions of the optical components of the interferometer are near to the operational point. Thus, it is not a simple problem to lock the interferometer from an uncontrolled state, particularly in an interferometer with suspended optical components and a complex optical configuration. In a power-recycled Fabry-Perot-Michelson interferometer, four degrees of freedom must be locked and kept at the operational point.

In the experiment of the 3-m prototype interferometer, we use two lock-acquisition schemes; a guide locking scheme and an automatic locking scheme. In the guide locking scheme, the interferometer is locked at the operational point with auxiliary control loops. The auxiliary control signals are extracted from the reflected beams from arm cavities. The automatic locking scheme is the simplest way to lock the interferometer; the interferometer is locked by just closing all of the longitudinal control loops. The process of the automatic lock has been analyzed with a computer simulation by the LIGO group [75].

6.1.1 Correlation diagram

Here we show correlation diagram of the light power to see the operational status of a power-recycled interferometer. Since the detection port is neither maxim nor minimum at the operational point in a power-recycled interferometer, it is impossible to confirm whether the interferometer is locked correctly by monitoring the power only at the detection port. In order to confirm the operational point of the interferometer, we monitor the light power on the beam splitter ($P_{\rm BS}$) and the power at the detection port ($P_{\rm det}$), and the transmitted power through the arm cavities[1]. The powers $P_{\rm BS}$ and $P_{\rm det}$ are simultaneously monitored by an

[1]The power on the beamsplitter $P_{\rm BS}$ is monitored with PD9, detecting the reflected beam on the AR surface of the beam splitter. The power at the detection port $P_{\rm det}$ is monitored with the DC output of PD1.

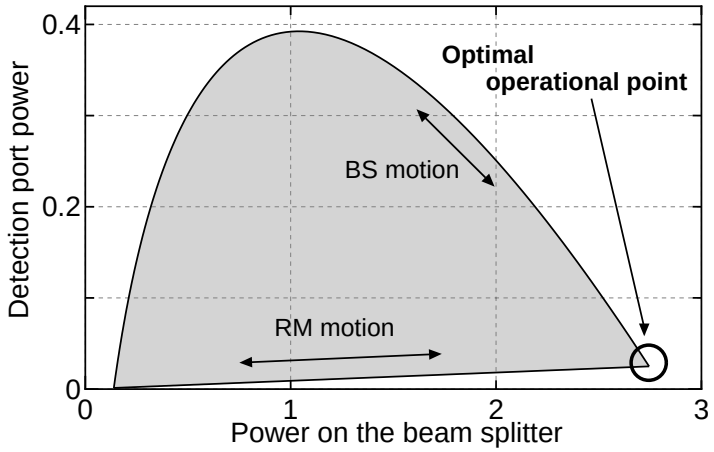

Figure 6.1: Correlation diagram of the light power. In a power-recycled interferometer, the operational point moves in the region bounded by an elliptic curve and a line.

oscilloscope in X-Y mode; the X and Y axes are set to display $P_{\rm BS}$ and $P_{\rm det}$, respectively. The operational point is determined from the position of the spot, and the motions of the mirrors are determined from the locus on the oscilloscope. This locus is called a correlation diagram of the light power[2] [26].

Figure 6.1 shows a correlation diagram of the light power. The horizontal and vertical axises are proportional to $P_{\rm BS}$ and $P_{\rm det}$, respectively. The horizontal axis is normalized so that the power on the beam splitter without recycling mirror should be unity; this value represents the power gain on the beam splitter. In a power-recycled interferometer, the correlation point moves in the region bounded by an elliptic curve and a line[3]. The sensitivity of an power-recycled interferometer is the best when the interference fringe is dark ($\phi_- = 0$) and the power recycling cavity is resonant with the incident laser beam ($\phi_+ = 0$). Under these conditions, the power on the beam splitter is maximized. When the recycling mirror deviates from this optimal operational point, the power in the recycling cavity decreases; the spot moves along the boundary line in the correlation diagram. On the other hand, when the beam splitter deviates from this optimal

[2]The correlation diagram described in this thesis is a little different from that in the reference [26]; the reflected power from the interferometer was used for the horizontal axis.

[3]Here, we assume the arm cavities are kept resonant with the incident laser beam.

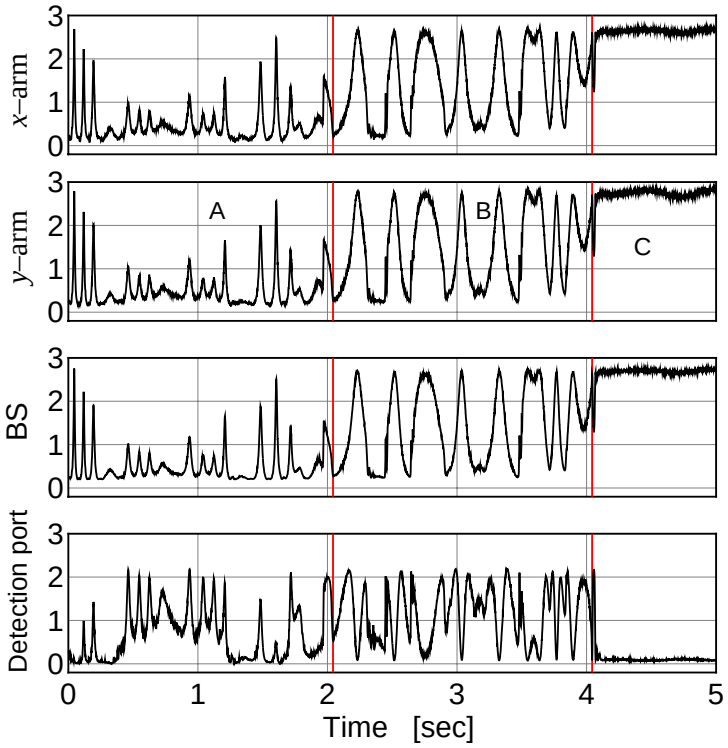

Figure 6.2: Power change in the guide lock acquisition sequence. A: Both arms cavities are locked independently with δL_x and δL_y signals. B: Recycling cavity is locked with the δl_+ signal. C: Beam-splitter is locked; all degrees of freedom are locked.

operational point, the power leaks to the detection port; the point moves along the elliptic boundary curve in the correlation diagram.

6.1.2 Guide locking scheme

One of the problems with lock acquisition is that the control signals are easily affected by the misalignment of the interferometer and misadjustment of demodulation phases; it is not easy to adjust under unlocked state. The point of guide locking scheme is to use signals which are less affected by the motions in other degrees of freedom of the interferometer, misalignment, and misadjustment of the demodulation phases. Since the noise level of the auxiliary controls signal is not good, the control system is switched to the final one step by step (Fig. 6.2 to

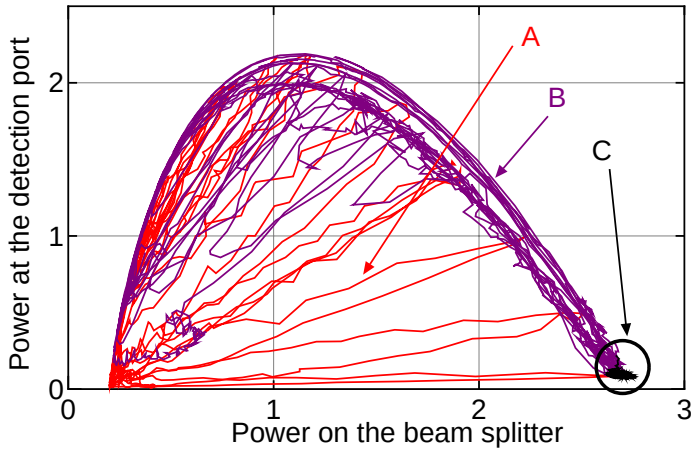

Figure 6.3: Correlation diagram in the guide lock acquisition sequence. In State A (both arm cavities are locked), the power correlation point moves in the elliptic region depending on the motion of the recycling mirror and the beam splitter. In State B, the recycling cavity is locked, and the correlation point moves along the elliptic boundary. In State C, with the whole interferometer locked, the correlation point is still at the operational point: the point of a high recycling gain and dark fringe.

Fig. 6.4) after the interferometer is locked with auxiliary control loops.

In order to lock the 3-m interferometer, at first, the arm cavities are locked with the δL_x and δL_y signals (State A). The δL_x and δL_y signals are extracted from the reflected beams on the AR surfaces of the beam splitter. The arm cavities are locked to resonate with the incident beam, though the beam splitter and the recycling mirror are not controlled. This is because the δL_x and δL_y signals are sensitive almost only to the corresponding arm cavity motions in the 3-m interferometer. In addition, we designed the servo filters of these control loops so as to be stable against the change in the sensitivities of these signals; the sensitivities of these signals change by a factor of about 20 because the light power on the beam splitter changes depending on the motions in the recycling mirror and the beam splitter.

After the arm cavities are locked, the recycling cavity is controlled with δl_+ signal (State B), and the beam splitter is controlled with δl_- signal (State C). At this stage, all degrees of the longitudinal freedom of the interferometer are

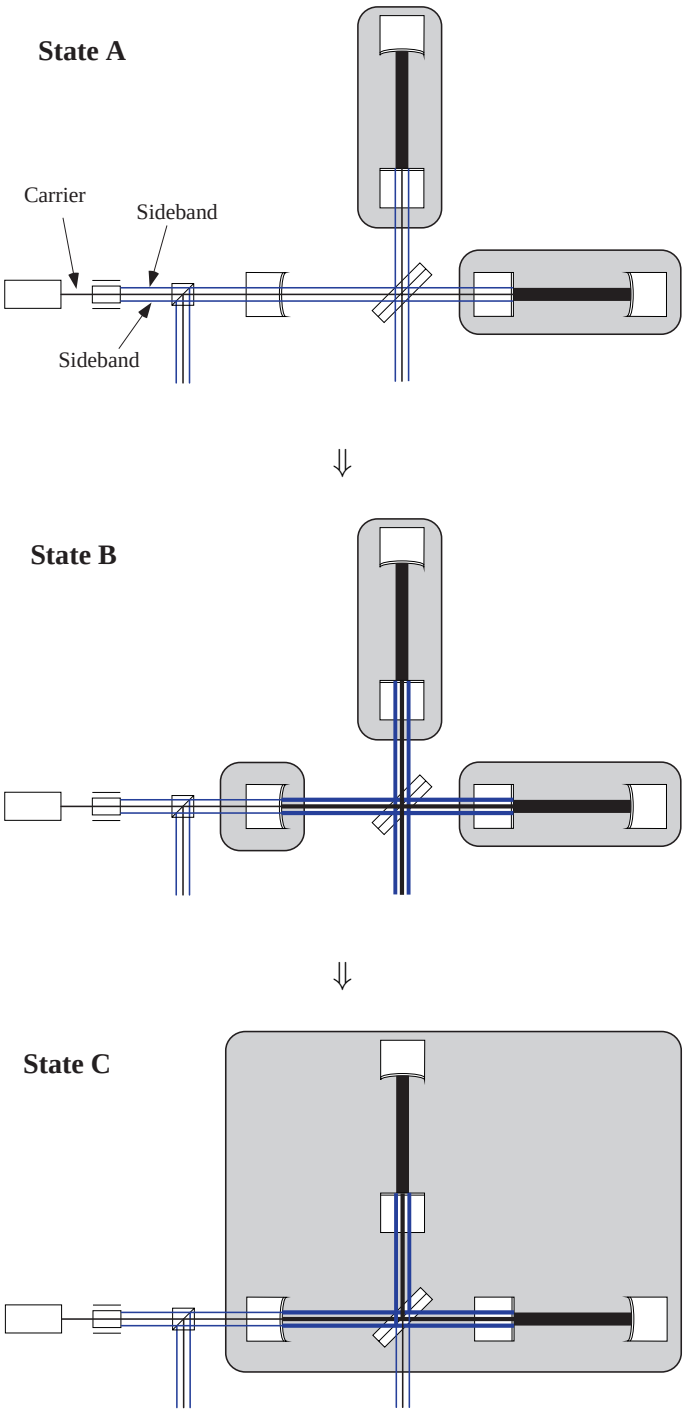

Figure 6.4: Lock acquisition sequence with the guide locking scheme. State A: both arm cavities are locked. State B: the arm and recycling cavities are locked. State C: the interferometer is locked.

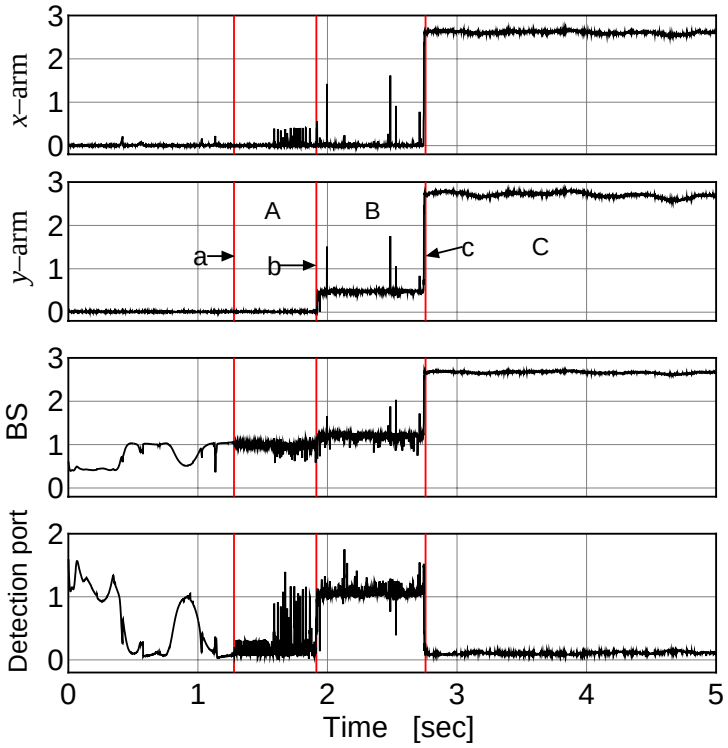

Figure 6.5: Power change in the automatic lock acquisition sequence. At the time 'a', all control loops are closed, and simultaneously, $\delta l_{\pm}$ degrees of freedom are locked for the sidebands (State A). At the time 'b' the y-arm cavity is locked for the carrier (State B); the transmission power through y-arm cavity increases. Finally, at the time 'c', the x-arm cavity is locked for the carrier (State C).

locked at the operational point. Finally, the control signals for the end mirrors are changed from δL_x and δL_y to δL_- and δL_+ with the summation amplifiers with switches (SW). Though the control loops are switched manually in our experiment, it is not difficult to automate the lock-acquisition step.

This scheme is particularly useful for the initial lock acquisition of the interferometer. The sensitivity of the interferometer is maximized when the δL_- and δL_+ signals are used to control the interferometer. However, the response of these signals is greatly affected by the misalignment of the mirrors or misadjustment of the demodulation phases. Since it is very difficult to adjust the orientation of the mirrors and the demodulation phases under the uncontrolled state, it is not

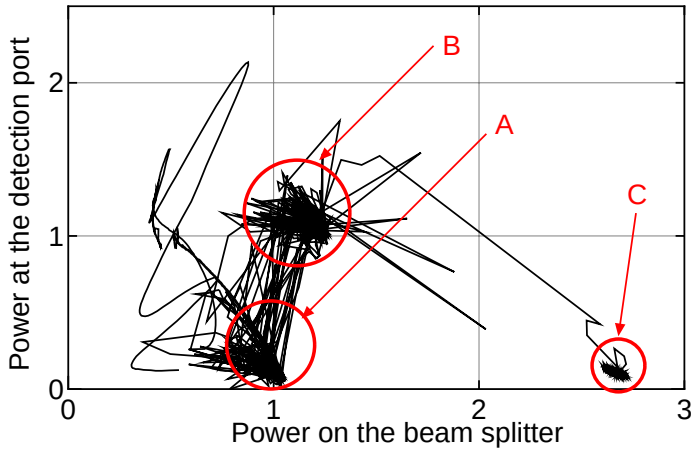

Figure 6.6: Correlation diagram in the automatic lock acquisition sequence. At State A, the detection port gets dark and the laser power on the beam splitter increases a little. At State B, the interference fringe turns to bright. Finally, all of the four degrees of freedom are locked at the operational point (State C). The interference fringe turns to dark at the detection port, and the laser power on the beam splitter increases.

easy to use the δL_- and δL_+ signals for the initial lock acquisition of the interferometer. The lock-acquisition scheme with the $\delta L_x$and δL_y signals is tolerant against the initial misalignment of the mirrors or misadjustment of the demodulation phases. By locking the interferometer with the auxiliary control loops (δL_x, δL_y) together with the δl_- and δl_+ control loops, it is possible to finely align the orientation of the mirrors of the interferometer to have a better contrast, a higher recycling gain, and a higher transmissivity through the Fabry-Perot arm cavities. The demodulation phase for each signal is also finely adjusted so as to minimize the unnecessary signals.

6.1.3 Automatic locking scheme

Once the interferometer and demodulation phases are well adjusted, the interferometer is locked by just closing the δL_-, δL_+, δl_- and δl_+ control loops without auxiliary control loops. This process has been analyzed with a computer simulation by the LIGO group [75]. Figure 6.5 to Fig. 6.7 shows the automatic lock acquisition sequence observed in the 3-m prototype interferometer.

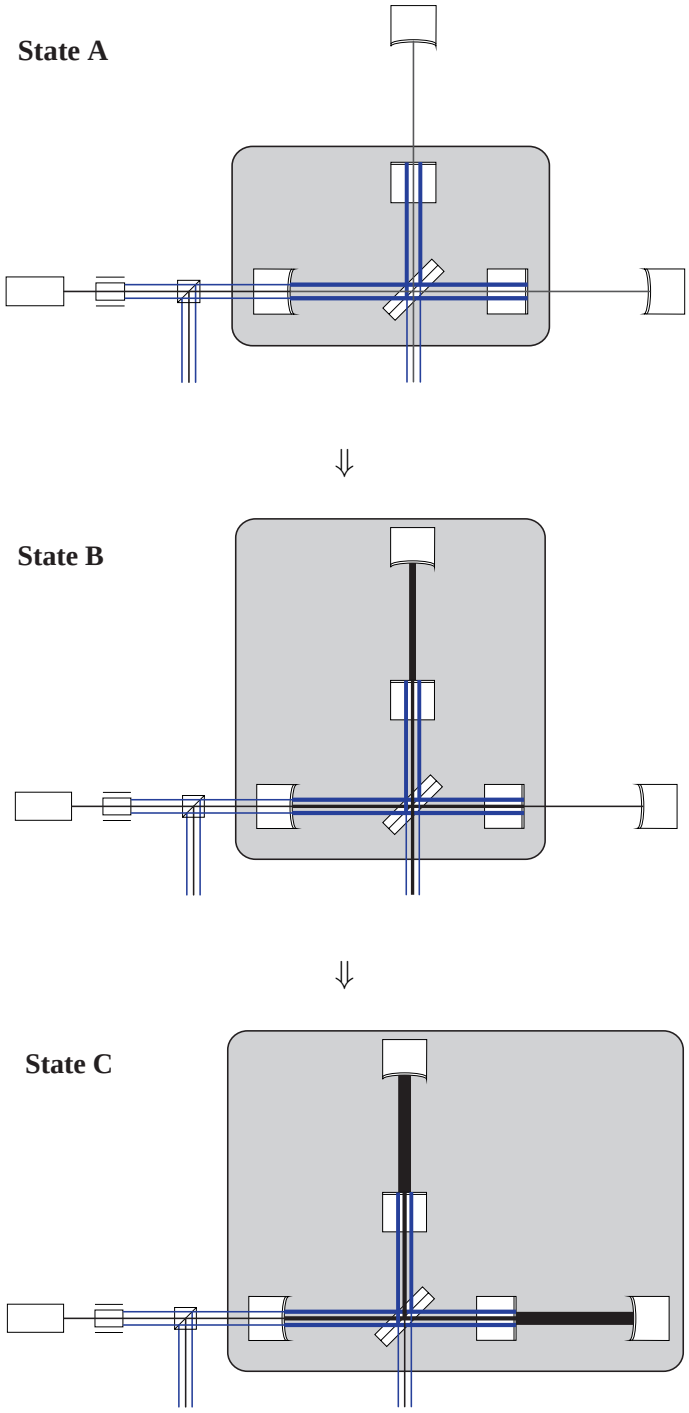

Figure 6.7: Automatic lock acquisition sequence. State A: the recycling mirror and the beam splitter is locked. State B: the power-recycled Michelson interferometer and one of the arm cavity are locked. State C: the interferometer is locked.

Table 6.1: Table of power gains. The measured gains are in a good agreement with calculated ones.

Power gain			
		Measured	Calculated
Power recycling gain	G_0	2.4	2.5
Power gain on BS	$G_{\rm BS}$	2.6	2.6

In this lock acquisition sequence, at first, the $\delta l_{\pm}$ degrees of freedom are locked (State A). At this state, the sidebands resonate with the power-recycled Michelson interferometer, while the carrier is anti-resonant with the interferometer. The detection port becomes dark and the laser power on the beam splitter increases in some extent because of the power gain of the sidebands. Next, one of the arm cavities is locked (State B); the carrier resonates with one of the arm cavities and with the recycling cavity. At this state, the interference fringe turns to bright; the carrier beams from two arms of the Michelson interferometer interfere constructively at the detection port. This is because the phase of the carrier reflected by arm cavity differs by π under resonant and anti-resonant conditions. At last, the carrier beam resonates with another arm cavity (State C); all of the four degrees of freedom ($\delta L_{\pm}$ and $\delta l_{\pm}$) are controlled and the interferometer is locked at the operational point. The interference fringe turns to dark at the detection port, and the laser power on the beam splitter increases.

Typically, the lock is acquired within a few second with the automatic locking sequence when the interferometer is well-adjusted. However, this scheme does not work well when the orientation of the mirrors and the demodulation phases are not well adjusted. In this case, we adjust the interferometer locking the interferometer with the guide locking scheme.

6.2 Operation with power recycling

The 3-m prototype interferometer is operated very stably with power recycling. In this Section, we evaluate the power-recycled interferometer: a recycling gain, stability of the operation, control loops, calibration of the error signals, residual

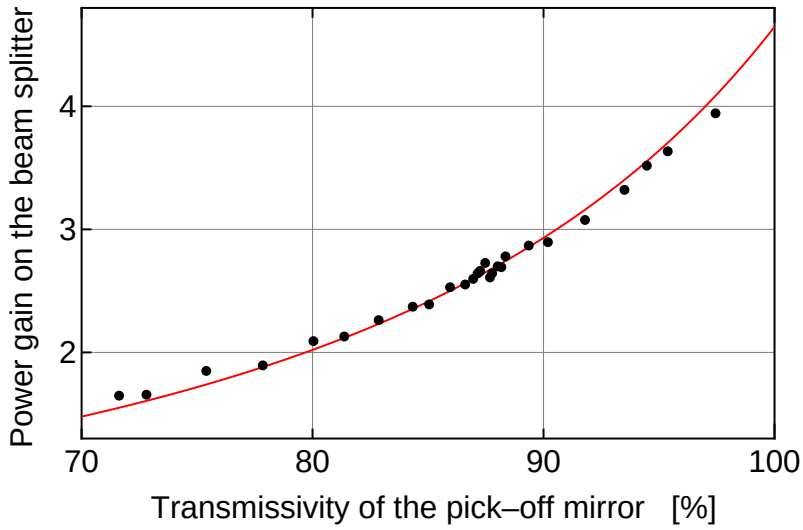

Figure 6.8: Power gain on the beam splitter as a function of the transmissivity of the pick-off. The dots are measured power gains on the beam splitter, and the solid curve is a calculated one.

RMS deviations around the operational point, and a signal gain.

6.2.1 Power-recycling gain

When the interferometer is power-recycled, the laser power in it increases by a factor called power gain. The power gain is defined as the ratio of the power with and without the recycling mirror. Especially, the power gain of the carrier beam is called power recycling gain. Since it is impossible to remove the recycling mirror keeping the interferometer in vacuum in our system, we estimate the power gain from the ratio of the power with power recycling and the power with the recycling mirror misaligned.

$$G = \frac{P_{\mathrm{PR}}}{P_{\mathrm{NR}}} = T_{\mathrm{R}} \frac{P_{\mathrm{PR}}}{P_{\mathrm{miss}}}, \tag{6.1}$$

where T_{R} is the power transmissivity of the recycling mirror, and P_{PR}, P_{NR}, and P_{miss} are the power with power recycling, without the recycling mirror, and with the recycling mirror misaligned, respectively.

We measured the power gain monitoring the laser power at three points; the powers transmitted trough the arm cavities (PD7, PD8), and the power on the

beam splitter (PD9). Since the arm cavities transmit only the carrier beam, the power gain of the transmitted beam represents the gain of the carrier, i.e., the power-recycling gain (G_0). On the other hand, the laser beam on the beam splitter is comprised of the carrier and the sidebands. Neglecting the higher-order sidebands, the power gain on the beam splitter ($G_{\rm BS}$) is written as

$$G_{\rm BS} = J_0^2(m_{\rm m})G_0 + 2J_1^2(m_{\rm m})G_1, \tag{6.2}$$

where $J_0(m_{\rm m})$ and $J_1(m_{\rm m})$ are Bessel functions, $m_{\rm m}$ is the modulation index, and G_1 is the power gain of the sidebands.

Table 6.1 shows the measured power gains together with gains calculated with the measured reflectivities and transmissivities of the optical components. Power gain on the beam splitter is also shown in Fig. 6.8, as a function of the transmissivity of the pick-off; the dots and the solid line are the measured and calculated power gains. From Table 6.1 and Fig. 6.8, we see that the measured gains are in a good agreement with calculated ones.

6.2.2 Stability of operation

Once locked, the interferometer is operated very stably. Figure 6.9 shows the power fluctuations 3-m RFPMI measured in 160 minutes from 4:40 till 7:20 in the morning.

The upper plot shows fluctuation of power gains. The vertical axis is normalized to show the power gains due to the power recycling. The lower line shows the power-recycling gain[4]. The upper line shows the power gain on the beam splitter.

The lower plot of Fig. 6.9 shows the fluctuation of the dark fringe. The vertical axis is normalized to represent the contrast. Contrast indicates the completeness of the interference. The averaged contrast in this measurement is 98.5%. In general, the contrast of a Michelson interferometer is defined by

$$C = \frac{P_{\rm max} - P_{\rm min}}{P_{\rm max} + P_{\rm min}}, \tag{6.3}$$

[4]The lower line in Fig. 6.9 is measured by monitoring the transmitted beam through the x-arm cavity (PD7). The measured recycling gain by y-arm cavity (PD8) shows almost the same line.

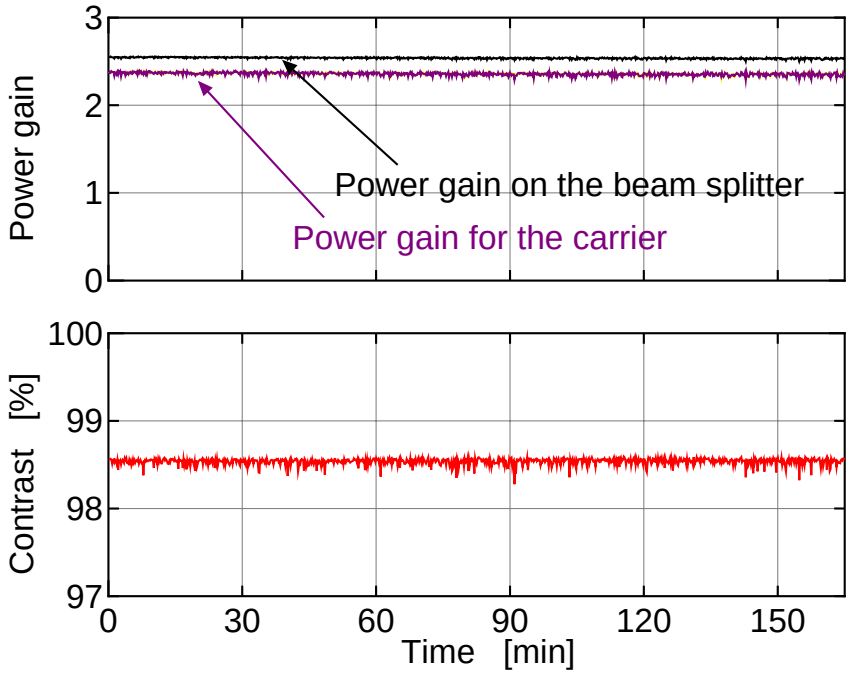

Figure 6.9: Fluctuation of the laser powers on the photo detectors in 160 minutes. The upper figure shows fluctuation of power gains. The vertical axis is normalized to show the power gain due to the power recycling. The lower figure shows the fluctuation of the dark fringe. The vertical axis is normalized to represent the contrast. The RMS fluctuation of the power gain and contrast are 0.34% and 0.038%, respectively in this 160 minutes' measurement. The interferometer is operated very stably.

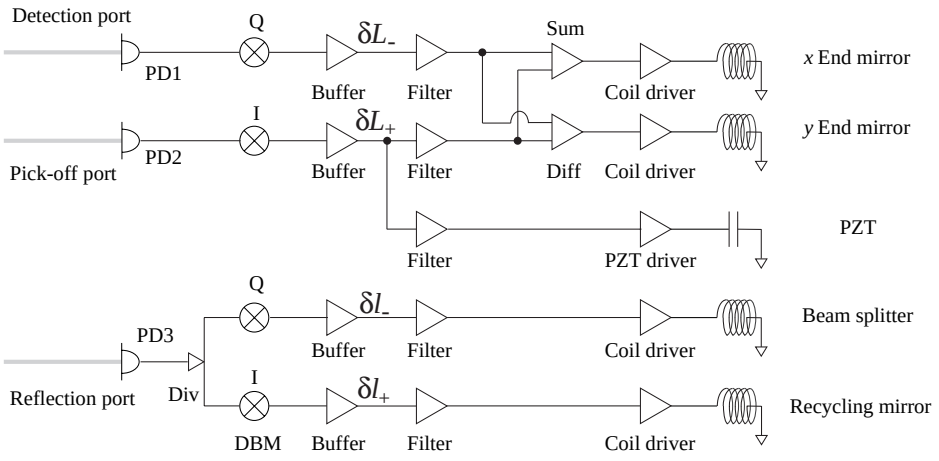

Figure 6.10: Diagram of the control system of the 3-m Fabry-Perot-Michelson interferometer. The δL_- and δL_+ signals are fed back to the actuators of the end mirrors differentially and commonly, respectively. The δL_+ signal is also used to control the frequency of the laser source. The δl_- and δl_+ signals are used to control the beam splitter and the recycling mirror, respectively.

where $P_{\rm max}$ and $P_{\rm min}$ are maximum and minimum powers, i.e. bright and dark fringe powers, respectively. These powers are usually measured by sweeping the interference fringe. In a power-recycled Michelson interferometer, however, the bright fringe power is not measured directly because the power incident on the Michelson interferometer changes depending on the interference condition. Thus, we estimated the bright fringe power with power recycling by

$$P_{\rm max} = \frac{1}{T_{\rm R}} G_{\rm BS} P_{\rm max,miss}, \tag{6.4}$$

where $P_{\rm max,miss}$ is the bright fringe power with the recycling mirror misaligned.

The RMS fluctuation of the power gain and dark fringe power are 0.34% and 2.6%, respectively in this 160 minutes' measurement. The fluctuation of 2.6% of the dark fringe power corresponds to the contrast fluctuation of 0.038%. The interferometer is operated very stably.

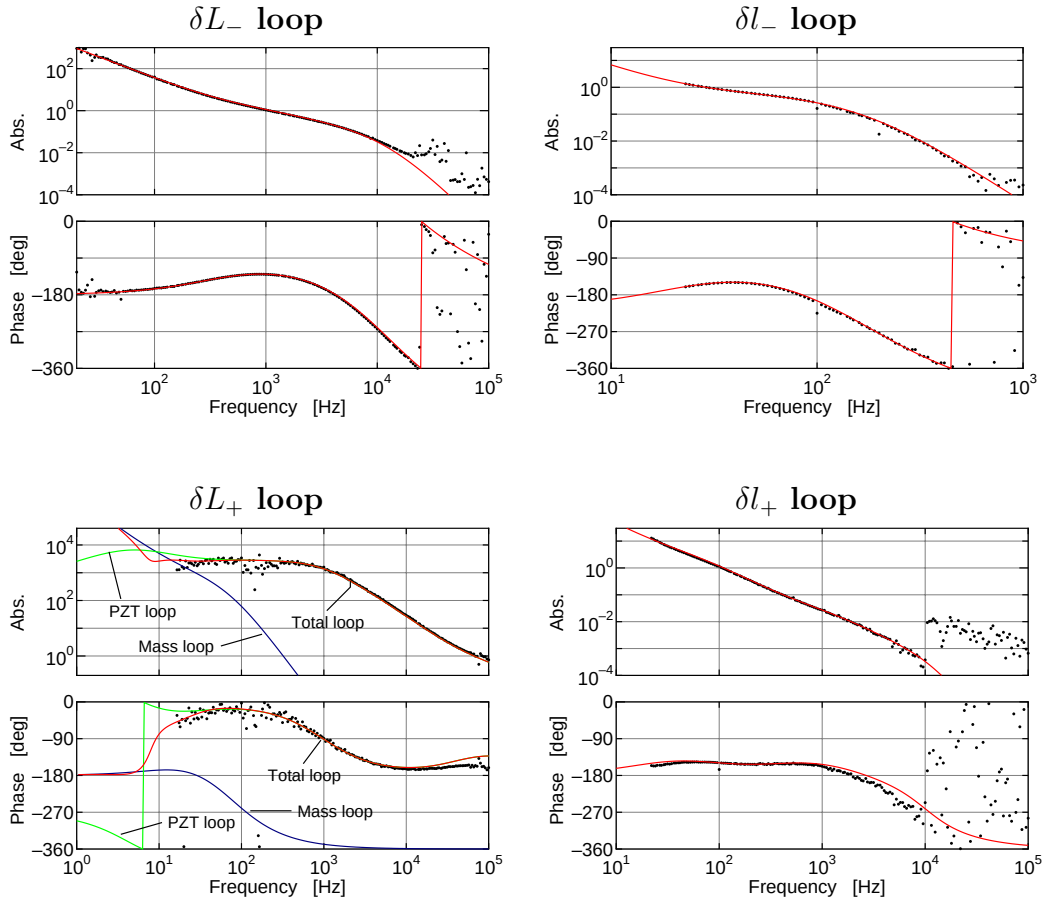

Figure 6.11: Bode diagrams of the control loops. The dots are the measured open loop transfer functions, and the solid curves are calculated open loop transfer functions from the response of the interferometer, the filter circuits, and the actuators.

6.2.3 Control system

Four degrees of freedom have to be controlled to operate a power-recycled Fabry-Perot-Michelson interferometer. In this experiment the four signals necessary for the control are obtained by frontal modulation (Chapter 4), and fed back to suitable actuators after processing through filters (Fig 6.10).

Figure 6.11 shows the bode diagrams of the measured open loop transfer functions of these four control loops. The dots are the measured open loop transfer functions, and the solid curves are calculated open loop transfer functions from

Table 6.2: Sensitivities of the signals. Control degrees of freedom and shaken mirrors for the measurement are shown together.

Signal sensitivity			
Signal	DOF	Shaken	Sensitivity
V_{DQ}	δL_-	y-FM	8.5×10^9 V/m
V_{RQ}	δl_-	BS	3.5×10^{10} V/m
V_{PI}	δL_+	y-FM	3.6×10^{10} V/m
V_{RI}	δl_+	RM	2.0×10^8 V/m

the response of the interferometer, the filter circuits, and the actuators. The δL_- signal is obtained by demodulating the output of PD1 in quadrature-phase, and fed back to the actuators of the end mirrors differentially. The unity gain frequency is 1 kHz. The δl_- signal is obtained by demodulating the output of PD3 in quadrature-phase, and used for the control of the beam splitter. The unity gain frequency of the δl_- loop is 29 Hz with a phase margin of 27 degree. The gain of this loop is cut off steeply in the frequency range above the unity gain frequency in order to prevent the noise in the δl_- signal from degrading the interferometer sensitivity. The δL_+ signal is obtained by demodulating the output of PD2 in in-phase. This signal is used to control the frequency of the laser source in a higher frequency range as well as the common control of the end mirrors in a lower frequency range. The crossover frequency of these control loops is about 10 Hz. The unity gain frequency of the δL_+ loop is 80 kHz with a phase margin of 22 degree. The recycling mirror is controlled with the δl_+ signals obtained by demodulating the output of PD3 in in-phase. The unity gain frequency of the recycling mirror control loop is 100 Hz.

The measured open loop transfer functions are in good agreement with the calculated ones. The control loops are working well as designed.

6.2.4 Calibration of signals

The sensitivities of the error signals to the deviation of the interferometer, the calibration value ([V/m]), are measured by shaking the mirrors and the beam

Table 6.3: Residual RMS deviations. These values are estimated from error signals and intensity modulated peaks.

Residual RMS deviations		
DOF	Error signal	Intensity modulation
δL_-	2.2×10^{-11} m	1.4×10^{-11} m
δl_-	1.3×10^{-9} m	2.6×10^{-9} m
δL_+	1.4×10^{-11} m	5.5×10^{-10} m
δl_+	1.7×10^{-9} m	1.7×10^{-9} m

splitter. Since the calibration values are measured with the interferometer controlled, it is necessary to consider the effect of the servo systems. The calibration value with an open loop gain of $G_{\rm open}$ is estimated as

$$\frac{\partial V}{\partial X} = \frac{V \times |1 + G_{\rm open}|}{X}, \tag{6.5}$$

where V is the measured voltage of the error signal, and X is the displacement of the shaken optical component. The displacement is estimated from the calibrated value of the actuator (Table. 5.6) and shaking voltage into the actuator driver.

The measured sensitivities of the signals are summarized in Table 6.2. These calibration values are also measured by shaking mirrors at 3 kHz[5]. The sensitivity of the δL_- and δL_+ error signals have frequency dependence. The calculated cut-off frequency of the signal is 106 kHz for δL_- and 24 kHz for δL_+.

6.2.5 Residual RMS deviations

Because of finite gains and offsets of the control system, the position of the mirrors and the frequency of the laser source have residual deviations from the ideal operational point. The residual RMS deviation is estimated from that of the error signals using the calibration values.

The RMS deviations are also measured by modulating the intensity of the input beam. The intensity modulation appears in the error signals coupling with

[5]The calibration values are estimated from the open loop transfer functions. The frequency response of these calibration values are in a good agreement with the measured value at 3 kHz and calculated frequency response.

Table 6.4: Measured and calculated signal gains.

Signal gains			
	DOF	Measured	Calculated
Signal gain	δL_-	3.0	2.9
	δl_-	4.0	3.3
	δL_+	6.9	4.6
Pole for the δL_+ signal		24 kHz	25 kHz

the RMS deviations.

$$\delta V = \frac{\delta P_\mathrm{l}}{P_\mathrm{l}} X_\mathrm{RMS}, \tag{6.6}$$

where $\delta P_\mathrm{l}/P_\mathrm{l}$ is the applied intensity modulation, which is measured by monitoring the input beam with PD9. The RMS deviations are estimated from the amplitude of the error signals at the modulation frequency of 3 kHz. The estimated RMS deviation is summarized in Table 6.3. It can be said that the RMS deviations in two estimation methods agree to each other; the differences in two estimation methods are considered to be caused from the offsets of the electronic circuits.

The residual RMS deviations of the arm cavity ($\delta L_\pm$) are about 1/50 of the line width of the resonance of the cavity. Though it is sufficient for the 3-m interferometer experiment, additional stability by a few orders is required in a gravitational wave detector. However, the required stability will be possible to realize with higher control gains in low frequency region, and moreover, with careful adjustments of the offsets. In practice, the RMS deviations do not come from the fluctuation around the operational point, but come mainly from the DC offset of the operational point.

6.2.6 Signal gain

The increase of the power inside the interferometer causes the increase of the sensitivity of the signals. The ratio of the sensitivity of the signal with and without the recycling mirror is called signal gain. We measured the signal gain

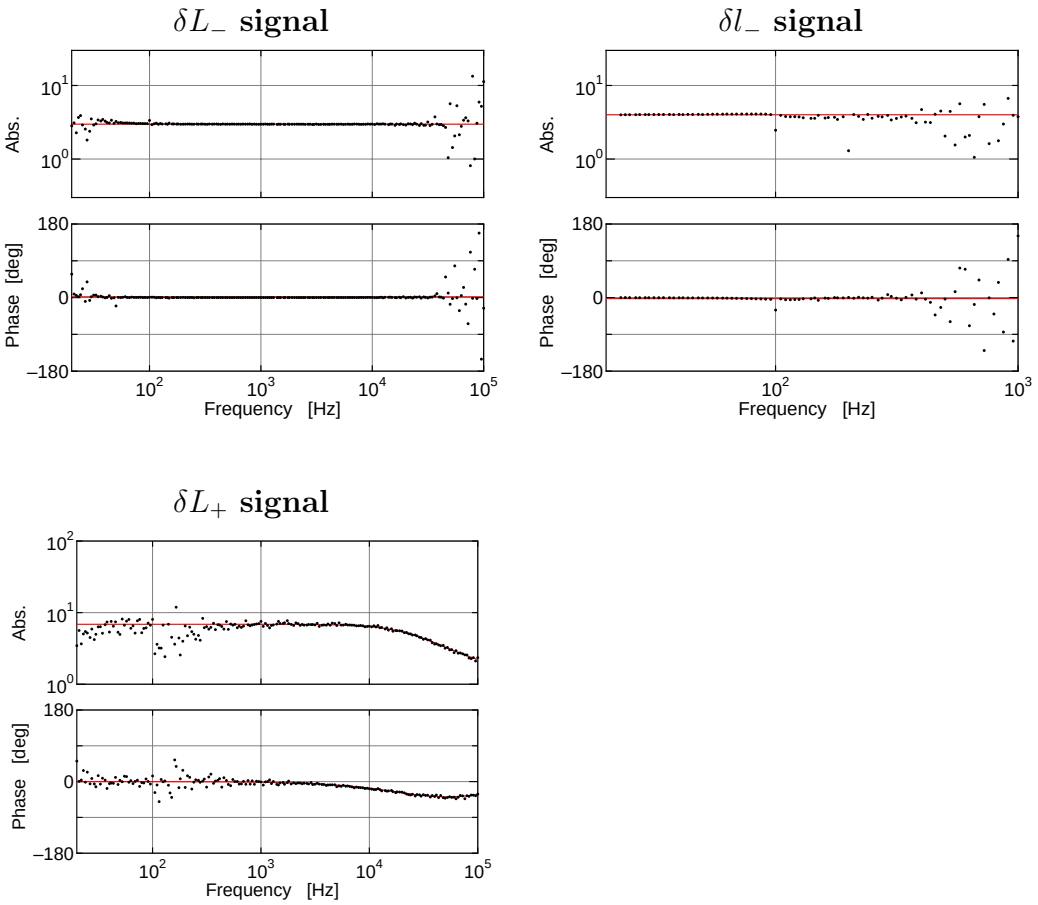

Figure 6.12: The absolute value and phase of the signal gain. Dots and the solid curves are the measured and fitted signal gains.

from open loop transfer functions[6] with power recycling and with the recycling mirror misaligned.

$$G_{\rm sig} = T_{\rm R} \frac{\left(\frac{G_{\rm open}}{G_{\rm filter}}\right)_{\rm PR}}{\left(\frac{G_{\rm open}}{G_{\rm filter}}\right)_{\rm miss}}, \tag{6.7}$$

where $G_{\rm open}$ is the open loop transfer function, and $G_{\rm filter}$ is the transfer function of the filter circuit, the gain of which is adjusted in each configuration.

Figure 6.12 shows the measured signal gains. The upper-left figure shows the signal gain of the δL_- control signal, which is extracted from the detection port. The signal gain for δL_- is described as $g_0 g_1$, the product of amplitude gains for the carrier and the sidebands. The measured signal gain of 3.0 is in a good agreement with the calculated value of 2.9. The frequency dependence of this signal is not changed with and without power recycling; the signal gain has no frequency dependence. The upper-right figure shows the signal gain of the δl_- control signal, which is extracted from the reflection port. The measured signal gain of δl_- is 4.0, and has no frequency dependence. The lower figure shows the signal gain of the δL_+ control signal, which is extracted from the pick-off port. This signal gain is 6.9, and has a pole at 24 kHz. The signal gain for the δL_+ has a frequency dependence; the cut-off frequency shifts lower with power recycling because the storage time of the δL_+ signal in the interferometer increases.

The signal gains are also estimated from the calibration values of the signals with and without power recycling. These signal gains are in good agreement with the values estimated from the open loop transfer functions.

6.3 Signal separation

One of the problems on controlling a power-recycled Fabry-Perot-Michelson interferometer is the extraction of the signal for the fluctuations of recycling cavity length, the δl_+ motion. In a conventional frontal modulation scheme, the δl_+ information is mixed by a large δL_+ information. However, with the signal separation scheme described in Section 4.4, the $V_{\rm RI}$ signal, the in-phase demodulated

[6]Note that the open loop transfer function is a product of the sensitivity of the control signal, the transfer function of the electronic circuits and the that of the actuator.

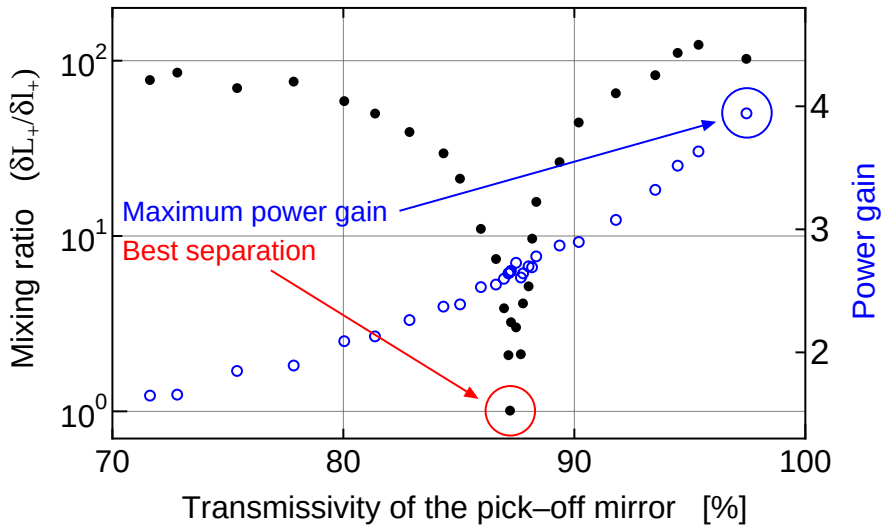

Figure 6.13: Measured signal mixing ratio and power gain as functions of the transmissivity of the pick-off. The dots represents the mixing ratio (the left axis), and the open circles represents the power gain on the beam splitter (the right axis).

signal at the reflection port, becomes sensitive only to the δl_+ motion.

6.3.1 Mixing in the $V_{\rm RI}$ signal

The signal separation is realized by setting the coupling of the recycling cavity optimal not for the carrier, but for the sidebands. In this experiment, the coupling of the recycling cavity is adjusted with the transmissivity of the pick-off, rotating the $\lambda/4$ plate.

We measured the mixing ratio of the $V_{\rm RI}$ signal with various transmissivities of the pick-off: the sensitivity ratio of the $V_{\rm RI}$ signal for δL_+ to that for δl_+ defined by

$$M_{V_{\rm RI},\delta L_+} = \frac{\left(\frac{\partial V_{\rm RI}}{\partial L_+}\right)}{\left(\frac{\partial V_{\rm RI}}{\partial l_+}\right)}. \tag{6.8}$$

Figure 6.13 shows the measured mixing ratio of the $V_{\rm RI}$ signal and the power gain on the beam splitter with various transmissivities of the pick-off. The dots represents the mixing ratio (the left axis), and the open circles represents the

Table 6.5: Measured signal sensitivity matrix without signal separation. The transmissivity of the pick-off is 98%

Mixing ratio without signal separation				
	δL_-	δl_-	δL_+	δl_+
$V_{\rm DQ}$	1	7.4×10^{-3}	2.1×10^{-2}	2.1×10^{-4}
$V_{\rm RQ}$	1.6	1	13	3.7
$V_{\rm PI}$	0.10	2.4×10^{-2}	1	3.4×10^{-2}
$V_{\rm RI}$	0.12	0.73	**130**	1

power gain on the beam splitter (the right axis). The best mixing ratio of 1.01 is obtained at the pick-off transmissivity of 87.2%. When the transmissivity is 97.4% (the maximum value in this figure), the mixing ratio is 102. Thus, the mixing ratio is improved by a factor of 100 with the adjustment of optical parameters.

As described above, the mixing ratio of δL_+ to δl_+ is about unity when the transmissivity of the pick-off is optimized. This ratio is considered to be limited by the residual motion of the interferometer as well as misadjustment of the transmissivity of the pick-off. The fluctuation of the reflectivity of the compound mirror for the sidebands causes deviation from the optimal signal-separation point, resulting in degradation of the signal-separation ratio. From the signal-mixing measurement (Fig. 6.13), the mixing ratio is estimated to be

$$M_{V_{\rm RI},\delta L_+} \simeq 705 \times \Delta R_{\rm com1}. \tag{6.9}$$

The measured RMS deviation in δl_- is 2.6×10^{-9} m. This residual motion corresponds to the fluctuation $\Delta R_{\rm com1} = 9.3 \times 10^{-4}$ (0.093%). The resultant mixing ratio is 0.7, which is in good agreement with the measured mixing ratio.

A small drift of the signal-separation point is observed during the measurement. However, it is possible to keep signal separation ratio around unity in a few tens of minutes. The mixing ratio gets worse to about 3 in a few hours, probably because of the drifts in the alignment of the interferometer.

Table 6.6: Measured signal sensitivity matrix with signal separation. The transmissivity of the pick-off is 87%

Mixing ratio with signal separation				
	δL_-	δl_-	δL_+	δl_+
$V_{\rm DQ}$	1	7.4×10^{-3}	2.3×10^{-2}	1.8×10^{-4}
$V_{\rm RQ}$	0.12	1	2.21	7.2×10^{-2}
$V_{\rm PI}$	1.7×10^{-2}	0.18	1	0.81
$V_{\rm RI}$	0.47	0.80	**1.4**	1

6.3.2 Signal sensitivity matrix

Besides the signal mixing in the $V_{\rm RI}$ signal described above, the signals mix one another. The signal mixing ratio of the signal V is defined by

$$M_{V,\delta X} = \frac{\left(\frac{\partial V}{\partial X}\right)}{\left(\frac{\partial V}{\partial X_{\rm control}}\right)}, \tag{6.10}$$

where X is one of four degrees of freedom to be controlled, and $X_{\rm control}$ is the controlled degree of freedom with the V signal[7]. Table 6.5 and 6.6 show the signal sensitives without and with signal separation, respectively. The sensitivities were measured at a frequency of 3 kHz. We see from these tables that the matrix is well-diagonalized with signal separation. Without signal separation (Table 6.5), the matrix has a large value of 130 in the $M_{V_{\rm RI},\delta L_+}$ component. While this value is decreases to 1.4 with signal separation (Table 6.6). In addition, note that the mixing of δL_+ in the $V_{\rm RQ}$ signal, which is used for the δl_- control, is improved with signal separation. The δL_+ information mixes easily into the $V_{\rm RQ}$ signal coupling with the misadjustment of the demodulation phase without the signal-separation condition. On the other hand, since RF sidebands are absent at the reflection port with the signal-separation scheme, δL_+ becomes harder to appear in the $V_{\rm RQ}$ signal even if the demodulation phase is misadjusted some extent.

[7]The four signals and the four degrees of freedom are arranged so that the table would be an unity matrix when no signal mixing is exist.

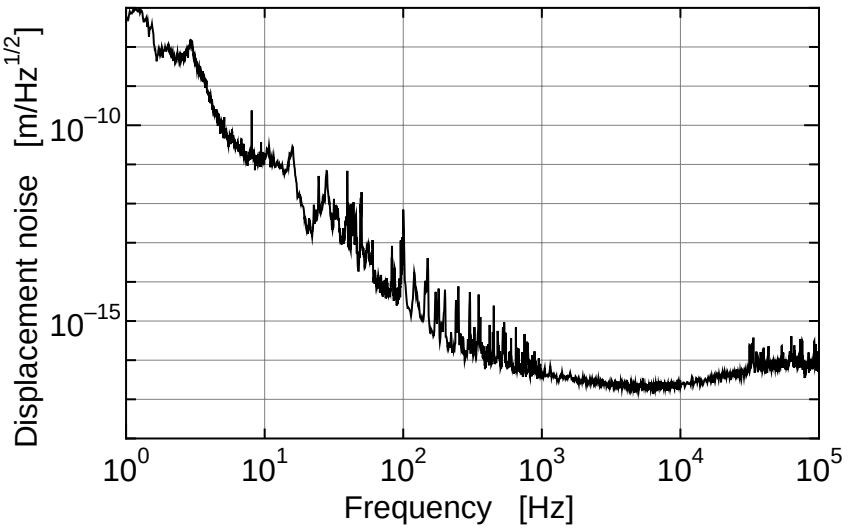

Figure 6.14: Displacement noise level of the 3-m Fabry-Perot-Michelson interferometer.

6.4 Sensitivity of the interferometer

The role of the control system is not only to keep the interferometer at the operational point, but also to operate the interferometer with a high sensitivity. Thus, the control system must be designed not to degrade the sensitivity. In this section, the sensitivity and noise sources of the 3-m prototype interferometer are described[8].

6.4.1 Displacement noise level

Figure 6.14 shows the displacement noise level, i.e., the sensitivity to δL_- deviations of the 3-m Fabry-Perot-Michelson interferometer with power recycling. The displacement noise level is estimated from the $\delta V_{\rm DQ}$ error signal, the open loop transfer function, and the calibration value shown in Table 6.2. The floor level of the displacement noise is $2 \times 10^{-17}{\rm m}/\sqrt{\rm Hz}$. The noise sources are described in the following Sections.

[8]Here, we describe the sensitivity of the interferometer by the displacement noise level. The phase fluctuation $\delta\theta$ is converted to the displacement by $\delta X = \lambda_{\rm l}\delta\theta/4\pi$, and the displacement noise level is converted to the strain sensitivity by $h = \delta L_-/L$.

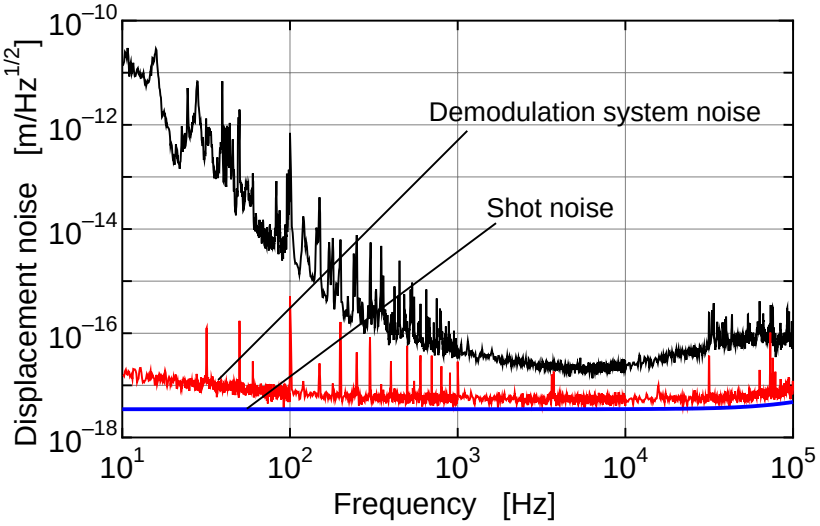

Figure 6.15: Shot-noise level and the demodulation noise level of the 3-m Fabry-Perot-Michelson interferometer.

6.4.2 Estimation of noise level

Shot noise

Shot noise is one of the fundamental noise sources in a laser interferometric gravitational wave detector. The DC photo current on the photo detector ($i_{\rm DC}$) produces a shot noise ($i_{\rm shot}$) described by

$$i_{\rm shot} = \sqrt{2ei_{\rm DC}}. \tag{6.11}$$

This shot-noise current is demodulated and appears in the error signal. The averaged photo current at the detection port detector is measured to be 0.11 mA when the interferometer is operated with power recycling. From this DC photo current, the gain of the demodulation system, and the calibration value, the shot noise level is estimated to be 3.5×10^{-18} [m/$\sqrt{\rm Hz}$]. The shot noise level is shown in Fig. 6.15 together with the displacement noise level of the 3-m prototype interferometer[9].

In practice, the demodulation system has a noise represented by the corresponding noise current $i_{\rm det}$, which is 0.26 mA for $V_{\rm DQ}$. Thus, the noise level is

[9]The shot noise level increases in a high frequency region because of the cutoff of the Fabry-Perot arm cavity at 106 kHz.

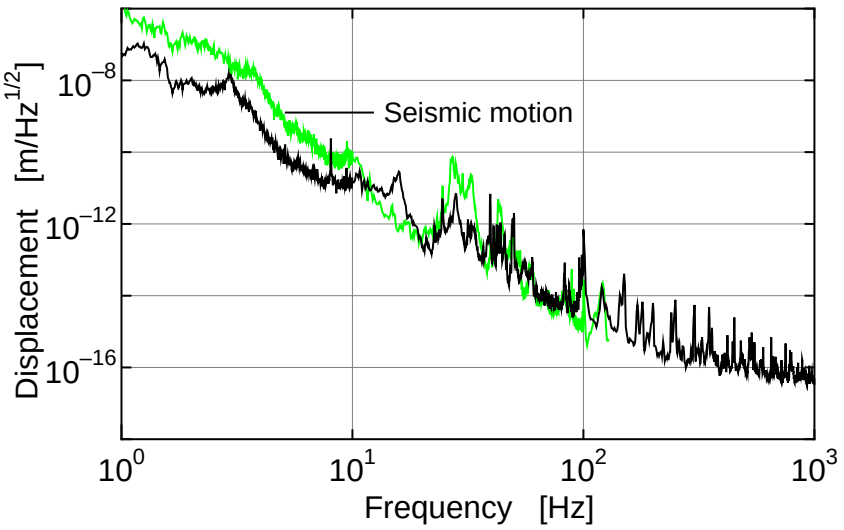

Figure 6.16: Seismic noise level of the 3-m Fabry-Perot-Michelson interferometer. The displacement noise level is limited by the seismic noise below 100 Hz.

dominated by the demodulation system noise rather than the shot noise. The noise level of the demodulation system is also shown in Fig. 6.15. The total noise level of the shot noise and demodulation system noise is calculated from Eq. (5.1), which results in the displacement noise of 6.3×10^{-18} [m/$\sqrt{\text{Hz}}$].

Seismic noise

Though the optical components are suspended and isolated from the seismic motion, the sensitivity of the interferometer is still affected by the seismic noise in a low frequency region. Figure 6.16 shows the seismic noise level together with the displacement noise level of the 3-m prototype interferometer. The seismic motion of a mirror is estimated from a measured ground motion and the seismic isolation ratio of the suspension system (Fig. 5.6). The seismic noise level of the interferometer is estimated by multiplying the motion of a mirror by $\sqrt{4}$, assuming that the motions of the four mirrors have no correlation[10]. We see that

[10]In Fig. 6.16, the displacement noise level is lower than the estimated seismic noise level. This is probably because the motions of the mirrors of the interferometer have some correlation in a low frequency region.

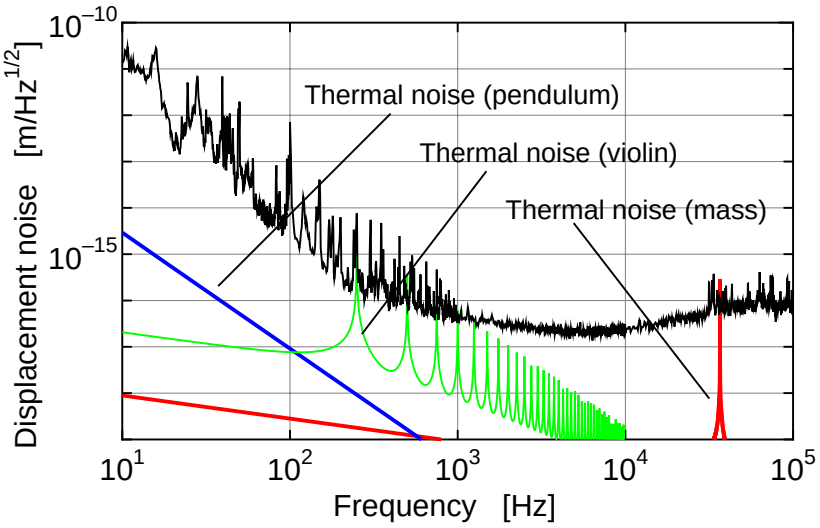

Figure 6.17: Thermal noise level of the 3-m Fabry-Perot-Michelson interferometer. The thermal noises do not affect the sensitivity of the interferometer except for the resonant frequency of the test mass (37 kHz).

the displacement noise level is limited by the seismic noise below 100 Hz from Fig. 6.16.

Thermal noise

Thermal noise is the other fundamental noise source for an interferometric gravitational wave detector. However, since the sensitivity of the 3-m prototype interferometer is not so high, the thermal noise level is lower than the sensitivity level except for the resonant frequencies of the test mass and violin modes. Figure 6.17 shows the thermal noise level. The thermal noise of the mass is calculated only for the lowest internal mode of the test mass, assuming the structure damping model. The measured Q-values are 1,600 to 27,000 for four test masses. The resonant frequency is 37 kHz, and an effective mass of 0.23 kg. The thermal noise for the pendulum is calculated with a Q-value of 1000, a resonant frequency of 1.2 Hz, and an effective mass of 0.46 kg. The resonant frequency of the lowest violin mode is calculated to be 250 Hz. The Q-value of the violin modes are assumed to be 500.

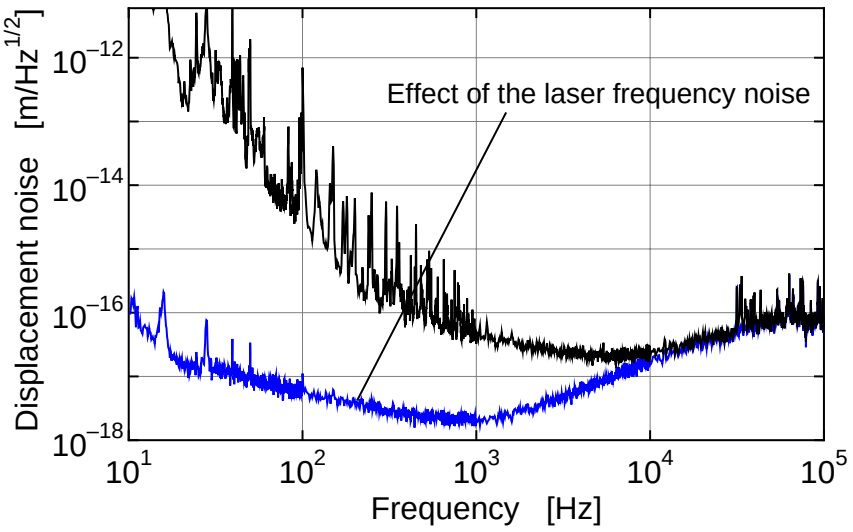

Figure 6.18: Effect of the laser frequency noise. The CMRR is about 20 in this measurement. The displacement noise level is limited by the laser frequency noise over a frequency of 10 kHz.

Laser frequency noise

A Fabry-Perot cavity is sensitive to the frequency fluctuation of the incident laser beam. Though the effect of the laser frequency noise is canceled out at the detection port if the two arms of the Michelson interferometer are symmetric, it can be a noise source for the interferometer because of the non-ideal optics. The reduction ratio of the laser frequency noise at the detection port is called CMRR (a common mode rejection ratio).

Figure 6.18 shows the effect of the laser frequency noise. The residual frequency noise with a frequency stabilization is measured by the $V_{\rm PI}$ error signal, which is sensitive to δL_+. The CMRR is about 20 in this measurement[11]. The displacement noise level is limited by the laser frequency noise over a frequency of 10 kHz.

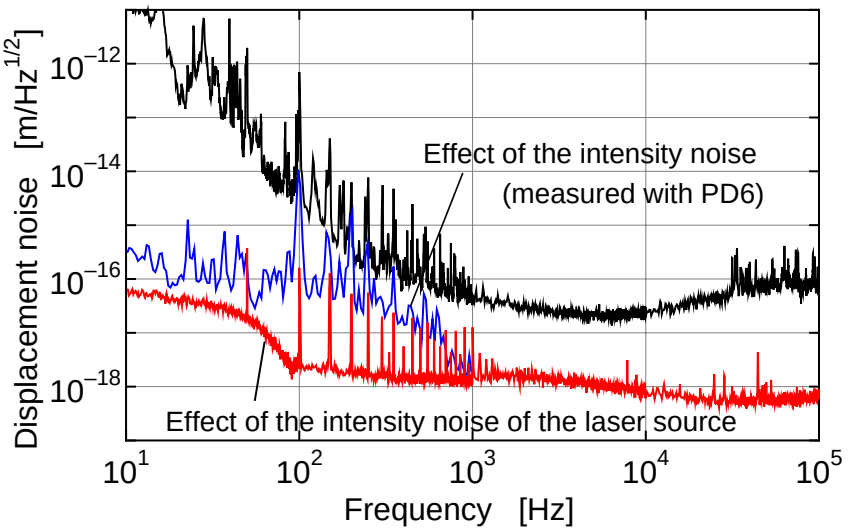

Figure 6.19: Effect of the intensity noise. The lowest curve is the effect of the intensity noise of the laser source. The middle curve is the effect of intensity noise caused by the fluctuation of power gain.

Laser intensity noise

The intensity noise of the incident laser beam can be a noise source coupling with the offset and residual motion around the operational point,

$$\delta L_{-,\mathrm{int}} = \frac{\delta P_\mathrm{l}}{P_\mathrm{l}} \Delta L_{-,\mathrm{RMS}} \quad [\mathrm{m}/\sqrt{\mathrm{Hz}}]. \tag{6.12}$$

In the 3-m prototype interferometer, the effect of intensity noise does not affect the sensitivity of the interferometer. Figure 6.19 shows the effect of the intensity noise when the residual RMS motion is 1.4×10^{-11} m (Table 6.3). The lowest curve is estimated from the intensity noise of the laser source (Fig. 5.11).

On the other hand, the middle line is the effect of intensity noise caused by the fluctuation of power gain. The intensity on the beam splitter fluctuates because of a residual longitudinal and orientation motion of the optics. This fluctuation (the fluctuation of the power gain on the beam splitter) affects the sensitivity of the interferometer in a same way as the intensity noise[12]. The fluctuation of

[11] A CMRR is a half of the mixing ratio of δL_+ into detection port signal, V_DQ; it is written by $M_{V_\mathrm{DQ},\delta L_+}/2$.

[12] Strictly, the effect of the fluctuation of the power is described by $\delta(g_0 g_1 P_\mathrm{l})/(g_0 g_1 P_\mathrm{l})$. Under

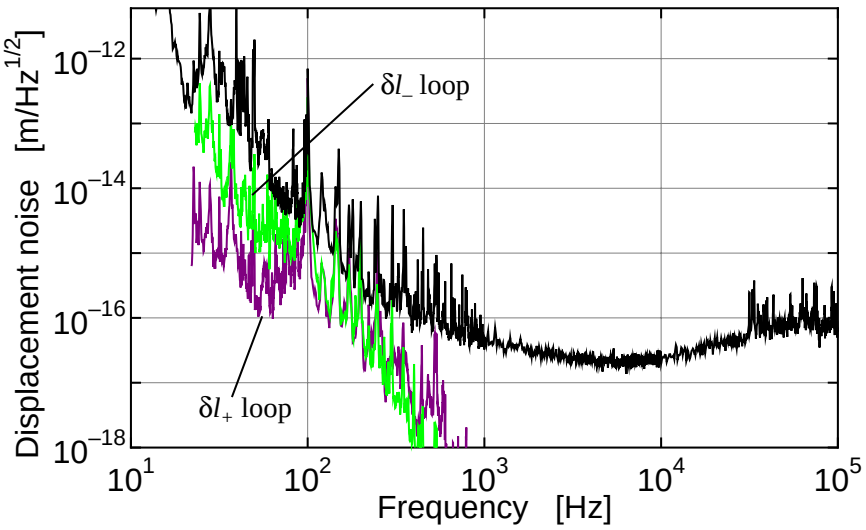

Figure 6.20: Effect of the noises introduced through the control loops.

power gain is measured with PD6, the photo detector monitoring the reflected beam on the AR surface of the beam splitter.

Excess noise introduced by control system

In general, the signal to noise ratio of the signals for the δl_- and δl_+ control loops are not so good as those for δL_- and δL_+. The excess noise can be introduced to the interferometer by controlling with these noisy signals. In other words, the beamsplitter and the recycling mirror can be shaken by feeding back noisy δl_- and δl_+ signals to the interferometer. The effect of the noise introduced by the control loop is written as

$$\delta L_{-,\delta l_\pm} = M_{V_{\rm DQ},\delta l_\pm} \left| \frac{G_{\delta l_\pm}}{1+G_{\delta l_\pm}} \right| n_{\delta l_\pm}, \tag{6.13}$$

where $G_{\delta l_\pm}$ is the open loop transfer function for δl_- or δl_+, and $n_{\delta l_\pm}$ is the displacement noise level of the signal for these control loops. Equation (6.13) shows that the gains of these loops should be designed to decrease steeply above the unity gain frequency in order to avoid the excess noise introduced through

an approximation that $g_0 \simeq g_1$, this expression is written by $\delta P_{\rm BS}/P_{\rm BS}$, which is measured with PD6.

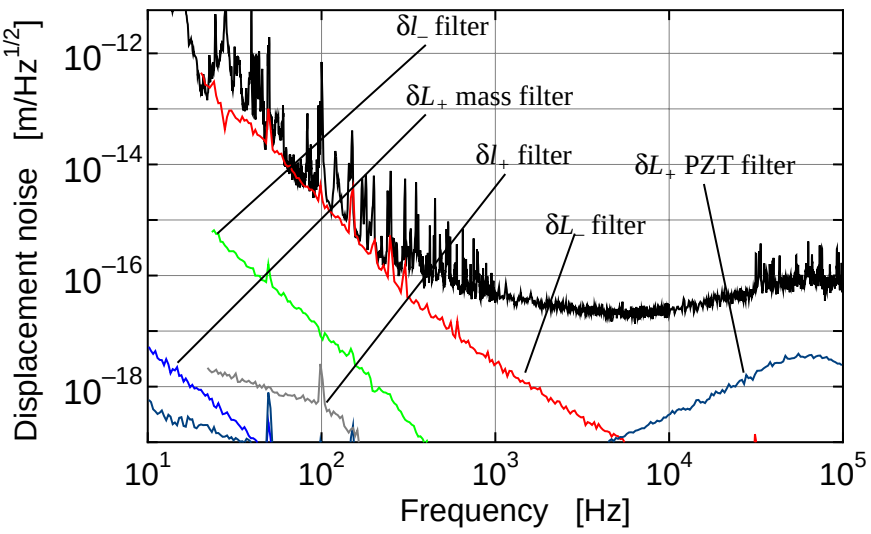

Figure 6.21: Effect of the electronic noises of the control circuits. The noise of δL_- filter is limiting the sensitivity from 60 Hz to 200 Hz.

the control loops. In particular, a severe restriction is required for the δl_- control loop[13].

The control loop for δl_- is designed to decrease steeply above the unity gain frequency in the 3-m interferometer. Thus, the excess noise introduced through the control loop is reduced lower than the displacement noise level although the control signals are affected not only by the shot noise but also by the intensity noise, the laser frequency noise, the seismic noise, and so on. Though the control loop for δl_+ is not designed to cut off steeply, the excess noise does not affect the sensitivity of the interferometer except for several resonant peaks[14].

[13]In the 3-m prototype interferometer, the shot noise level for the δl_- is 4.5×10^{-15} m/$\sqrt{\text{Hz}}$ and $M_{V_{\text{DQ}},\delta l_-} = 7.4 \times 10^{-3}$. Thus, the product of these is 3.3×10^{-17} m/$\sqrt{\text{Hz}}$. Thus, the shot noise of the δl_- control signal can limit the displacement noise level without a proper design. On the other hand, the shot noise level for δl_+ is 7.7×10^{-16} m/$\sqrt{\text{Hz}}$ and $M_{V_{\text{DQ}},\delta l_+} = 1.8 \times 10^{-4}$. The product of these is 1.4×10^{-19} m/$\sqrt{\text{Hz}}$. This noise level is much below the displacement noise level of the 3-m prototype interferometer.

[14]The noise in the δl_+ error signal is introduced also into the δL_+ signal through the control loop. However, with the signal separation scheme, the requirement would not be severe because the sensitivity for δl_+ is high enough. However, if a high stability is required for the laser frequency, or if the conventional frontal modulation scheme is used, the laser frequency stability can be limited by the noise in the δl_+ error signal.

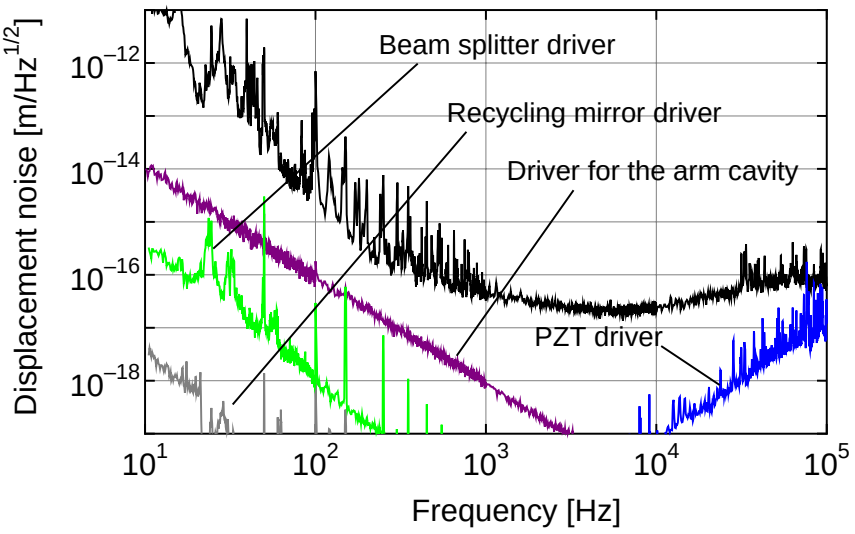

Figure 6.22: Effect of the electronic noises of the actuator drivers. The noise levels of the drivers are lower than the displacement noise level.

Electronic circuit noise

Though the electric noises are not fundamental noise sources in an interferometer, they can affect the sensitivity of the interferometer without a proper design. Thus, the control circuits should be designed carefully in a sensitive detector.

The affects of the electric noises of the filter circuits are shown in Fig. 6.21. The noise of δL_- filter is limiting the sensitivity from 60 Hz to 200 Hz. This is because we measured the displacement noise level at the error signal for δL_-; the contribution of this filter noise is reduced in the bandwidth of this control loop (< 1 kHz) by measuring the displacement noise at the feedback signal[15].

The contribution of the electric noise of the actuator driver circuits are shown in Fig 6.22. The noise levels of the drivers are lower than the displacement noise level of the 3-m interferometer.

6.4.3 Summary of noise sources

The main noise sources limiting the sensitivity of the 3-m prototype interferometer are summarized in Fig. 6.23. The floor noise level of this interferometer is $2 \times$

[15]The contribution of the filter circuit noise is reduced by the open loop gain.

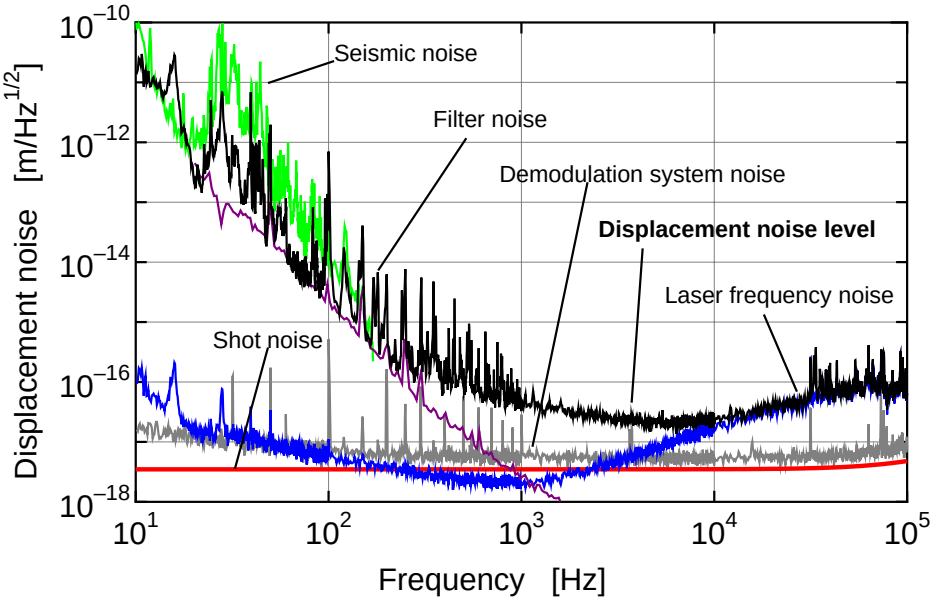

Figure 6.23: Estimated noise sources of the 3-m Fabry-Perot-Michelson interferometer. In a lower frequency range, the sensitivity is limited by the seismic noise (∼100 Hz) and the noise of the filter circuit (∼200 Hz). In a high frequency range, the sensitivity is limited by the laser frequency noise (10 kHz∼). The noise source in the middle frequency range (200 Hz∼10 kHz) is not identified. One candidate for this noise is a thermal noise at the bonding of the mirror.

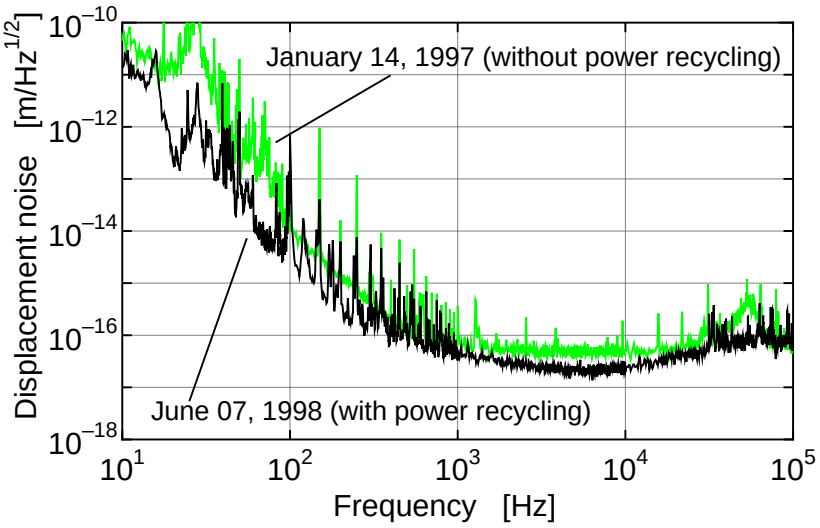

Figure 6.24: Comparison of the displacement noise levels of the 3-m prototype interferometer. The upper curve is measured displacement noise on January 14 in 1997, when power recycling is not implemented. The lower curve is the displacement noise with power recycling described in this thesis.

10^{-17} [m/$\sqrt{\text{Hz}}$], while the shot noise level is 3.5×10^{-18} [m/$\sqrt{\text{Hz}}$]. In a lower frequency range, the sensitivity is limited by the seismic noise ($\sim$100 Hz) and the noise of the filter circuit ($\sim$200 Hz). In a high frequency range, the sensitivity is limited by the laser frequency noise (10 kHz$\sim$). The noise source in the middle frequency range (200 Hz$\sim$10 kHz) is not identified. One candidate for this noise is a thermal noise at the bonding of the mirror.

Figure 6.24 shows the displacement noise levels of the 3-m prototype interferometer. The lower curve shows the displacement noise level described in this thesis. The upper one shows the displacement noise measured on January 14 in 1997 when power recycling was not implemented to the interferometer [76].

The noise level is reduced in all frequency range because of the following improvements.

- $\sim$100 Hz: The reduction of seismic motion. The interferometer was moved to a new building. The seismic noise level is reduced by about 10 times.
- 100 Hz$\sim$1 kHz: The optimization of control system. The design of the control system is improved.

- 1 kHz∼10 kHz: The effect of power recycling. Before the implementation of power recycling, the floor sensitivity level is limited by the shot noise and demodulation system noise. With power recycling, both of these noises are improved.

- 10 kHz∼: The improvement of the frequency stabilization loop. The control loop for δL_+ is improved to have larger gain and phase margin.

The displacement noise level is improved with power recycling and other improvements in the 3-m prototype interferometer, though we could not reach the shot noise level of the power-recycled interferometer.

Chapter 7

Discussion and conclusion

7.1 Results and discussions

We have implemented power recycling on a 3-m prototype interferometer, and developed the control system. This is the first demonstration of power recycling on a Fabry-Perot-Michelson interferometer with suspended optics.

Lock acquisition

Two different schemes are used to lock the interferometer: a guide locking scheme and an automatic locking scheme. The guide locking scheme is tolerant against the initial misadjustment of the interferometer, while it is simple to lock with the automatic locking scheme. The observed steps of automatic locking verifies the computer-simulated results in the LIGO group.

The realized recycling gain is rather low compared with that of a real detector in which the gain is designed to be over 10. The lock acquisition of the interferometer will become hard with a high recycling gain, because the gain of the control system changes largely on each step of lock acquisition. Thus it is necessary to test lock acquisition with a high recycling gain. However the interferometer should have a higher quality optics, and clean environment to keep the quality in order to realize a high recycling gain[1].

[1]The recycling gain of 12 is realized with a 20-m prototype interferometer in NAO. The interferometer is locked with the guide locking scheme [28].

Demonstration of power recycling

Power recycling is demonstrated with this prototype interferometer. The realized power gain is in a good agreement with the calculated one; the maximum power gain is about 4. The control system is working well as designed, and the interferometer is operated very stably over several hours. We also see the signal gain due to power recycling, i.e., increase of the signal sensitivity to the fluctuation of the interferometer.

Signal separation

We have invented a new signal-separation scheme and verified it experimentally. The control signals are separated with a proper adjustment of the optical parameters of the interferometer; the signal-separation condition is realized when the RF sidebands are absent at the reflection port,$R_{\rm rec1} = 0$. In this experiment, the transmissivity of the pick-off inside the power-recycling cavity is adjusted so as to eliminate the RF sidebands at the reflection port. The mixing ratio of unnecessary signal ($\delta\Phi_+$) to the recycling mirror control signal ($\delta\phi_+$) is improved by a factor of 100 with this scheme. The best separation ratio is limited by the length and the alignment fluctuation of the interferometer.

Though the signal separation is realized by adjusting the transmissivity of the pick-off, the transmissivity at the best separation is not exactly the same as the calculated one. The difference of the calculated transmissivity and that at the best separation ratio is about 4 %. This disagreement would be caused by the measurement errors of the optical parameters of the interferometer.

Displacement noise level

We have measured the displacement noise level of this prototype interferometer and estimated the level of main noise sources. The floor level of the displacement noise is 2×10^{-17} [m/$\sqrt{\rm Hz}$]. In a lower frequency range, the sensitivity is limited by the seismic noise ($\sim$100 Hz) and the noise of the filter circuit ($\sim$200 Hz). In a high frequency range, the sensitivity is limited by the laser frequency noise (10 kHz$\sim$).

Power recycling is a technique to improve the shot noise level of the interfer-

ometer. However, we could not confirm the improvement of the shot noise level with power recycling because of other noises. The floor level is estimated to be limited by a noise due to the bonding of the mirror; the mirrors are attached to aluminum test masses in this experiment. This noise level will be improved by replacing the mirrors of the interferometer to monolithic mirrors.

7.2 Power recycling in a real detector

Though we have achieved almost all of the purposes of this experiment on power recycling, further investigations and improvements are necessary for a real interferometric gravitational wave detector. The following problems are under investigation in several groups for gravitational wave detection.

Instrument to adjust the optical parameters

In this experiment, we use a pick-off comprised of a wave plate and polarizers in the recycling cavity; this pick-off is convenient to test the signal separation scheme because it has a wide adjustable range. However, this pick-off will not be used in a real interferometer. This is because a wave plate for a beam with a large diameter and high power is required in a real interferometer. In addition, the wavefront distortion at the wave plate will not be negligible for a high recycling gain.

Instead of the pick-off with a wave plate, it is proposed to use a pick-off plate which has an angular dependence in the transmissivity [77]. In addition, it is possible to tune the parameter with an asymmetry by motorized stages of mirror suspensions.

Quality of optics

In order to realize a high power recycling gain, the requirement for the quality of the optics becomes quite severe because the recycling gain is limited by the losses in the interferometer. Though the finesse of the arm cavities is not so high in an interferometer with long baseline, the loss of each mirror is required to be less than a few tens of ppm. In addition, such a low-loss mirror coating must

be realized in a large area (over a diameter of a few tens of centimeters) because the beam has a large diameter in a large-scale interferometer. Currently, a ppm-class of mirror loss has been produced and tested only with small mirrors (a few centimeter in diameter) [78].

Moreover, a high accuracy is required for the surface shape of the mirrors. In a large-scale interferometer, the curvatures of the mirrors are very large to realize a stable arm cavity with a mirrors as small as possible. In particular, the recycling mirror must have an extremely large curvature (a few tens to a hundred kilometers).

Alignment control

In an interferometer with long baseline, a hard requirement is set for the orientation of the optics because only a small angular fluctuation causes a large motion of the beam spot on a mirror. Thus, the automatic alignment system is indispensable. Though the alignment control systems have been tested with a simpler optical configurations or with fixed-mirror interferometers [23, 79, 80, 81], the alignment control system has not tested on a suspended Fabry-Perot-Michelson interferometer with power recycling. Similarly to the length control signals described in this thesis, the signals for alignment control will mix to each other with power recycling. In particular, the alignment signal for the recycling mirror is easily mixed with other signals.

7.3 Conclusion

We have demonstrated power recycling on a 3-m prototype interferometer, a Fabry-Perot-Michelson interferometer with suspended optics. This demonstration solves the non-obvious problem of lock acquisition. In addition, we have invented a new signal-separation scheme and verified it experimentally. This scheme will relax the requirement for the design of the control system of power-recycled interferometer. The next step of the investigation on this interferometer will be the improvement of the noise level to see the shot noise.

References

[1] C. W. Misner, K. S. Thorne, and J. A. Wheeler, *Gravitation*, W. H. Freeman and Company (1973).

[2] B. F. Schutz, *A first course in general relativity*, Cambridge University Press (1985).

[3] K. S. Thorne, *Gravitational radiation*, in: *Three hundred years of gravitation* p. 330-458, eds: S. Hawking and W. Israel, Cambridge University Press (1987).

[4] R. A. Hulse and J. H. Taylor, Astrophysical Journal 195 (1975) L51.

[5] J. H. Taylor and J. M. Weisberg, Astrophysical Journal 345 (1989) 434.

[6] J. H. Taylor, *Testing relativistic gravity with binary and millisecond pulsars* in: *General relativity and gravitation* p. 287-294, eds: R. J. Gleiser, C. N. Kozameh, and O. M. Moreschi, Institute of Physics (1993).

[7] J. Weber, Physical Review 117 (1960) 306.

[8] J. Weber, Physical Review Letters 22 (1969) 1320.

[9] R. Weiss, *Electromagnetically coupled broadband gravitational antenna*, Quarterly Progress Report of the Research Laboratory of Electronics of the Massachusetts Institute of Technology 105 (1972) 54.

[10] G. E. Moss, L. R. Miller, and R. L. Forward, Applied Optics 10 (1971) 2495.

[11] A. Abramovici, W. E. Althouse, R. W. P. Drever, Y. Gürsel, S. Kawamura, F. J. Raab, D. Shoemaker, L. Sievers, R. E. Spero, K. S. Thorne, R. E. Vogt, R. Weiss, S. E. Whitcomb and M. E. Zucker, Science 256 (1992) 325.

[12] The VIRGO collaboration, VIRGO Final Design Report (1997).

[13] K. Danzmann, H. Lück, A. Rüdiger, R. Schilling, M. Schrempel, W. Winkler, J. Hough, G. P. Newton, N. A. Robertson, H. Ward, A. M. Campbell, J. E. Logan, D. I. Robertson, K. A. Strain, J. R. J. Bennett, V. Kose, M. Kühne, B. F. Schutz, D. Nicholson, J. Shuttleworth, H. Welling, P. Aufmuth, R. Rinkleff, A. Tünnermann and B. Willke, Proposal for a 600m Laser-Interferometric Gravitational Wave Antenna, Max-Planck-Institut für Quantenoptik Report 190, Garching (Germany) (1994).

[14] K. Tsubono, 300-m Laser Interferometer Gravitational Wave Detector (TAMA300) in Japan, in: *Gravitational Wave Experiments* p. 112-114, eds: E. Coccia, G. Pizzella, and F. Ronga, World Scientific (1995) .

[15] R. W. P. Drever, Fabry-Perot cavity gravity-wave detectors, in: *The detection of gravitational waves* p. 306-328, ed: D. G. Blair, Cambridge University Press (1991) .

[16] C. N. Man, D. Shoemaker, M. Pham Tu and D. Dewey, Physics Letters A 148 (1990) 8.

[17] K. A. Strain and B. J. Meers, Physical Review Letters 66 (1991) 1391.

[18] P. Fritschel, D. Shoemaker and R. Weiss, Applied Optics 31 (1992) 1412.

[19] M. W. Regehr, *Signal Extraction and Control for an Interferometric Gravitational Wave Detector*, Ph. D thesis, California Institute of Technology (1995).

[20] M. W. Regehr, F. J. Raab and S. E. Whitcomb, Optics Letters 20 (1995) 1507.

[21] J. A. Giaime, *Studies of Laser Interferometer Design and a Vibration Isolation System for Interferometric Gravitational Wave Detectors*, Ph. D thesis, Massachusetts Institute of Technology (1995).

[22] D. Sigg, N. Mavalvala, J. Giaime, P. Fritschel, and D. Shoemaker, Applied Optics 37 (1998) 5687.

[23] D. Babusci, H Fang, G. Giordano, G. Matone, L. Matone and V. Sannibale, Physics Letters A 226 (1997) 31.

[24] D. Schnier, J. Mizuno, G. Heinzel, H. Lück, A. Rüdiger, R. Schilling and M. Schrempel, W. Winkler and K. Danzmann, Physics Letters A 225 (1997) 210.

[25] P. Fritschel, G. González, B. Lantz, P. Saha, and M. Zucker, Physical Review Letters 80 (1998) 3181.

[26] S. Moriwaki and the TAMA collaboration, in: *Gravitational Wave Detection* p. 281-286, eds. K. Tsubono, M.-K. Fujimoto and K. Kuroda, Universal Academy Press (1997).

[27] F. J. Raab, private communication (1997).

[28] S. Sato, Ph. D thesis, The Graduate University for Advanced Studies (1998).

[29] G. Heinzel, K. A. Strain, J. Mizuno, K. D. Skeldon, B. Willke, W. Winkler, R. Schilling, A. Rüdiger, and K. Danzmann, Physical Review Letters 81 (1998) 5493.

[30] K. Kawabe, S. Nagataki, M. Ando, K. Tochikubo, N. Mio and K. Tsubono, Applied Physics B 62 (1996) 135.

[31] K. Kawabe, *Development of a 3-m Fabry-Perot-Michelson interferometer*, Ph.D thesis, University of Tokyo (1998).

[32] M. Ando, K. Arai, K. Kawabe, K. Tsubono, Physics Letters A 248 (1998) 145.

[33] M. Ando, K. Kawabe and K. Tsubono, Physics Letters A 237 (1997) 13.

[34] T. Nakamura, in: *Detection of gravitational waves* (in Japanese) p. 1-166, eds: T. Nakamura, N. Mio, M. Ohashi, Kyoto University Academy Press (1998).

[35] Kip S. Thorne, in: *Proceedings of the Snowmass 95 Summer Study on Particle and Nuclear Astrophysics and Cosmology*, eds: E. W. Kolb and R. Peccei, World Scientific (1995).

[36] P. Bender, A. Brillet, I. Ciufolini, A. M. Cruise, C. Cutler, K. Danzmann, F. Fidecaro, W. M. Folkner, J. Hough, P. McNamara, M. Peterseim, D. Robertson, M. Rodrigues, A. Rüdiger, M. Sandford, G. Schäfer, R. Schilling, B. Schutz, C. Speake, R. T. Stebbins, T. Sumner, P. Touboul, J.-Y. Vinet, S. Vitale, H. Ward, W. Winkler, *LISA Pre-Phase A Report Second Edition* (1998).

[37] P. Astone, M. Bassan, P. Bonifazi, P.Carelli, M. G. Castellano, G. Cavallari, E. Coccia, C. Cosmelli, V. Fafone, S. Frasca, E. Majorana, I. Modena, G. V. Pallottino, G. Pizzella, P. Rapagnani, F. Ricci, and M. Visco, Physical Review D 47 (1993) 362.

[38] E. Mauceli, Z. K. Geng, W. O. Hamilton, W. W. Johnson, S. Merkowitz, A. Morse, B. Price, and N. Solomonson, Physical Review D 54 (1996) 1264.

[39] D. G. Blair, I. S. Heng, E. N. Ivanov, F. van Kann, N. P. Linthorne, M. E. Tobar, and P. J. Turner, in: *Gravitational Wave Experiments* p. 144-160, eds: E. Coccia, G. Pizzella, and F. Ronga, World Scientific (1995).

[40] P. Astone, M. Bassan, P. Bonifazi, F. Bronzini, M. G. Castellano, E. Coccia, C. Cosmelli, V. Fafone, S. Frasca, E. Majorana, I. Modena, G. V. Pallottino, G. Pizzella, P. Rapagnani, F. Ricci, and M. Visco, Europhysics Letters 16 (1991) 231.

[41] M. Cerdonio, L. Franceschini, G. Fontana, R. Mezzena, S. Paoli, G. A. Prodi, S. Vitale, J. P. Zendri, M. Biasotto, M. Lollo, F. Bronzini, R. Macchietto, G. Maron, A. Ortolan, M. Strollo, G. Vedovato, M. Bonaldi, P. Falferi, E. Cavallini, P. L. Fortini, E. Montanari, L. Taffarello, A. Colombo, D. Pascoli, B. Tiveron, in: *Gravitational Wave Experiments* p. 176-194, eds: E. Coccia, G. Pizzella, and F. Ronga, World Scientific (1995).

[42] P. F. Michelson, L. Mann, R. Penny, J. Henderson, D. McKenzie, C. Zhou, in: *Gravitational Wave Experiments* p. 195-200, eds: E. Coccia, G. Pizzella, and F. Ronga, World Scientific (1995).

[43] T. Suzuki, in: *Gravitational Wave Experiments* p. 115-127, eds: E. Coccia, G. Pizzella, and F. Ronga, World Scientific (1995).

[44] N. Kondo, *Disk-type resonant antenna with a laser transducer for monitoring gravitational waves*, Ph. D thesis, University of Tokyo (1998).

[45] W. W. Johnson and S. M. Merkowitz, Physical Review Letters 70 (1993) 2367.

[46] S. M. Merkowitz and W. W. Johnson, Physical Review D 53 (1996) 5377.

[47] V. B. Braginsky, and M. E. Gertsenshtein, Soviet Physics — JETP Letters 5 (1967) 287.

[48] L. B. Iess, B. Bertotti, G. Giampieri, A. Vecchio, R. Ambrosini, G. Comoretto, Y. Koyama, and A. Messeri, *Search for massive coalescing binaries with the spacecraft ULYSSES*, in: *Gravitational wave experiments* p. 64-69, eds: E. Coccia, G. Pizzella, F. Ronga, World Scientific (1995).

[49] B. Bertotti, R. Ambrosini, J. W. Armstrong, S. W. Asmar, G. Comoretto, G. Giampieri, L. Iess, Y. Koyama, A. Messeri, A. Vecchio, and H. D. Wahlquist, Astronomy and Astrophysics 296 (1995) 13.

[50] M. V. Sazhin, Soviet Astronomy 22 (1978) 36.

[51] S. Detweiler, Astrophysical Journal 234 (1979) 1100.

[52] M. P. McHugh, G. Zalamansky, and F. Vernotte, Physical Review D 54 (1996) 5993.

[53] S. Miyoki, *Development of a 100-meter Delay-Line Laser Interferometer*, Ph. D thesis, University of Tokyo (1996).

[54] C. M. Caves, Physical Review D 23 (1981) 1693.

[55] N. Mio, in: *Technical investigation of gravitational wave antennas* (in Japanese), eds: N. Mio, M. Ohashi, (1992).

[56] P. R. Saulson, Physical Review D 42 (1990) 2437.

[57] A. Gillespie, and F. Raab, Physics Letters A 178 (1993) 357.

[58] A. Gillespie, and F. Raab, Physics Letters A 190 (1994) 213.

[59] T. Uchiyama, D. Tatsumi, T. Tomaru, M. E. Tobar, K. Kuroda, T. Suzuki, N. Sato, A. Yamamoto, T. Haruyama, T. Shintomi, Physics Letters A 242 (1998) 211.

[60] D. Shoemaker, R. Schilling, L. Schnupp, W. Winkler, K. Maischberger, and A. Rüdiger, Physical Review D 38 (1988) 423.

[61] M. A. Barton and K. Kuroda, Review of Scientific Instruments 65 (1994) 3775.

[62] M. A. Barton, N. Kanda, and K. Kuroda, Review of Scientific Instruments 67 (1996) 3994.

[63] A. Rüdiger, R. Schilling, L. Schnupp, W. Winkler, H. Billing, and K. Maischberger, Opt. Acta 28 (1981) 641.

[64] F. Barone, E. Calloni, L.Di Fiore, A. Grado, P. Hello, L. Milano, G. Russo, Physics Letters A 217 (1996) 90.

[65] K. D. Skeldon, K. A. Strain, A. I. Grant, and J. Hough, Review of Scientific Instrument 67 (1996) 2443.

[66] A. Araya, N. Mio, K. Tsubono, K. Suehiro, S. Telada, M. Ohashi, and M.-K. Fujimoto, Applied Optics 36 (1997) 1446.

[67] A. Telada, *Development of a Mode Cleaner for a Laser Interferometer Gravitational Wave Detector*, Ph. D thesis, The Graduate University for Advanced Studies (1997).

[68] N. Mio, in: *Detection of gravitational waves.* (in Japanese) p. 197-229, eds: T. Nakamura, M. Mio, M. Ohashi, Kyoto University Academy Press (1998).

[69] B. Caron, A. Dominjon, R. Flaminio, F. Marion, L. Massonnet, R. Morand, B. Mours, D. Verkindt and M. Yvert, Nuclear Instruments and Methods in Physics Research A 360 (1995) 375.

[70] R. Flaminio and H. Heitmann, Physics Letters A 214 (1996) 112.

[71] K. Tochikubo, *Alignment control of a Fabry-Perot cavity.* (in Japanese), Master thesis, University of Tokyo (1996).

[72] K. Arai, private communication (1998).

[73] A. Araya, *Optical Mode Cleaner for the Interferometric Gravitational wave Detector.* Ph.D thesis, University of Tokyo (1994).

[74] S. Moriwaki, in: *Technical investigation of gravitational wave antennas* (in Japanese) p. 222-233, eds: N. Mio, M. Ohashi (1992).

[75] L. Sievers, private communication (1997).

[76] M. Ando, *Control of a Fabry-Perot-type laser interferometric gravitational wave detector.* (in Japanese), Master thesis, University of Tokyo (1996).

[77] Discussions in the TAMA group (1998).

[78] N. Uehara, A. Ueda, K. Ueda, H. Sekiguchi, T. Mitake, K. Nakamura, N. Kajima, and I. Kataoka, Optics Letters 20 (1995) 530.

[79] E. Morrison, B. J. Meers, D. I. Robertson, and H. Ward, Applied Optics 33 (1994) 5037.

[80] N. Mavalvala, *Alignment issues in laser interferometric gravitational wave detectors*, Ph. D thesis, Massachusetts Institute of Technology (1997).

[81] G. Heinzel, A. Rüdiger, R. Schilling, K. Strain, W. Winkler, J. Mizuno, and K. Danzmann, Optics Communications 160 (1999) 321.

Acknowledgements

It would have been impossible, beyond all question, to complete this doctoral work without the supports of many people.

First of all, I am deeply indebted to my supervisor, Professor Kimio Tsubono, who introduced me to this energetic field of gravitational wave detection. In addition, Prof. Tsubono encouraged me to start the power recycling experiments on the 3-m prototype interferometer. I am also indebted to Dr. Keita Kawabe for his scientific insights and technical supports. I have learned a lot of things from him on the fundamentals and art of the physical experiments. I am grateful to the members of Tsubono laboratory for their support. In particular, Mr. Koji Arai, with patient support and discussions, was instrumental in the completion of this work.

I would like to thank the members of the TAMA project for their useful discussions. In addition, some of the instruments used in this work were provided by the TAMA project and its members. I am especially grateful to Professor Norikatu Mio, Dr. Shigenori Moriwaki, and Dr. Masatake Ohashi for support of experimental instruments and for their useful and suggestive comment on the signal-separation scheme.

This research is supported by Research Fellowships of the Japan Society for the Promotion of Science for Young Scientists, and by a Grant-in-Aid for Creative Basic Research of the Ministry of Education.

Finally, I am grateful to my parents for everything.